

10

The Magnetic Inverse Problem

Eduardo Andrade Lima, Andrei Irimia and John P. Wikswo

- 10.1 The Peculiarities of the Magnetic Inverse Problem 141
- 10.2 The Magnetic Forward Problem 145
 - 10.2.1 Introduction 145
 - 10.2.2 Magnetic Fields from Magnetization Distributions 146
 - 10.2.2.1 Field and Moment of a Magnetic Dipole 146
 - 10.2.2.2 Magnetic Fields from Ferromagnetic Materials 147
 - 10.2.2.3 Magnetic Fields from Paramagnetic and Diamagnetic Materials 148
 - 10.2.3 Magnetic Fields from Current Distributions 149
 - 10.2.4 Magnetic Fields from Multipole Sources 152
 - 10.2.4.1 Introduction 152
 - 10.2.4.2 Poisson's and Laplace's Equations 152
 - 10.2.4.3 Magnetic Multipoles 159
 - 10.2.4.4 Current Multipoles in Conducting Media 165
- 10.3 The Magnetic Inverse Problem 168
 - 10.3.1 Introduction 168
 - 10.3.2 Inverting the Law of Biot and Savart 168
 - 10.3.2.1 Nonuniqueness of Inverse Solutions 168
 - 10.3.2.2 The Spatial Filtering Approach 169
 - 10.3.2.3 Dipole Fitting 208
 - 10.3.2.4 Methods for Regularization 209
 - 10.3.2.5 Lead Field Analysis 210
 - 10.3.2.6 The Finite-Element Method 216
 - 10.3.2.7 Phase-Sensitive Eddy-Current Analysis 226
 - 10.3.2.8 Summary of Inverse Magnetic Imaging of Current Distributions 227
 - 10.3.3 Imaging Magnetization Distributions 227
 - 10.3.3.1 The Dipole Field Equation 227
 - 10.3.3.2 Inverting the Dipole Field Equation for Diamagnetic and Paramagnetic Materials 230
 - 10.3.3.3 Two-Dimensional Magnetization Imaging 231
 - 10.3.3.4 Magnetic Susceptibility Tomography 232
 - 10.3.4 The Inverse Problem and Silent Sources 237

- 10.3.4.1 Introduction 237
- 10.3.4.2 The Helmholtz Decomposition 237
- 10.3.4.3 Electrically Silent Sources 239
- 10.3.4.4 Multipole Expansions 241
- 10.3.4.5 Multiple Dipole Models 243
- 10.3.5 Three-Dimensional Inverse Algorithms 245
 - 10.3.5.1 Introduction 245
 - 10.3.5.2 Beamformers 245
 - 10.3.5.3 Minimum Norm Techniques 246
 - 10.3.5.4 FOCUSS 248
 - 10.3.5.5 MUSIC 249
 - 10.3.5.6 Principal and Independent Component Analysis 251
 - 10.3.5.7 Signal Space Projection 252
 - 10.3.5.8 Other Three-Dimensional Methods 253
- 10.4 Conclusions 254

10.1

The Peculiarities of the Magnetic Inverse Problem

In the early days of SQUID magnetometry, a researcher was fortunate to have a single SQUID magnetometer to measure the magnetic field at a small number of locations outside of an object such as the human head or chest, a rock, a thin metal film, or a block of superconductor. The nature of the source being studied and the type of information being obtained would dictate the number of locations where the field had to be measured and how the data were to be analyzed. The fact that the magnetic field was measured from outside the object rather than from within meant that the description of the object was in fact inferred from the magnetic field by using the measurements to specify a limited number of parameters of a model that might describe the object. This process is known as the “magnetic inverse problem” and involves obtaining a description of the magnetic sources from measurements of their magnetic field.

An extremely simple example of the magnetic inverse problem would be to determine the average remanent magnetization of a large spherical object from an external magnetic field measurement. If the sphere were known to be homogeneously magnetized, the magnetic field outside of the sphere would be identical to that of a point magnetic dipole located at the center of the sphere. The magnetic field \vec{B} at the point \vec{r} produced by a point magnetic dipole \vec{m} at the point \vec{r}' is given by

$$\vec{B}(\vec{r}) = \frac{\mu_0}{4\pi} \left\{ \frac{3\vec{m} \cdot (\vec{r} - \vec{r}')}{|\vec{r} - \vec{r}'|^5} (\vec{r} - \vec{r}') - \frac{\vec{m}}{|\vec{r} - \vec{r}'|^3} \right\}. \quad (10.1)$$

Since this equation is linear in the dipole moment \vec{m} , if the location of the dipole is known, this equation can be inverted to obtain the three components of \vec{m} from measurement of the three components of \vec{B} at a single point \vec{r} ¹⁾

- 1) Taking the dot product of (10.1) with

$$\begin{aligned} &(\vec{r} - \vec{r}') \text{ and rearranging terms, we get} \\ \vec{m} \cdot (\vec{r} - \vec{r}') &= \frac{2\pi}{\mu_0} |\vec{r} - \vec{r}'|^3 \vec{B}(\vec{r}) \cdot (\vec{r} - \vec{r}'). \end{aligned}$$

By substituting this expression into (10.1) we obtain (10.2) after some manipulation (Mark Leifer, personal communication).

$$\vec{m} = \frac{4\pi}{\mu_0} |\vec{r} - \vec{r}'|^3 \left\{ \frac{3}{2} \frac{\vec{B}(\vec{r}') \cdot (\vec{r} - \vec{r}')}{|\vec{r} - \vec{r}'|^2} (\vec{r} - \vec{r}') - \vec{B}(\vec{r}') \right\}. \quad (10.2)$$

Hence it is sufficient to measure the magnetic field \vec{B} at a single known location \vec{r} outside of the sphere. However, if our sphere has only a small number of small regions that are magnetized but at unknown locations within the sphere, we would need multiple dipoles to describe the field. Since the location of these dipoles is unknown, the nonlinearity of (10.1) in \vec{r} and \vec{r}' makes the inverse process much harder; in general, there is no closed-form analytical solution for determining both \vec{m} and \vec{r}' from measurements of \vec{B} at multiple locations. In this context, there is another serious implication of (10.1): the fall-off of the field with distance serves as a harsh low-pass spatial filter, so that the further a magnetic object is from the measurement location, the greater is the spatial blurring of the contribution of adjacent source regions. The loss of information with distance is so rapid that it often cannot be balanced by realistic reductions of sensor noise.

More importantly, were the object we were studying to contain a spherical shell of uniform radial magnetization, the integration of (10.1) over that shell would produce a zero magnetic field outside of the shell. Hence no magnetic measurements and inverse process would be able to detect the presence of such a closed shell were it somewhere inside the object. Similar problems occur in the interpretation of magnetic fields from current sources in conducting objects, whether they are a heart, a brain, or a corroding aircraft wing: whenever a measured field obeys Laplace's equation, there exists the possibility of source distributions with symmetries such that they produce no externally detectable fields. The ability to add or subtract such silent sources at will without altering the measured field corresponds to the lack of a unique solution to an inverse problem.

The nonuniqueness of the solution to the inverse problem was first realized by Helmholtz [1] in 1853, but was described in the context of electrostatics. Helmholtz stated [2], in now-archaic terminology, that "... the same electromotoric surface may correspond to infinitely many distributions of electromotoric forces inside the conductors, which have only in common that they produce the same tensions (voltages) between given points on the surface." As we will see in the following sections, both electric and magnetic fields satisfy Laplace's and Poisson's equations in the static limit and, consequently, have many properties in common, such as nonuniqueness. We will weave aspects of silent source distributions throughout this chapter.

Added problems, or at least confusion, can arise from the vector nature of the magnetic field, in that often an array of SQUIDS may not measure all three components of the magnetic field vector. To explore this, let us consider an infinite volume divided into upper and lower semi-infinite half spaces. Current and magnetization distributions occupy the lower half space, while the upper half space is vacuum. We further restrict our problem by placing our SQUIDS only on a hori-

zontal plane in the upper half space, as shown in Figure 10.1. In theory, a measurement of a *single component* of the vector magnetic field everywhere over this infinite horizontal plane will contain all of the information about the magnetic field everywhere in the upper half space, consistent with the magnetic field obeying Laplace's equation. Upward or downward continuation of the measured magnetic field above or below the measurement plane will allow one to specify the magnetic field everywhere in the upper half space. In practice, however, one can measure the magnetic field at only a finite number of locations in the plane. In this case, there are not only issues regarding the Shannon sampling theorem and the maximum allowable separation between field measurements for a given source distribution, but also questions as to how best to distribute a collection of one-, two-, and three-axis SQUIDs over the measurement plane. For example, the accuracy of solutions to the inverse problem for the head or abdomen using a moderate number of SQUID channels may well be improved by allocation of some SQUIDs to vector magnetometers at the edge of a finite array and single-component SQUIDs elsewhere [3, 4].

These and other limitations of the magnetic inverse problem arise from the presence of scalar and vector products inherent in Maxwell's equations, and produce inverse challenges that are not encountered in optical, X-ray, ultrasound, NMR, or tactile images. Generally, the interpretation of optical images in terms of the sources that produce the image, *i.e.*, the optical inverse problem, may require

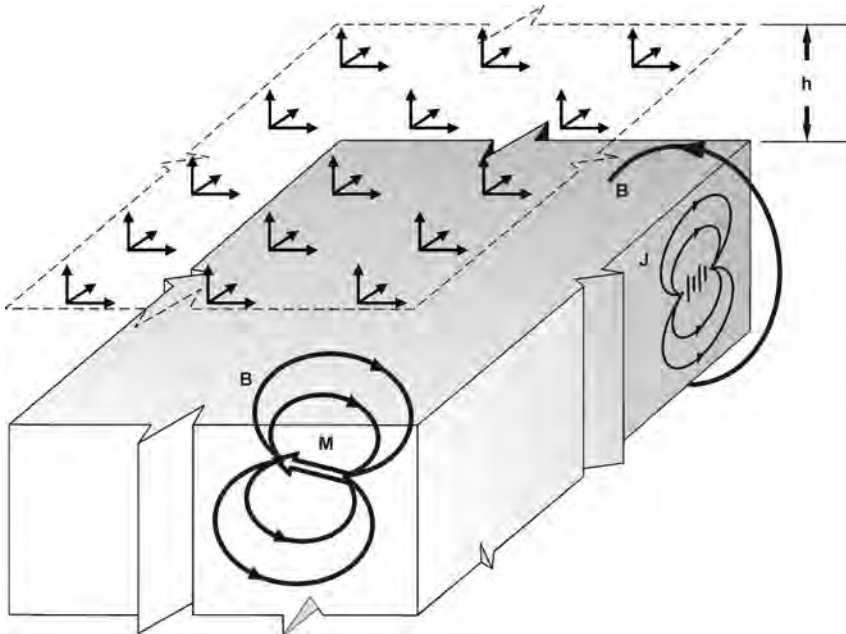


Fig. 10.1 A semi-infinite half space containing current and magnetization distributions, whose associated magnetic field is measured by a planar array of vector SQUID magnetometers in the upper, source-free half space.

deconvolution but will not require the inversion of a Laplacian field, but the magnetic inverse problem does. This should give an indication of the difficulties that will be encountered in attempting to use magnetic field measurements to discern the magnetic or electric sources hidden from direct view within an object.

In the days of a single SQUID and simple models, or instruments dedicated to measuring a single physical property, the appropriate equation for a simple model could be selected with care and intuition to obtain the required information. However, complex models, as would be required to describe spatially distributed heterogeneous sources in the brain or a thin slice of a meteorite, require measurement of the magnetic field at the least at as many points as there are model parameters. If the source distribution is either time-independent or periodic, a single magnetometer can be used to make sequential measurements at multiple locations. Today, the number of points where a scanned SQUID measures the magnetic field may exceed 125 000 [5, 6]. If the time-varying source distribution is aperiodic with a time variation that exceeds the rate at which the SQUID can be moved, one has no choice but to use multiple SQUIDS to record simultaneously the field at the required number of locations. For this reason, the number of SQUID sensors in a magnetoencephalogram (MEG) system is now approaching 1000. In these two cases it is reasonable to consider this as a problem in magnetic imaging: a magnetometer produces a vector or scalar “image” of the magnetic field, and the magnetic inverse problem becomes one of determining an “image” of the associated source distribution. In many situations, a source image can be obtained only after performing some sort of vector processing, as both the sources and their fields usually have a vector nature and are not colinear. In the limit of magnetic imaging of distributed, vector sources, our intuition based upon single point dipoles may fail us and there may not be a simple vector manipulation that can provide us with the answer.

What began 35 years ago as a SQUID measurement of the magnetic field at a single point above the human chest [7] has now progressed to the point of true magnetic images created by scanning a high-resolution SQUID microscope over a highly heterogeneous section of a Martian meteorite [8]. Hence the magnetic inverse problem has now evolved to include problems in image deconvolution that are potentially complicated by the nonuniqueness of the magnetic inverse problem. In this chapter, we establish a firm mathematical foundation for the magnetic inverse problem and present a number of simple examples, drawn primarily from our research in the field, borrowing extensively from and building upon an earlier book chapter [9]. We concentrate on the general issues of the magnetic inverse problem, and leave the discussion of MEG and magnetocardiogram (MCG) applications of three-dimensional inverse algorithms to Chapter 11. The present chapter is intended to serve as a tutorial, and not an all-inclusive review of the literature.

10.2 The Magnetic Forward Problem

10.2.1

Introduction

In order to explain the magnetic inverse problem, it is important first to define the forward one: the calculation of the magnetic field given a complete description of the sources. As shown in Figure 10.2, there are a number of different mechanisms by which magnetic fields can be generated. From the perspective of the forward problem, these can be grouped by which of two formulas govern the field production. The first, the law of Biot and Savart, is used to describe the magnetic

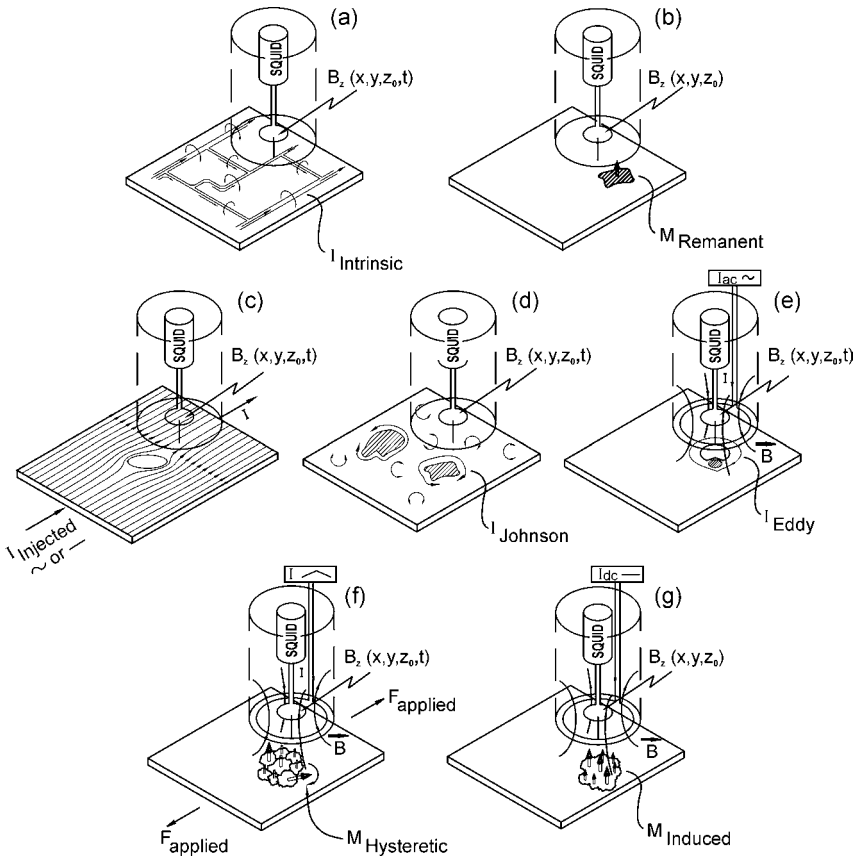


Fig. 10.2 Various mechanisms by which a scanning SQUID magnetometer can produce an image: (a) intrinsic currents, (b) remanent magnetization, (c) flaw-induced perturbations in applied currents, (d) Johnson noise in conductors, (e) eddy currents and their

perturbations by flaws, (f) hysteretic magnetization in ferromagnetic materials in the presence of an applied stress, and (g) diamagnetic and paramagnetic materials in an applied field. (Adapted from Ref. [141], with permission.)

fields produced by intrinsic currents, for example the magnetocardiogram (MCG) and MEG produced by current sources in the heart and brain, or from currents applied to a printed or integrated circuit, as is shown in Figure 10.2(a). Johnson noise arising from thermal motion of electrons in a conductor (Figure 10.2(d)) can produce measurable magnetic fields, as can inhomogeneity-induced perturbations in applied currents (Figure 10.2(c)). The second, the equation for the magnetic field of a point magnetic dipole, governs the field from remanent magnetization from ferromagnetic objects or inclusions (Figure 10.2(b)), ferromagnetic materials under stress, with or without an applied field (Figure 10.2(f)), or from paramagnetic or diamagnetic objects in an applied, static magnetic field (Figure 10.2(g)). If one applies an oscillating field, SQUIDS can be used to image the eddy currents (Figure 10.2(e)). After we examine the two governing equations in some detail, *i.e.*, the magnetic forward problem, we will then examine their inversion, *i.e.*, the magnetic inverse problem.

In this chapter, we will limit our discussion to the quasistatic magnetic field, *i.e.*, the field determined by the instantaneous sources. We do not consider the rate of change of the magnetic field, retarded potentials, *etc.* The time variation must be slow enough that inductive effects can be ignored, appropriate for most low-frequency SQUID applications except those involving eddy currents in metals.

In this chapter, we also do not address the numerous computational techniques that have been developed for the forward problem of calculating the magnetic field from current and magnetization distributions, but instead will outline the general principles that govern the forward problem for a variety of source and sample geometries.

10.2.2

Magnetic Fields from Magnetization Distributions

10.2.2.1 Field and Moment of a Magnetic Dipole

In the quasistatic limit, the magnetic field of a magnetostatic dipole is given by (10.1). For an object with a distributed magnetization $\vec{M}(\vec{r}')$, which is equivalent to a dipole density, each differential volume element d^3r' in the object is assigned a dipole moment $\vec{m}(\vec{r}')$ that is equal to $\vec{M}(\vec{r}')d^3r'$, so that we can simply integrate (10.1)

$$\vec{B}(\vec{r}) = \frac{\mu_0}{4\pi} \int_V \left\{ \frac{3\vec{M}(\vec{r}') \cdot (\vec{r} - \vec{r}')}{|\vec{r} - \vec{r}'|^5} (\vec{r} - \vec{r}') - \frac{\vec{M}(\vec{r}')}{|\vec{r} - \vec{r}'|^3} \right\} d^3r'. \quad (10.3)$$

The magnetization can either be permanent, *e.g.*, ferromagnetic remanent magnetization, or induced through diamagnetic, paramagnetic, or ferromagnetic effects. Let us suppose that an object made of magnetically linear, isotropic material is

placed in a magnetic field produced by a distant electromagnet. The magnetization $\vec{M}(\vec{r})$ at a source point \vec{r} is determined by the product of the magnetic susceptibility $\chi(\vec{r})$ and the applied magnetic field intensity $\vec{H}(\vec{r})$

$$\vec{M}(\vec{r}) = \chi(\vec{r})\vec{H}(\vec{r}). \quad (10.4)$$

The magnetic induction field \vec{B} , hereafter referred to as the “magnetic field,” at the same source point \vec{r} is given by

$$\vec{B}(\vec{r}) = \mu_0 \left\{ \vec{H}(\vec{r}) + \vec{M}(\vec{r}) \right\}, \quad (10.5)$$

where μ_0 is the permeability of free space. We can express this in terms of the susceptibility χ by substituting (10.4) into (10.5) to obtain

$$\vec{B}(\vec{r}) = \mu_0 \left\{ 1 + \chi(\vec{r}) \right\} \vec{H}(\vec{r}) \quad (10.6)$$

$$= \mu_0 \mu_r(\vec{r}) \vec{H}(\vec{r}) \quad (10.7)$$

$$= \mu(\vec{r}) \vec{H}(\vec{r}), \quad (10.8)$$

where the relative permeability μ_r is given by

$$\mu_r(\vec{r}) = 1 + \chi(\vec{r}) \quad (10.9)$$

and the absolute permeability μ is

$$\mu(\vec{r}) = \mu_0 \mu_r(\vec{r}). \quad (10.10)$$

As we shall see, the difficulty with susceptibility and magnetization imaging is that the field measured by the SQUID is not the local field within the object, but the field in the source-free region outside of the object.

10.2.2.2 Magnetic Fields from Ferromagnetic Materials

Soft ferromagnetic materials have high permeabilities, in the approximate range $10^3 \leq \mu_r \leq 10^5$, so that

$$\mu_r = 1 + \chi \approx \chi. \quad (10.11)$$

In general for these materials, χ , and hence μ_r , are functions of the applied field. If the materials are “hard,” they exhibit significant hysteresis; if they are “soft,”

they do not. Soft materials may exhibit a range of fields for which χ is approximately constant, but in general for ferromagnetic materials, χ has a strong dependence on the applied field. In either case, there is an applied \vec{H} above which the material saturates and the magnetization \vec{M} in (10.4) attains a maximum value. Above that value, any increases in \vec{B} in (10.5) are due only to the increase in \vec{H} . Since the magnetic field within soft ferromagnetic materials can be from 10^3 to 10^5 times the applied field, the determination of the magnetization within a ferromagnetic material must be made in the strong-field limit: $\vec{B} = \mu_0(\vec{H} + \vec{M}) = \mu\vec{H}$ at any point in the material, so that \vec{M} at one point is affected by \vec{M} at other points in the material. Self-consistency requires simultaneous solution of \vec{H} and \vec{M} everywhere, since $\vec{M}(\vec{r})$ is determined by both $\vec{H}(\vec{r})$ and $\chi(\vec{r})$, even if the applied field \vec{H} was initially uniform before the object was placed in the field. In this strong-field case, the magnetic inverse problem, *i.e.*, the inversion of (10.3) to determine $\vec{M}(\vec{r})$, is difficult to impossible, particularly if there is a remanent (hard) magnetization superimposed upon the induced (soft) magnetization. While it is difficult to induce a soft, spherically symmetric, magnetically silent magnet with external fields, it is in principle possible to have such a distribution in a hard component of magnetization, and this leads to the previously discussed nonuniqueness problem.

10.2.2.3 Magnetic Fields from Paramagnetic and Diamagnetic Materials

The situation is much friendlier for the magnetic imaging of paramagnetic ($0 \leq \chi \leq 10^{-3}$) and diamagnetic ($-10^{-6} \leq \chi \leq 0$) materials, in that

$$\mu_r = 1 + \chi \approx 1. \quad (10.12)$$

As a result, the variation in the magnitude of the induced magnetic field \vec{B} is 10^{-6} to 10^{-3} times the magnetic field in free space, and is proportional to the applied field, since paramagnetic and diamagnetic materials are linear and nonhysteretic at practical applied fields. The most significant feature of the low susceptibility of these materials is that (10.3) can be evaluated in the weak-field limit, also known as the Born approximation: at any point in the material we can ignore the contributions to the applied field at \vec{r} from the magnetization elsewhere in the object and consider the applied magnetic intensity \vec{H} as it would be in the absence of the magnetic material. In that case, we immediately know the magnetic field \vec{B} everywhere as well. In the Born approximation, the magnetization is independent of the magnetization elsewhere in the sample, and hence is a local phenomenon, in contrast to ferromagnetism. Because \vec{M} is so weak for diamagnetic and paramagnetic materials, if we know \vec{H} everywhere, we shall then know \vec{B} to at least one part in 10^3 for a paramagnetic material with $\chi = 10^{-3}$, and to one part in 10^6 for a diamagnetic one with $\chi = -10^{-6}$. Thus, we have eliminated a major problem in obtaining a self-consistent, macroscopic solution that is based upon the microscopic constitutive equation given by (10.5). Because of their periodic flux-voltage characteristic, and the ability to thermally release magnetic flux trapped in pickup

coils, SQUID magnetometers readily can measure only the very small perturbation $\vec{B}_p(\vec{r})$ in the applied magnetic field [10]. We thereby can eliminate \vec{B} and \vec{H} from the imaging problem, and need them only to determine the magnetization. The measured magnetic field, $\vec{B}_p(\vec{r})$, thus is given by (10.3) where

$$\vec{M}(\vec{r}) = \frac{\chi(\vec{r})}{\mu_0} \vec{B}(\vec{r}) = \chi(\vec{r}) \vec{H}(\vec{r}). \quad (10.13)$$

If $\vec{H}(\vec{r})$ is uniform, then the spatial variation of $\vec{M}(\vec{r})$ is determined only by $\chi(\vec{r})$. For isotropic materials, χ is a scalar, and the direction of \vec{M} is the same as that of \vec{B} ; otherwise, a tensor susceptibility is required.

10.2.3

Magnetic Fields from Current Distributions

The calculation of the magnetic fields from magnetizations is conceptually straightforward because the only vector operation is the dot product in the first term of (10.3). In contrast, the law of Biot and Savart contains a vector cross product which complicates the problem. Let us start with the simplest case of determining the distribution of currents in a planar circuit, as shown, for example, in Figures 10.2(a), 10.3, and 10.4. In general, the magnetic field $\vec{B}(\vec{r})$ at the point \vec{r} is given by the law of Biot and Savart

$$\vec{B}(\vec{r}) = \frac{\mu_0}{4\pi} \int_V \frac{\vec{J}(\vec{r}') \times (\vec{r} - \vec{r}')}{|\vec{r} - \vec{r}'|^3} d^3r', \quad (10.14)$$

where $\vec{J}(\vec{r}')$ is the current density at point \vec{r}' . It is also instructive to rewrite (10.14) in terms of the curl of the current distribution [11, 12]

$$\vec{B}(\vec{r}) = \frac{\mu_0}{4\pi} \int_S \frac{\vec{J}(\vec{r}') \times \hat{n}}{|\vec{r} - \vec{r}'|} d^2r' + \frac{\mu_0}{4\pi} \int_V \frac{\nabla' \times \vec{J}(\vec{r}')}{|\vec{r} - \vec{r}'|} d^3r', \quad (10.15)$$

where \hat{n} is the normal to the surface S that bounds the object or regions within the object with differing conductivities. The first integral represents the magnetic field due to the discontinuity of the tangential component of the current at any external or internal boundaries of the object, and the second is that produced by any curl within the object. Note that within a homogeneous conductor, any current distribution that has zero curl will not contribute to the external magnetic field and, hence, will be magnetically silent [13–15]. This implies that in homogeneous, three-dimensional conductors, currents that obey Ohm's law, relating the current density to either the electric field \vec{E} or the electric scalar potential V , *e.g.*,

$$\vec{J}(\vec{r}) = \sigma \vec{E}(\vec{r}) = -\sigma \nabla V(\vec{r}), \quad (10.16)$$

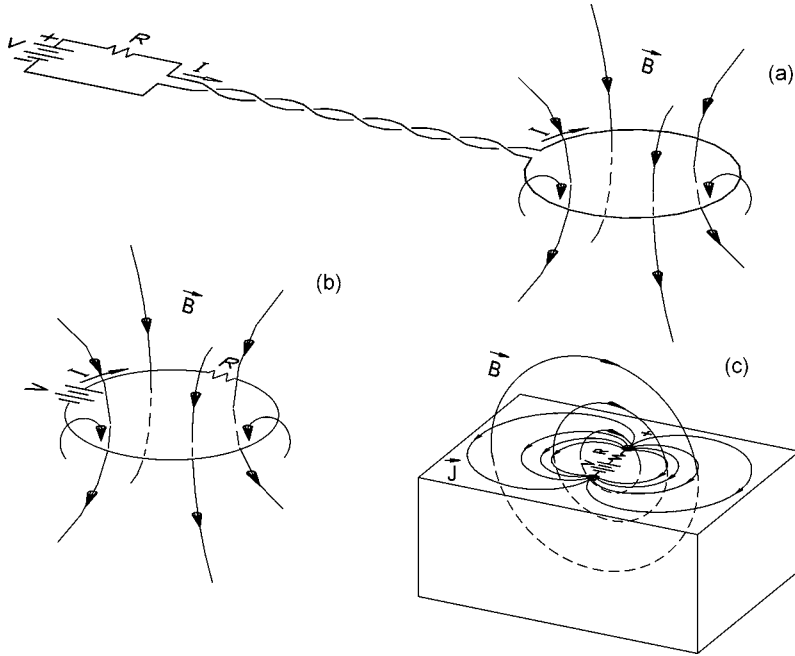


Fig. 10.3 Currents and their magnetic fields: (a) a loop of wire and its magnetic field \vec{B} , when the battery is far away. It follows from Ampère's law that the magnetic field from the leads connecting the battery to the loop is negligible because the leads are tightly twisted; (b) a loop of wire that contains a voltage source and a current-limiting resistor; (c) the current and magnetic field distribu-

tions from a current source located on the surface of a conducting bath of saline. The source can be thought of as a current dipole whose moment (*i.e.*, strength) is the product of the spacing between the positive and negative electrodes times the current passing between them. (Adapted from Ref. [243], with permission.)

do not contribute to the magnetic field because the curl of a gradient is identically zero, and the conductivity σ is a constant within the volume V and passes through the curl operator. Batteries, such as a dry cell dropped into a conducting medium (Figure 10.4), or the microscopic equivalent, a current dipole [16, 17], are non-Ohmic and hence can have curl. The first term in (10.15) would indicate that whenever Ohmic currents encounter a boundary or a discontinuity in conductivity, a magnetic field could be produced, since a discontinuity in the component of the current density tangential to a boundary is equivalent to a curl.²⁾ In a thin sheet that would approximate a two-dimensional conductor, the sample has two parallel surfaces in proximity that have curls of opposite sign which cancel each

2) The insulating boundary on the side of the cylindrical battery in Figure 10.4 produces a discontinuity of tangential current, and this provides an alternative description for the magnetic field produced by a battery in a

homogeneous conducting medium. Whether or not this approach is taken, it is extremely important to recognize the importance of insulating layers such as those outside of batteries and wires.

other far from the sheet; the curl that contributes most strongly to the magnetic field is that from any edges in the conductor. A current-carrying wire, bent into a pattern, has a curl all along its surface. We shall address the role of spatial variations in the conductivity σ in two-dimensional conductors in a later section. For now, we shall concentrate on sheet conductors with a constant (homogeneous) conductivity σ .

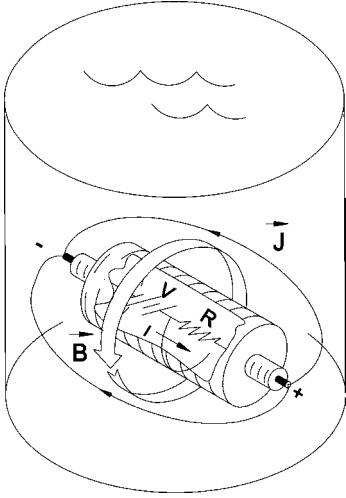


Fig. 10.4 A simple current source in the form of a battery in a bucket of saline. Currents flow in the saline, and a magnetic field encircles the battery. (Adapted from Ref. [243], with permission.)

In typical measurements, the component of the magnetic field normal to the sample, B_z , is mapped by scanning the SQUID pickup coil of radius a over the sample, at a fixed height z_0 , as shown in Figure 10.5. In this case, we can expand the cross product in (10.14) and rewrite the law of Biot and Savart as a pair of integrals

$$B_z(\vec{r}) = \frac{\mu_0}{4\pi} \int_V \frac{J_x(\vec{r}') (y - y')}{|\vec{r} - \vec{r}'|^3} d^3 r' - \frac{\mu_0}{4\pi} \int_V \frac{J_y(\vec{r}') (x - x')}{|\vec{r} - \vec{r}'|^3} d^3 r'. \quad (10.17)$$

Equations (10.14) and (10.17) are convolution integrals. The source of the field is the current density $\vec{J}(\vec{r}')$; the remaining terms of the integrand are a function of both \vec{r} and \vec{r}' and form the Green's function $G(\vec{r} - \vec{r}')$. To calculate the magnetic field, we integrate the product of \vec{J} and G over the entire region where \vec{J} is non-zero, *i.e.*, we convolve \vec{J} and G to determine \vec{B} . Note that in (10.14), G is a vector function that contains the cross product, but in (10.17), it is a pair of scalar functions. It is worth noting that identical arguments starting with (10.3) show that the magnetic field from a magnetization distribution can be expressed as the convolution of $\vec{M}(\vec{r}')$ with another vector Green's function.

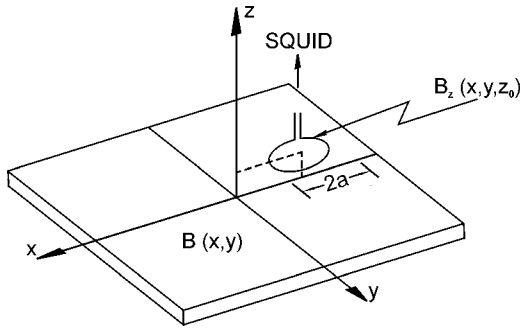


Fig. 10.5 The geometric arrangement and coordinates for a SQUID that is scanned over a current-carrying sample. (Adapted from Ref. [56], with permission.)

10.2.4

Magnetic Fields from Multipole Sources

10.2.4.1 Introduction

Any discussion of the forward problem would not be complete without a description of the relationship between multipole sources and their fields. In the following sections, we discuss the commonalities of the magnetic fields associated with a number of different sources, how the magnetic field can be described in terms of the gradient of a scalar magnetic potential, and how this in turn provides the basis for multipole expansions of either the sources or their fields. While this last topic is intimately connected with the inverse problem, we present it first under the forward problem because physical representations of magnetic dipoles and quadrupoles (in contrast to their abstract mathematical equivalents) are often the actual sources of magnetic fields, and hence a description of the spatial dependence of these fields is critical to understanding their measurement and mapping.

10.2.4.2 Poisson's and Laplace's Equations

In contrast to ray-based imaging modalities that involve the focusing of electromagnetic or acoustic waves onto detector arrays, and are hence governed by the equations of propagating waves, a magnetic field is governed by the laws of Biot and Savart, Ampère, and Gauss (which are the static limits of the dynamic Maxwell equations that govern electromagnetic wave propagation). We have already presented the equations that describe the relation between an electric or magnetic source distribution and the associated magnetic field ((10.1), (10.3), (10.14), (10.15), (10.17)). Now we need to show how the magnetic field in the source-free region occupied by the SQUID obeys the much simpler Laplace's equation. As we will see later in this chapter, this simplification carries with it a cost in a reduction

of the information contained in the field and a corresponding restriction on the invertibility of the field equations and the solution to the inverse problem. This section draws extensively from Ref. [18].

To aid in our development of an intuition regarding Laplace's equation, it is worthwhile to begin with electrostatic fields. Let us first consider a quasistatic charge distribution given by the charge density $\rho(\vec{r})$. In vacuum, Gauss' law for the electric field \vec{E} reduces to

$$\nabla \cdot \vec{E}(\vec{r}) = \rho(\vec{r})/\epsilon_0, \quad (10.18)$$

where ϵ_0 is the electrical permittivity of free space. Because the differential form of Faraday's law reduces to $\nabla \times \vec{E}(\vec{r}) = \vec{0}$ for a quasistatic charge distribution, the electric field can be described as the negative gradient of the scalar electrostatic potential $V(\vec{r})$, where

$$\vec{E}(\vec{r}) = -\nabla V(\vec{r}). \quad (10.19)$$

Equations (10.18) and (10.19) can be combined to obtain Poisson's equation

$$\nabla^2 V(\vec{r}) = -\rho(\vec{r})/\epsilon_0, \quad (10.20)$$

which is known to have the solution

$$V(\vec{r}) = \frac{1}{4\pi\epsilon_0} \int_V \frac{\rho(\vec{r}')}{|\vec{r} - \vec{r}'|} d^3r'. \quad (10.21)$$

This equation shows that, in the mathematical sense, the charge density $\rho(\vec{r})$ is the "source" of the scalar potential.³⁾ Most importantly, if we restrict our attention to source-free regions where $\rho(\vec{r}) = 0$, we find that the electrostatic potential obeys Laplace's equation

$$\nabla^2 V(\vec{r}) = 0, \quad (10.22)$$

and the entire armamentarium of techniques to solve Laplace's equation can be brought to bear on the problem.

We can now extend our analysis to consider the electric field of current sources in a homogeneous conductor. In an infinite, homogeneous, isotropic, linear conductor, containing sources of electromotive force (EMF), the quasistatic current density $\vec{J}(\vec{r})$ obeys Ohm's law, which can be written as

$$\vec{J}(\vec{r}) = \sigma \vec{E}(\vec{r}) + \sigma \vec{E}^i(\vec{r}) = \sigma \vec{E}(\vec{r}) + \vec{J}^i(\vec{r}), \quad (10.23)$$

3) A purist would argue that one cannot have the electrostatic potential without the charge, and vice versa, so that it is better to describe the charge and the potential as

being "associated" with each other, rather than having the charge as the "source" of a field.

where the impressed voltage $\vec{E}^i(\vec{r})$ is zero, where there are no EMFs, and σ is the electrical conductivity of the conductor. Alternatively, the effect of the EMFs can be described in terms of the impressed current density \vec{j}^i . It can be shown that \vec{E}^i can be described as an EMF dipole density and \vec{j}^i can be interpreted as a current dipole density [19]. Because of the high impedance of the cellular membranes across which bioelectric currents are driven by transmembrane concentration gradients, bioelectric sources are almost always described in terms of \vec{j}^i rather than \vec{E}^i . It is important to note that in the quasistatic limit conservation of charge requires that $\nabla \cdot \vec{j}(\vec{r}) = 0$. Taking the divergence of (10.23) and using (10.19), we once again obtain Poisson's equation

$$\nabla^2 V(\vec{r}) = \frac{1}{\sigma} \nabla \cdot \vec{j}^i(\vec{r}), \quad (10.24)$$

which has the solution

$$V(\vec{r}) = \frac{1}{4\pi\sigma} \int_V \frac{-\nabla' \cdot \vec{j}^i(\vec{r}')}{|\vec{r} - \vec{r}'|} d^3r', \quad (10.25)$$

and we see that $\nabla \cdot \vec{j}^i(\vec{r})$ is the source of the scalar potential. In regions within the conductor where $\nabla \cdot \vec{j}^i = 0$, this reduces to Laplace's equation.

The extension of this formalism to the magnetic field of steady-state current distributions is straightforward. We have already shown that the law of Biot and Savart can be written as

$$\vec{B}(\vec{r}) = \frac{\mu_0}{4\pi} \int_V \frac{\nabla' \times \vec{j}(\vec{r}')}{|\vec{r} - \vec{r}'|} d^3r'. \quad (10.26)$$

We now recognize this as the solution to a vector form of Poisson's equation,

$$\nabla^2 \vec{B}(\vec{r}) = -\mu_0 \nabla \times \vec{j}(\vec{r}), \quad (10.27)$$

wherein each Cartesian component of \vec{B} is Laplacian, with a source that is the corresponding Cartesian component of $\nabla \times \vec{j}$. In the event that the current density is produced by impressed current sources in an unbounded homogeneous medium that obeys Ohm's law, (10.23) reduces to

$$\vec{j}(\vec{r}) = -\sigma \nabla V(\vec{r}) + \vec{j}^i(\vec{r}), \quad (10.28)$$

such that

$$\nabla \times \vec{j}(\vec{r}) = \nabla \times \vec{j}^i(\vec{r}), \quad (10.29)$$

so that the solution for infinite homogeneous conductors reduces to Poisson's equation for which the integration can be restricted to the region containing impressed currents

$$\vec{B}(\vec{r}) = \frac{\mu_0}{4\pi} \int_V \frac{\nabla' \times \vec{j}^i(\vec{r}')}{|\vec{r} - \vec{r}'|} d^3r'. \quad (10.30)$$

This equation is particularly significant in that it shows that for unbounded conductors, the Ohmic currents do not contribute to the magnetic field, and the field is determined by the impressed currents alone.

This result also leads to an important equation for the case where the source is a current dipole \vec{P} located at \vec{r}'' , *i.e.*,

$$\vec{j}^i(\vec{r}') = \vec{P} \delta(\vec{r}' - \vec{r}''), \quad (10.31)$$

where $\delta(\vec{r}' - \vec{r}'')$ is the Dirac delta function. We can apply (10.31) to (10.23) to write (10.14) as

$$\vec{B}(\vec{r}) = \frac{\mu_0}{4\pi} \frac{\vec{P} \times (\vec{r} - \vec{r}'')}{|\vec{r} - \vec{r}''|^3}. \quad (10.32)$$

It is vital to note that deeply embedded in the derivation of this equation is the assumption that we are dealing with an unbounded homogeneous conductor. The fascinating aspect of this equation is that it is, in effect, a differential form of the law of Biot and Savart, operating on only one portion of the complete "circuit." While in general this would raise concerns over current continuity and Newton's third law, in this special case of an unbounded conductor, \vec{P} is a point source of current, and the magnetic field contributions of each differential element of the return Ohmic current integrate exactly to zero. Figure 10.4 shows how a current dipole or a small battery has an encircling magnetic field, which in an unbounded conductor would be given by (10.32). In the limit of a very large bucket and a battery that reduces to a current dipole, the magnetic field can be calculated by considering only the current dipole moment of the battery. For small buckets, the discontinuity in the tangential current at the wall of the bucket will also contribute to the magnetic field. As will be apparent in the subsequent discussion of edge effects, it is important to appreciate that magnetic fields can be exquisitely sensitive to discontinuities in the tangential current!

For completeness, it is important to point out that the addition of boundary surfaces S_j within the conductor, thereby making the conductor only *piecewise* homogeneous, will add secondary current sources \vec{K}^i that are given by the product of the difference in conductivities across the boundary with the potential at the

boundary, with an orientation specified by the normal \hat{n}_j to the boundary [20], such that

$$\vec{K}^i(\vec{r}) = -(\sigma' - \sigma'')V(\vec{r})\hat{n}_j(\vec{r}) \quad \text{for } \vec{r} \text{ on all } S_j, \quad (10.33)$$

$$\vec{K}^i(\vec{r}) = \vec{0} \quad \text{for } \vec{r} \text{ not on any } S_j$$

In this case, our equations for the electric potential and magnetic field become [21, 22]

$$V(\vec{r}) = \frac{1}{4\pi\sigma} \int_V \frac{-\nabla' \cdot \{\vec{J}^i(\vec{r}') + \vec{K}^i(\vec{r}')\}}{|\vec{r} - \vec{r}'|} d^3r', \quad (10.35)$$

$$\vec{B}(\vec{r}) = \frac{\mu_0}{4\pi} \int_V \frac{\nabla' \times \{\vec{J}^i(\vec{r}') + \vec{K}^i(\vec{r}')\}}{|\vec{r} - \vec{r}'|} d^3r'. \quad (10.36)$$

As we will see later, these two equations are critical in understanding the relation between bioelectric and biomagnetic fields.

If the current distribution is bounded, as it would be for a conductor bounded by a surface S , the curl of \vec{B} , as given by Maxwell's fourth equation, must be zero outside of S , *i.e.*,

$$\nabla \times \vec{B}(\vec{r}) = \vec{0}. \quad (10.37)$$

Any field that has no curl can be described in terms of the gradient of the magnetic scalar potential, so that we can now write

$$\vec{B}(\vec{r}) = -\mu_0 \nabla V_m(\vec{r}) \quad \text{outside } S. \quad (10.38)$$

Since $\nabla \cdot \vec{B}(\vec{r})$ is zero everywhere,

$$\nabla^2 V_m = 0 \quad \text{outside } S, \quad (10.39)$$

and we see that the quasistatic magnetic field in a current-free region can be derived from a scalar potential obeying Laplace's equation. The identical result applies to a bounded object with a quasistatic magnetization $\vec{M}(\vec{r})$: the magnetic induction *outside* the object must satisfy (10.39).

Inside a magnetized object, $\vec{B}(\vec{r})$ is given by

$$\vec{B}(\vec{r}) = -\mu_0 \nabla V_m(\vec{r}) + \mu_0 \vec{M}(\vec{r}). \quad (10.40)$$

If we take the divergence of each term and note that $\nabla \cdot \vec{B}(\vec{r}) = 0$, we obtain Poisson's equation for V_m

$$\nabla^2 V_m(\vec{r}) = \nabla \cdot \vec{M}(\vec{r}) . \quad (10.41)$$

This has the solution

$$V_m(\vec{r}) = \frac{1}{4\pi} \int_V \frac{-\nabla' \cdot \vec{M}(\vec{r}')}{|\vec{r} - \vec{r}'|} d^3 r' , \quad (10.42)$$

which shows that $-\nabla \cdot \vec{M}(\vec{r})$ can be interpreted as an effective magnetic charge density that is the source of V_m . Similar to the constraint on $\nabla \cdot \vec{J}$ for the electric field of a distributed current, the condition that $\nabla \cdot \vec{B} = 0$ implies that

$$\int_V \nabla' \cdot \vec{M}(\vec{r}') d^3 r' = 0 . \quad (10.43)$$

Equation (10.41) shows that the magnetic field outside of a magnetized object is also Laplacian, so we can describe the current-related source of V_m in (10.38) as an effective magnetization given by [18, 23]

$$\vec{M}(\vec{r}) = \frac{1}{2} \vec{r} \times \vec{J}(\vec{r}) . \quad (10.44)$$

The divergence of \vec{M} becomes

$$\nabla \cdot \vec{M}(\vec{r}) = \nabla \cdot \left[\frac{1}{2} \vec{r} \times \vec{J}(\vec{r}) \right] = -\frac{1}{2} \vec{r} \cdot [\nabla \times \vec{J}(\vec{r})] . \quad (10.45)$$

Thus the magnetic scalar potential outside the bounded current distribution satisfies the equation

$$V_m(\vec{r}) = \frac{1}{4\pi} \int_V \frac{\frac{1}{2} \vec{r}' \cdot \nabla' \times \vec{J}(\vec{r}')}{|\vec{r} - \vec{r}'|} d^3 r' , \quad (10.46)$$

and we identify the source of V_m to be one-half the radial component of the curl of \vec{J} . In unbounded homogeneous media with impressed current sources, \vec{J} can be replaced by \vec{j}^i . In the piecewise homogeneous case, it is necessary to include the secondary sources \vec{K}^i .

We close the loop on boundary effects by noting that the symmetry of a bounded conductor may lead to several interesting results. A radial current dipole in a spherical conductor and a current dipole perpendicular to the surface of a semi-infinite conductor produce *no* magnetic field *outside* the conductor. A current

dipole parallel to and below the surface of a conducting half space produces a magnetic field in the upper half space given by (10.32), as if the boundary did not exist [24].

The equations derived in this section, summarized in Table 10.1, can be used to calculate the electric and magnetic fields from various sources. The problem of greater complexity is the inverse one of fitting a model of the source to observed field data.

Table 10.1 Summary of the electric and magnetic Poisson's equations [18]

General form: $\nabla^2 \Psi(\vec{r}) = -s(\vec{r})$, $\Psi(\vec{r}) = \frac{1}{4\pi} \int_V \frac{s(\vec{r}')}{|\vec{r} - \vec{r}'|} d^3 r'$

Field	Sources, s	Solution to Poisson's equations
Electric scalar potential $V(\vec{r})$ from a quasistatic charge distribution $\rho(\vec{r})$	$s(\vec{r}) = \frac{1}{\epsilon_0} \rho(\vec{r}) = \nabla \cdot \vec{E}(\vec{r})$	$V(\vec{r}) = \frac{1}{4\pi\epsilon_0} \int_V \frac{\rho(\vec{r}')}{ \vec{r} - \vec{r}' } d^3 r'$
Electric scalar potential $V(\vec{r})$ from a quasistatic current distribution in a medium of conductivity σ	$s(\vec{r}) = -\frac{1}{\sigma} \nabla \cdot \vec{J}(\vec{r})$	$V(\vec{r}) = \frac{1}{4\pi\sigma} \int_V \frac{-\nabla' \cdot \vec{J}(\vec{r}')}{ \vec{r} - \vec{r}' } d^3 r'$
Magnetic scalar potential $V_m(\vec{r})$ from a quasistatic magnetization $\vec{M}(\vec{r})$	$s(\vec{r}) = -\nabla \cdot \vec{M}(\vec{r})$	$V_m(\vec{r}) = \frac{1}{4\pi} \int_V \frac{-\nabla' \cdot \vec{M}(\vec{r}')}{ \vec{r} - \vec{r}' } d^3 r'$
Magnetic induction $\vec{B}(\vec{r})$ from a quasistatic current distribution $\vec{J}(\vec{r})$	For each component B_j $s_j(\vec{r}) = \mu_0 [\nabla \times \vec{J}(\vec{r})]_j$	$B(\vec{r}) = \frac{\mu_0}{4\pi} \int_V \frac{\nabla' \times \vec{J}(\vec{r}')}{ \vec{r} - \vec{r}' } d^3 r'$
Magnetic scalar potential $V_m(\vec{r})$ outside a bounded quasistatic current distribution $\vec{J}(\vec{r})$	$s(\vec{r}) = \frac{1}{2} \vec{r} \cdot [\nabla \times \vec{J}(\vec{r})] = -\nabla \cdot \vec{M}_{\text{eff}}(\vec{r})$	$V_m(\vec{r}) = \frac{1}{4\pi} \int_V \frac{\frac{1}{2} \vec{r}' \cdot [\nabla' \times \vec{J}(\vec{r}')]}{ \vec{r} - \vec{r}' } d^3 r'$

10.2.4.3 Magnetic Multipoles

Given our understanding of the sources of electric and magnetic fields, we can now draw from Ref. [25] to describe these sources and their associated fields in terms of equivalent multipoles. A vector field with zero curl, termed conservative or irrotational, can be described as the negative gradient of a scalar potential $\Psi(\vec{r})$ which satisfies Poisson's equation

$$\nabla^2 \Psi(\vec{r}) = -s(\vec{r}), \quad (10.47)$$

where $s(\vec{r})$ describes the source distribution in terms of another scalar field, and in our case $\Psi(\vec{r})$ can be either $V(\vec{r})$ or $V_m(\vec{r})$. As we saw above, this equation is known to have a solution of the form

$$\Psi(\vec{r}) = \frac{1}{4\pi} \int_V \frac{s(\vec{r}')}{|\vec{r} - \vec{r}'|} d^3r', \quad (10.48)$$

where the integral must be evaluated over all regions where s is nonzero. If the source distribution s can be bounded by a closed surface S , then $\Psi(\vec{r})$ outside of S satisfies Laplace's equation

$$\nabla^2 \Psi(\vec{r}) = 0, \quad \vec{r} \text{ outside of } S, \quad (10.49)$$

which can be solved using multipole expansion techniques. If the surface that most closely bounds the sources is spherical, it is most convenient to use expansions based on Cartesian [26] or spherical coordinates. Nevertheless, from a theoretical perspective, it is interesting to note that, even in spherical geometry, spherical harmonic theory is not required to derive the multipole formalism [27]. If the best bounding surface is, for example, a prolate spheroid, it may be advantageous to use a prolate spheroidal expansion. Here we will consider only the case where the bounding surface is a sphere of radius a , so that

$$\nabla^2 \Psi(\vec{r}) = 0, \quad |\vec{r}| > a. \quad (10.50)$$

There are several equivalent series expansions for Ψ in the region $|\vec{r}| > a$ [28]

$$4\pi \Psi = \sum_{n=0}^{\infty} \sum_{m=0}^n \frac{1}{r^{n+1}} (a_{nm} \cos m\phi + b_{nm} \sin m\phi) P_n^m(\cos \theta) \quad (10.51)$$

$$= \sum_{n=0}^{\infty} p^{(n)} \frac{(-1)^n}{n!} \frac{\partial^n}{\partial l_{n1} \partial l_{n2} \dots \partial l_{nn}} \left(\frac{1}{r} \right) \quad (10.52)$$

$$= \sum_{n=0}^{\infty} \sum_{l=0}^n \sum_{k=0}^{n-l} \frac{(-1)^n}{l!k!(n-l-k)!} c_{nkl} \frac{\partial^n}{\partial x^l \partial y^k \partial z^{n-l-k}} \times \left(\frac{1}{r}\right), \quad (10.53)$$

where $P_n^m(\cdot)$ is an associated Legendre polynomial, r , θ , and ϕ are the spherical coordinates, a_{nm} , b_{nm} , $p^{(n)}$, and c_{nkl} are all coefficients of the expansion, and k , l , n , and m are indices. The index n determines the order of the multipole ($n=0$ is a monopole, $n=1$ is a dipole, *etc.*). In (10.52), $p^{(n)}$ may be interpreted as the magnitude of the n th multipole, which has $3n$ associated direction cosines, $a_{n1}, \beta_{n1}, \gamma_{n1}, \dots, a_{nn}, \beta_{nn}, \gamma_{nn}$, and

$$\frac{\partial}{\partial l_{ni}} = a_{ni} \frac{\partial}{\partial x} + \beta_{ni} \frac{\partial}{\partial y} + \gamma_{ni} \frac{\partial}{\partial z} \quad (10.54)$$

and

$$a_{ni}^2 + \beta_{ni}^2 + \gamma_{ni}^2 = 1. \quad (10.55)$$

The theoretical derivations of Gray [29–31] and Nolte [32] are excellent sources of reference regarding magnetic multipolar expansions, including useful alternative derivations of Ψ based on the scalar, vector, and Debye potentials. In Ref. [27], a spherical tensor approach is employed to derive a multipole expansion similar to (10.53), but involving instead the magnetic vector potential. Reference [25] discusses each expansion in some detail, provides the formulas for each of the coefficients, and determines the relationship of the various expansions. The most important result to come from that discussion is the realization that the intuitively obvious and easy-to-draw Taylor's series multipole expansion includes terms for the quadrupole and higher moments that correspond to externally silent spherical capacitors. These terms are valid representations of particular degrees of freedom of the source distribution, but do not produce external fields. They can be removed in the traceless tensor representation that is derived from the Taylor's series, and are by design absent in the spherical harmonic expansion, which is based in effect upon the representation of the external fields as a solution to Laplace's equation. The distinction between silent and nonsilent in this case is whether one is using the multipoles to represent the source itself, or the associated external fields. A forward calculation must show that a silent component of a source will not contribute to the field; an inverse calculation could never specify a silent source term from the external fields. For this chapter, we will limit ourselves to the spherical harmonic expansion summarized in Table 10.2. This table shows that the expansion can be described as a series of even and odd unit potentials $\Psi_{nm}^e(r)$ and $\Psi_{nm}^o(r)$ multiplied by the corresponding multipole strengths a_{nm} and b_{nm} .

Table 10.2 Spherical harmonic multipole expansion [18]

$$\Psi(\vec{r}) = \sum_{n=0}^{\infty} \sum_{m=0}^n [a_{nm} \Psi_{mn}^e(r)(\vec{r}) + b_{nm} \Psi_{mn}^o(r)(\vec{r})], \quad r > a$$

	Monopole
$\Psi_{00}^e = \frac{1}{4\pi} \frac{1}{r}$	$a_{00} = \int_V s(\vec{r}') d^3 r'$
	Dipole
$\Psi_{10}^e = \frac{1}{4\pi} \frac{z}{r^3}$	$a_{10} = \int_V s(\vec{r}') z' d^3 r'$
$\Psi_{11}^e = \frac{1}{4\pi} \frac{x}{r^3}$	$a_{11} = \int_V s(\vec{r}') x' d^3 r'$
$\Psi_{11}^o = \frac{1}{4\pi} \frac{y}{r^3}$	$b_{11} = \int_V s(\vec{r}') y' d^3 r'$
	Quadrupole
$\Psi_{20}^e = \frac{1}{4\pi} \frac{3z^2 - r^2}{2r^5}$	$a_{20} = \frac{1}{2} \int_V s(\vec{r}') (3z'^2 - r'^2) d^3 r'$
$\Psi_{21}^e = \frac{1}{4\pi} \frac{3xz}{r^5}$	$a_{21} = \int_V s(\vec{r}') x' z' d^3 r'$
$\Psi_{21}^o = \frac{1}{4\pi} \frac{3yz}{r^5}$	$b_{21} = \int_V s(\vec{r}') y' z' d^3 r'$
$\Psi_{22}^e = \frac{1}{4\pi} \frac{3(x^2 - y^2)}{r^5}$	$a_{22} = \frac{1}{4} \int_V s(\vec{r}') (x'^2 - y'^2) d^3 r'$
$\Psi_{22}^o = \frac{1}{4\pi} \frac{6xy}{r^5}$	$b_{22} = \frac{1}{2} \int_V s(\vec{r}') x' y' d^3 r'$
	Octupole
$\Psi_{30}^e = \frac{1}{4\pi} \frac{z}{2r^7} (5z^2 - 3r^2)$	$a_{30} = \frac{1}{2} \int_V s(\vec{r}') z' (5z'^2 - 3r'^2) d^3 r'$
$\Psi_{31}^e = \frac{1}{4\pi} \frac{3x}{2r^7} (5z^2 - r^2)$	$a_{31} = \frac{1}{4} \int_V s(\vec{r}') x' (5z'^2 - 4r'^2) d^3 r'$
$\Psi_{31}^o = \frac{1}{4\pi} \frac{3y}{2r^7} (5z^2 - r^2)$	$b_{31} = \frac{1}{4} \int_V s(\vec{r}') y' (5z'^2 - r'^2) d^3 r'$
$\Psi_{32}^e = \frac{1}{4\pi} \frac{15z}{r^7} (x^2 - y^2)$	$a_{32} = \frac{1}{4} \int_V s(\vec{r}') z' (x'^2 - y'^2) d^3 r'$
$\Psi_{32}^o = \frac{1}{4\pi} \frac{30xyz}{r^7}$	$b_{32} = \frac{1}{2} \int_V s(\vec{r}') x' y' z' d^3 r'$
$\Psi_{33}^e = \frac{1}{4\pi} \frac{15x}{r^7} (x^2 - 3y^2)$	$a_{33} = \frac{1}{24} \int_V s(\vec{r}') x' (x'^2 - 3y'^2) d^3 r'$
$\Psi_{33}^o = \frac{1}{4\pi} \frac{15y}{r^7} (3x^2 - y^2)$	$b_{33} = \frac{1}{24} \int_V s(\vec{r}') y' (3x'^2 - y'^2) d^3 r'$

Four of the source terms listed in Table 10.1 are the divergence of a vector and thus provide the opportunity to simplify the multipole moment integrals listed in Table 10.2. Again following Ref. [18], we find that the moments of the spherical harmonic multipole expansion are of the form

$$A_{nm}^p = \int_V s(\vec{r}') f(\vec{r}') d^3 r', \quad (10.56)$$

where p is either e or o , A_{nm}^e is a_{nm} , A_{nm}^o is b_{nm} , and $f(\vec{r}')$ is the weight function which is different for each moment. When we consider the sources s that are the negative divergence of a vector field \vec{F} , *i.e.*, $s = -\nabla \cdot \vec{F}$, (10.56) can be written as

$$A_{nm}^p = - \int_V f(\vec{r}') \nabla' \cdot \vec{F}(\vec{r}') d^3 r'. \quad (10.57)$$

The vector identity

$$f \nabla \cdot \vec{F} = \nabla \cdot (f \vec{F}) - \vec{F} \cdot \nabla f \quad (10.58)$$

can be used to rewrite (10.57) as

$$A_{nm}^p = - \int_V \nabla \cdot (f \vec{F}) d^3 r' + \int_V \vec{F} \cdot \nabla f d^3 r'. \quad (10.59)$$

The first integral vanishes when it is transformed into a surface integral outside the source region. Thus the moments reduce to the simpler form

$$A_{nm}^p = - \int_V \vec{F} \cdot \nabla f d^3 r' \quad (10.60)$$

which is tabulated in Table 10.3. As an example, the dipole moment \vec{m} for a distributed magnetization \vec{M} is greatly simplified by this technique

$$\vec{m} = - \int_V \nabla' \cdot \vec{M}(\vec{r}') \vec{r}' d^3 r' = \int_V \vec{M}(\vec{r}') d^3 r'. \quad (10.61)$$

The field at \vec{r} produced by a dipole located at \vec{r}' is obtained by computing the gradient of the dipole potentials in Table 10.3

$$\vec{B}(\vec{r}) = -\nabla \Psi(\vec{r}) = \frac{\mu_0}{4\pi} \left(\frac{3\vec{m} \cdot (\vec{r} - \vec{r}')}{|\vec{r} - \vec{r}'|^5} (\vec{r} - \vec{r}') - \frac{\vec{m}}{|\vec{r} - \vec{r}'|^3} \right). \quad (10.62)$$

Table 10.3 Spherical harmonic multipole strengths [18] in terms of dipole density S

$$A_{nm}^p = \int_V S(\vec{r}') \cdot \nabla f(\vec{r}') d^3 r'$$

Monopole	$a_{00} = \int_V \nabla \cdot S(\vec{r}') d^3 r' = 0$
Dipole	$a_{10} = \int_V S_z(\vec{r}') d^3 r'$ $a_{11} = \int_V S_x(\vec{r}') d^3 r'$ $b_{11} = \int_V S_y(\vec{r}') d^3 r'$
Quadrupole	$a_{20} = \int_V [3z'S_z(\vec{r}') - \vec{r}' \cdot S(\vec{r}')] d^3 r'$ $a_{21} = \int_V [x'S_z(\vec{r}') + z'S_x(\vec{r}')] d^3 r'$ $b_{21} = \int_V [y'S_z(\vec{r}') + z'S_y(\vec{r}')] d^3 r'$ $a_{22} = \frac{1}{2} \int_V [x'S_x(\vec{r}') - y'S_y(\vec{r}')] d^3 r'$ $b_{22} = \frac{1}{2} \int_V [x'S_y(\vec{r}') + y'S_x(\vec{r}')] d^3 r'$
Octupole	$a_{30} = \frac{3}{2} \int_V [S_z(\vec{r}') (5z'^2 - r'^2) - 2z'r' \cdot S(\vec{r}')] d^3 r'$ $a_{31} = \frac{1}{4} \int_V [S_x(\vec{r}') (5z'^2 - r'^2) + 2x' (5z'S_z(\vec{r}') - S(\vec{r}') \cdot \vec{r}')] d^3 r'$ $b_{31} = \frac{1}{4} \int_V [S_y(\vec{r}') (5z'^2 - r'^2) + 2y' (5z'S_z(\vec{r}') - S(\vec{r}') \cdot \vec{r}')] d^3 r'$ $a_{32} = \frac{1}{4} \int_V [2z' (x'S_x(\vec{r}') - y'S_y(\vec{r}')) + S_z(\vec{r}') (x'^2 - y'^2)] d^3 r'$ $b_{32} = \frac{1}{2} \int_V [y'z'S_x(\vec{r}') + x'z'S_y(\vec{r}') + x'y'S_z(\vec{r}')] d^3 r'$ $a_{33} = \frac{1}{8} [(x'^2 - y'^2)S_x(\vec{r}') - 2x'y'S_y(\vec{r}')] d^3 r'$ $b_{33} = \frac{1}{8} [2x'y'S_x(\vec{r}') + (x'^2 - y'^2)S_y(\vec{r}')] d^3 r'$

The end result of this exercise is a series of dipole pictures for the spherical harmonic multipole series, as shown in Figure 10.6. It is important to recognize that in the limit as the dipole spacing becomes small, the two alternative configurations, shown for example by the black and gray arrows in a_{21} , produce the same field. We will address the implications of these pictures when we later discuss the information content of biomagnetic signals.

If an electric or magnetic source consists of N dipoles \vec{M}_a at locations $\vec{r}_a (a = 1, N)$, then it is straightforward to relate this model to a multipole series computed about the origin [19, 28]. For a single magnetic dipole \vec{m} at the point \vec{r} , the magnetization is given by

$$\vec{M}(\vec{r}) = \vec{m} \delta(\vec{r} - \vec{r}) , \tag{10.63}$$

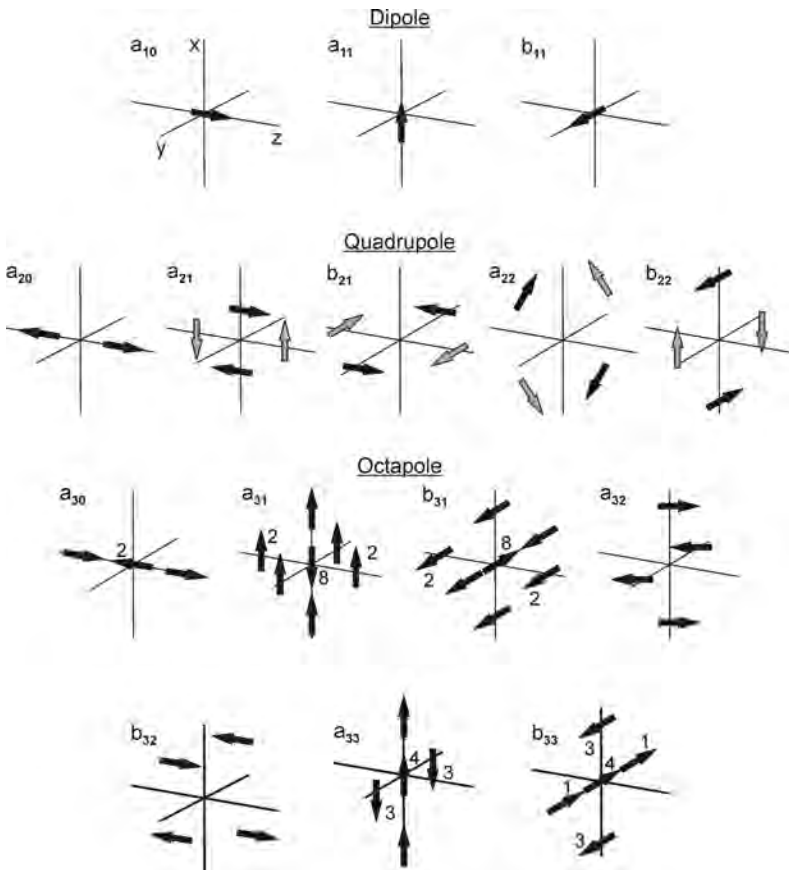


Fig. 10.6 The dipole models that correspond to the various multiple moments in Tables 10.2 and 10.3. The gray and black arrows in the quadrupole moments describe two current source distributions that are electrically identical but magnetically different. (Adapted from Ref. [18], with permission.)

where $\delta(\vec{r} - \vec{r}')$ is the Dirac delta function. Substitution of this into the integrals in Table 10.3 can be used to obtain the dipole through octapole moments of a dipole displaced from the origin [18].

10.2.4.4 Current Multipoles in Conducting Media

The advantage of the multipole approach is that it provides a mathematically compact, orthogonal description of a source distribution, which is particularly advantageous in an inverse calculation. Moreover, it has been pointed out in the literature [33–35] that the classic equivalent current dipole model can sometimes lead to dangerous oversimplification of the inverse problem, partly because dipoles alone describe spatially extended sources rather poorly. We refer the reader to the work of Mosher *et al.* [33, 34, 36] for excellent and up-to-date reviews of MEG forward modeling using multipole expansions.

The challenge is to establish an appropriate interpretation of the higher order multipole moments. To explore the relationship between multipole moments and distributed dipole sources, we draw from a detailed discussion of the uniform double-layer model [22].

Figure 10.7 shows a schematic representation of a cardiac activation wave front. In the uniform double-layer model of cardiac activation, the active sources of the cardiac electric and magnetic fields are constrained to an expanding wave front, which is assumed to be thin, and have an impressed current density \vec{j}^i that is everywhere uniform and perpendicular to the wave front [37]. It is termed a double layer because current is injected by the wave front into the medium at the outer surface, and withdrawn with an equal strength at the inner one. In this case, the solid angle theorem [23] states that the electric potential at any point in an infinite, homogeneous conductor containing such a uniform double-layer source is determined by the solid angle subtended by the rim of the double layer. The projected area of this rim is proportional to the dipole moment of this source and field; the curvature and detailed shape of the rim contribute to the quadrupole and higher moments [22]. It also follows that the external potential is independent of any perturbations of the layer that do not affect the shape or location of the rim, in that they are equivalent to the addition or subtraction of closed double layers, which are equivalent to externally silent, spherical capacitors. If the origin of the multipole series does not correspond to the center of the surface enclosed by the rim, there will be additional terms to the multipole expansion that are described by the dipole shift equations [18, 28]. Conversely, the center of the wave front can in principle be located by determining the location for the multipole origin that minimizes higher order moments [22]. Interpretation is even more complicated when, late in cardiac depolarization, the wave front expands until it breaks through the epicardial surface, adding a second, or third rim to the wave front, each with its own shifted multipole series!

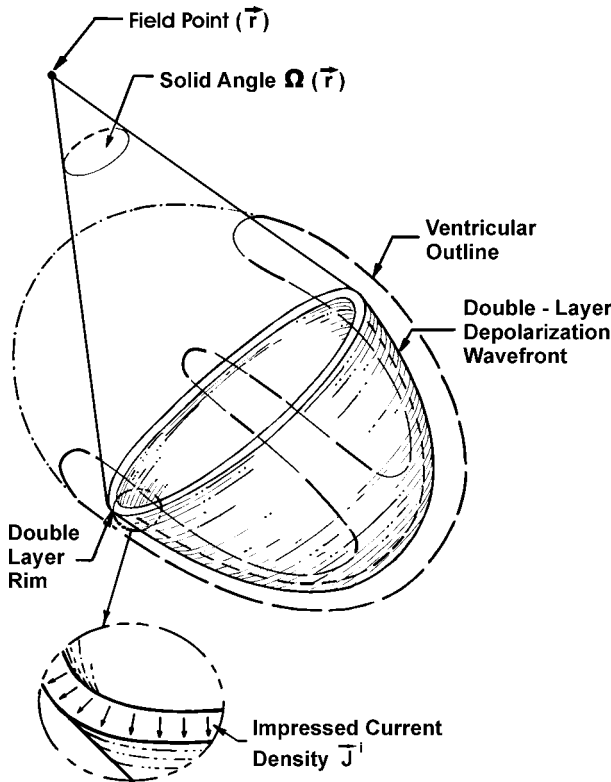


Fig. 10.7 The double-layer model of ventricular activation. (Adapted from Ref. [22], with permission.)

Given the difficulty in picturing the rim topology that corresponds to higher order moments, it is tempting to ignore multipole series from the outset and use only a distributed dipole source, as shown in Figure 10.8. While this approach provides a straightforward means of computing the electric and magnetic fields from *a priori* knowledge of the spatiotemporal behavior of the wave front, we will show later in the chapter that it fails as an inverse model because the dipoles are not independent or orthogonal. As discovered when first attempted by Holt *et al.* [38–40], there are instabilities in the solutions that correspond to the addition and subtraction of dipole representations of spherical capacitors. Perturbing one dipole can be balanced by a corresponding antiperturbation of all other dipoles. The obvious solution is to constrain the orientation of the dipole, through quadratic programming, so that their orientation cannot reverse. This corresponds to the addition of physiological constraints to a model, something that has been popular in MEG analyses of cortical sources.

While the preceding discussion was directed towards cardiac sources, it applies equally well to distributed sources in the brain and gastrointestinal (GI) system,

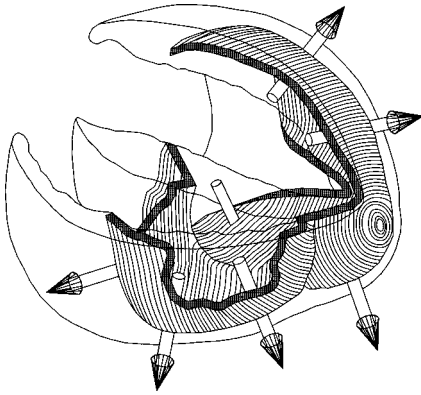


Fig. 10.8 A multiple-dipole representation of the cardiac activation.
(Adapted from Ref. [243], with permission.)

which can have a significant spatial extent [41]. The issue of MEG sensitivity to cortical sources as a function of their depth is addressed in work of Hillebrand [42] and Okada [43, 44]. Fourier inverse techniques, discussed in a later section, have been used to determine how the magnetic field of cortical sources is affected by their linear extent [45–48]. It has also been shown that higher order current multipole coefficients can provide supplementary information on characteristics of the source, in addition to the location and magnitude of the source extracted from the dipolar terms. There is an increasing body of evidence suggesting that multipole fitting in realistic head models may be required to accurately estimate and characterize neuronal activity [49]. Specifically, quadrupoles can be related to source curvature and octapoles to spatial extent. However, large (yet feasible) signal-to-noise ratios (SNRs) are required to detect such components. For example, using a 49-channel SQUID system, the highest SNR should be of the order of 60 to detect a spatial extent of 20 mm.

The application of forward and inverse models to the study of the GI system was pioneered by Allescher et al. [50] and by Irimia and Bradshaw [51–53], who showed that inverse solutions can be used to detect the pathological uncoupling of electric sources due to gastroparesis and ischemia. In spite of considerable progress in this area, solving the GI inverse problem remains difficult, mainly because the system being studied has a large spatial extent and is populated with many distinct sources that have very different frequency characteristics.

10.3

The Magnetic Inverse Problem

10.3.1

Introduction

Given our brief introduction to the magnetic forward problem, we now address the inverse problem of determining sources from fields. We showed above that the magnetic field represents a convolution of a source distribution with a Green's function. In this light, the inverse problem simply reduces to the deconvolution of these convolution integrals. Therein lies the challenge.

10.3.2

Inverting the Law of Biot and Savart

10.3.2.1 Nonuniqueness of Inverse Solutions

The fundamental difficulty in magnetic imaging of currents is that there is no unique solution to the inverse problem of determining the three-dimensional current distribution in (10.14) from the measurements of the magnetic field outside of the object. As mentioned in Section 10.1, the easiest proof of nonuniqueness is to note that it is possible to superimpose on any three-dimensional current distribution another source distribution that is magnetically silent, such as when the radial internal currents of a spherically symmetric battery are superimposed upon an infinite, homogeneous conductor. This is exactly analogous to the electrostatic case where there is no electric field outside a spherical capacitor formed by a pair of concentric spherical shells carrying opposite charge. In an electrostatics inverse problem, spherical capacitors of arbitrary radius, charge, and sphere separation can be added or subtracted from the source distribution without changing the potentials measured on the surface that bounds all sources. Hence, any attempt to solve such an inverse problem will be unable to determine which spherical capacitor configurations exist, and which do not. Constraints might be used to prevent the inverse algorithm from creating spherical capacitors *de novo*, but there is a whole class of higher-order silent sources. As we saw above, the spherical harmonic multipole solution to Laplace's equation is designed specifically to eliminate those silent sources [18, 25]. The usual approach to this problem for either the electric or magnetic inverse is to restrict the possible sources and invert the resulting set of constrained equations.

In contrast to the three-dimensional current-imaging problem, the two-dimensional problem does have a unique inverse. As we shall see in this chapter, there is a wide variety of inverse algorithms for magnetic imaging of two-dimensional current distributions, including spatial filtering, dipole fitting, the Hosaka-Cohen transformation, alternating projections, lead-field analysis, the finite-element method, and blind deconvolution. While there may be a unique inverse solution, even the two-dimensional inverse problem can be ill-conditioned, in that the abil-

ity to determine the inverse solution with the desired accuracy or spatial resolution can be strongly dependent upon measurement noise, source-detector distance, and the exact nature of the source current distribution. We shall show that this can be overcome in part by applying constraints to limit the effects of noise or to utilize most fully *a priori* knowledge of the current distribution.

10.3.2.2 The Spatial Filtering Approach

The most elegant method to obtain a two-dimensional current image from a magnetic field map is to use Fourier-transform deconvolution (inversion) of the law of Biot and Savart [54–59]. Following the notation of Roth [56], let us assume that we are imaging the magnetic field produced by a two-dimensional current $\vec{J}(x, y)$ distributed through a slab of conducting material of thickness d that extends to infinity in the xy -plane. We shall assume that we measure the component B_x at a height $z \gg d$, so that we can integrate (10.14) over z' and immediately obtain⁴⁾

$$B_x(x, y, z) = \frac{\mu_0 d}{4\pi} z \int_{-\infty}^{\infty} \int_{-\infty}^{\infty} \frac{J_y(x', y')}{[(x - x')^2 + (y - y')^2 + z^2]^{3/2}} dx' dy'. \quad (10.64)$$

We can write this equation as the convolution of the current distribution with a Green's function that represents the magnetic source-to-field transfer function:

$$B_x(x, y, z) = \int_{-\infty}^{\infty} \int_{-\infty}^{\infty} J_y(x', y') G((x - x'), (y - y'), z) dx' dy', \quad (10.65)$$

where the Green's function is given by

$$G((x - x'), (y - y'), z) = \frac{\mu_0 d}{4\pi} \frac{z}{[(x - x')^2 + (y - y')^2 + z^2]^{3/2}}. \quad (10.66)$$

Rather than computing this through integration in Cartesian space, we can instead compute the spatial Fourier transform (FT)⁵⁾ of J_y using the fast Fourier transform (FFT) or more accurate techniques [60], so that

- 4) Hereafter, when we are discussing the two-dimensional current image, we shall assume that the sample has a thickness d that is negligible compared to z , so that \vec{J} has neither a z -component nor z -dependence. Thus, we shall be able to use the standard current density \vec{J} , with units of amperes/meter², rather than a two-dimensional equivalent. The thickness d will be written explicitly in the equations. $\vec{J}d$ is simply a two-dimensional current density with units of amperes/meter.

- 5) We use the following definition of the two-dimensional Fourier transform pair in this chapter:

$$f(k_x, k_y) = \int_{-\infty}^{+\infty} \int_{-\infty}^{+\infty} F(x, y) e^{-i(k_x x + k_y y)} dx dy$$

$$F(x, y) = \frac{1}{(2\pi)^2} \int_{-\infty}^{+\infty} \int_{-\infty}^{+\infty} f(k_x, k_y) e^{i(k_x x + k_y y)} dk_x dk_y$$

This may lead to slight differences between some of the equations presented herein and those in the original papers.

$$j_y(k_x, k_y) = FT\{J_y(x, y)\}. \quad (10.67)$$

Similarly, we can write

$$b_x(k_x, k_y, z) = FT\{B_x(x, y, z)\}. \quad (10.68)$$

The Green's function has the Fourier transform [56]

$$g(k_x, k_y, z) = \frac{\mu_0 d}{2} e^{-z\sqrt{k_x^2 + k_y^2}}, \quad (10.69)$$

where $k_x = 2\pi/x$ and $k_y = 2\pi/y$ are the spatial frequencies, in m^{-1} , in the x and y directions. We can then use the convolution theorem to write the law of Biot and Savart as a simple multiplication in the spatial frequency domain

$$b_x(k_x, k_y, z) = g(k_x, k_y, z)j_y(k_x, k_y). \quad (10.70)$$

This process allows us to start with a known y component of the current density, $J_y(x, y)$, and then calculate the x component of the magnetic field, $B_x(x, y, z)$. Note that the spatial filter that corresponds to the magnetic forward problem, g , falls exponentially with both k and z , so that the high-spatial-frequency contributions to the current distribution are attenuated in the magnetic field, *i.e.*, the Green's function acts as a spatial low-pass filter. The farther the magnetometer is from the current distribution, the harsher is the filtering.

Inverse Spatial Filtering

A supposedly simple division allows us to solve (10.70) for $j_y(k_x, k_y)$ and hence solve in Fourier space the inverse imaging problem of determining \vec{J} from \vec{B}

$$j_y(k_x, k_y) = \frac{b_x(k_x, k_y, z)}{g(k_x, k_y, z)}. \quad (10.71)$$

The desired image of $J_y(x', y')$ is obtained with the inverse Fourier transform

$$J_y = FT^{-1}\{j_y(k_x, k_y)\}. \quad (10.72)$$

A similar set of equations would allow us to determine J_x from a map of B_y . This inverse solution is unique [56].

As we shall see in more detail shortly, the problem with this inverse process, in general, is in the division in (10.71). If g is small, but nonzero, at spatial frequencies for which $1/g$ is large, j_y tends toward infinity. Unfortunately, g falls exponentially with k , so that $1/g$ diverges exponentially. Since noise is always present in experimental data, b_x is certainly nonzero at high frequencies, even if the theoretical magnetic field associated with the source does not contain high-spatial-fre-

quency components. Therefore, (10.71) is destined to “blow up” due to excessive amplification of noise. Before we see how this can be avoided, it is useful to look at the z component of the field.

From (10.17), it follows that the Fourier transform of B_z is [56]

$$b_z(k_x, k_y, z) = i \frac{\mu_0 d}{2} e^{-z\sqrt{k_x^2 + k_y^2}} \left(\frac{k_x j_y(k_x, k_y)}{\sqrt{k_x^2 + k_y^2}} - \frac{k_y j_x(k_x, k_y)}{\sqrt{k_x^2 + k_y^2}} \right). \quad (10.73)$$

This shows us, in general, that a single image of B_z would be inadequate to determine both J_x and J_y , and would provide only a linear combination of the two. However, if we assume that the current distribution is continuous, it must have zero divergence in the quasistatic limit, *i.e.*,

$$\nabla \cdot \vec{J}(x, y) = 0. \quad (10.74)$$

For two-dimensional current with no source or sinks, this reduces to

$$\frac{\partial J_x}{\partial x} + \frac{\partial J_y}{\partial y} = 0. \quad (10.75)$$

If we compute the Fourier transform of this equation, we then have the added constraint

$$ik_x j_x(k_x, k_y) + ik_y j_y(k_x, k_y) = 0, \quad (10.76)$$

which allows us to solve (10.73) for either J_x or J_y and then use the continuity equation to obtain the other. While this procedure works well for planar current distributions, it may not be applicable for mapping effective surface currents on the upper boundary of three-dimensional current distributions in thick objects, since current flowing on the surface can disappear as J_z into the bulk conductor of the object without affecting B_z .

Noise and Windowing

We now can address briefly the issue of noise and windowing, which is treated in greater detail elsewhere for two-dimensional imaging [56], for fetal MCG noise removal [61], and for cylindrical models of the head [45, 47, 48] and abdomen [62]. The value of j_y in (10.71) will diverge if there is noise in the absence of signal, *i.e.*, if the denominator goes to zero faster than does the numerator. However, because the noise in a SQUID measurement is white at high temporal frequencies, a scanned SQUID image will have white noise at high spatial frequencies. The low-pass characteristic of the law of Biot and Savart is manifest as a Green’s function that tends towards zero exponentially at high spatial frequencies, so that an unstable inverse is almost guaranteed except in cases where the magnetometer is very close to the current distribution. The solution to this dilemma is to filter spatially the magnetic field data by eliminating all contributions at high spatial frequencies, so that the numerator is identically zero above a frequency k_c . The pro-

cess of low-pass filtering in the frequency domain (or windowing in the temporal domain) will ensure a stable inverse, but at the cost of losing high-spatial-frequency information.

The steps in this process, and how it affects the image quality, are shown in Figures 10.9 and 10.10, in which we simulate the forward problem of conversion of a current source distribution into a magnetic field map (down the left column) and, after adding noise, the inverse problem of converting the field map into a reconstructed source image (up the right column), which includes the windowing that is usually required to provide a stable inverse solution.

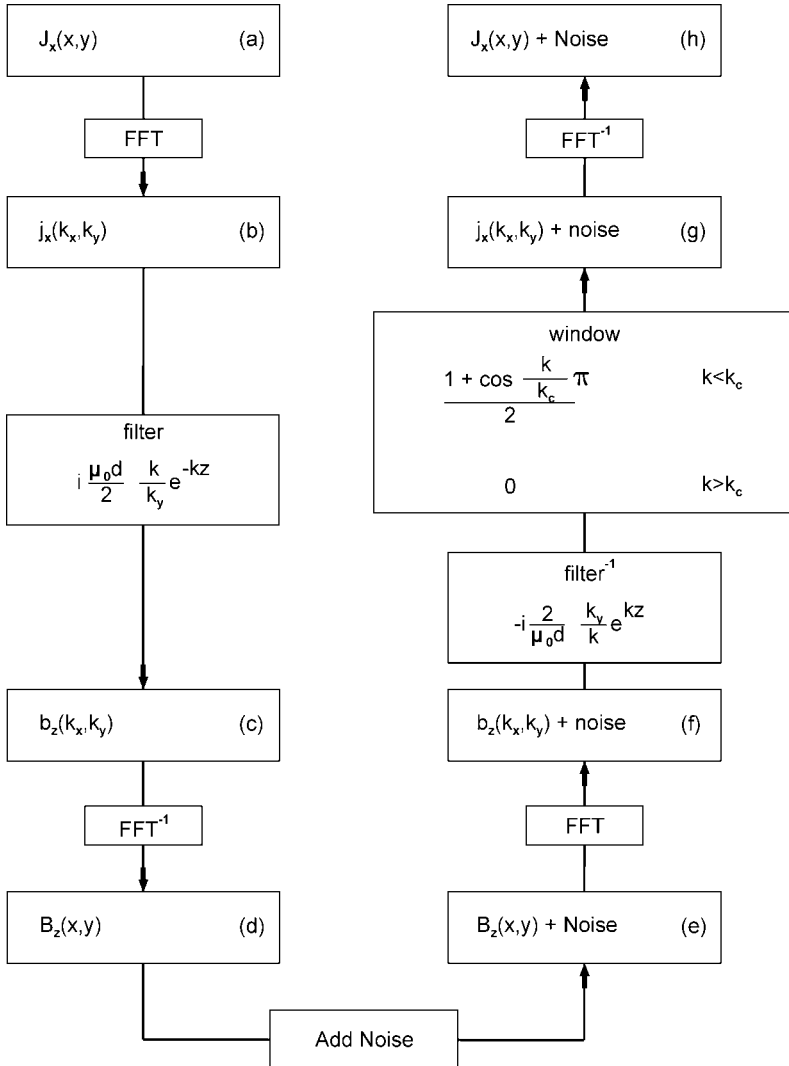


Fig. 10.9 Schematic outlining the forward and inverse Fourier imaging process. (Adapted from Ref. [56], with permission.)

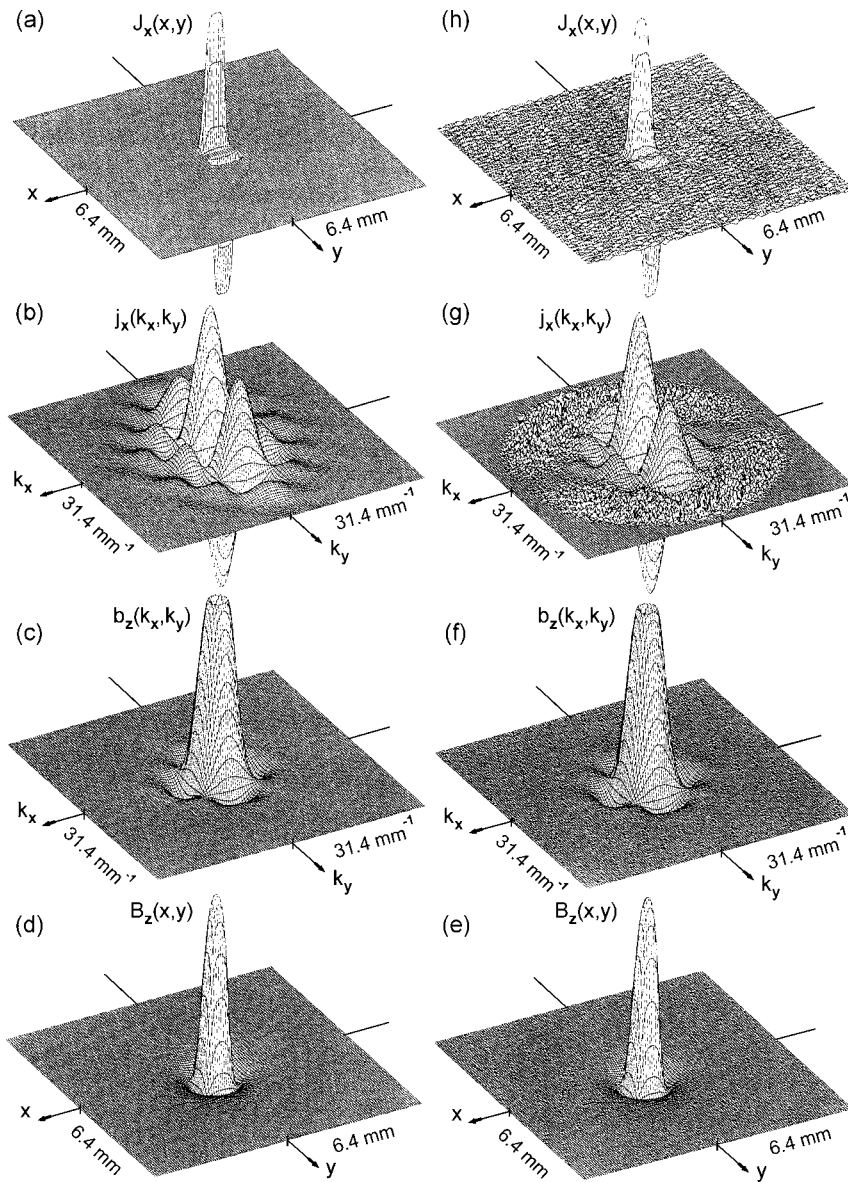


Fig. 10.10 Forward and inverse spatial filtering/Fourier transform calculations for $z = 0.3$ mm. See text for details. (Adapted from Ref. [56], with permission.)

In Figure 10.10(a), we start with the x component of the current density, $J_x(x, y)$, for a square loop of current and compute in Figure 10.10(b) the imaginary part of the Fourier transform of $J_x(x, y)$, i.e., $j_x(k_x, k_y)$. The real part of the Fourier transform of $B_z(x, y, z)$, $b_z(k_x, k_y)$, at $z = 0.3$ mm is shown in Figure 10.10(c), and

from this we compute in Figure 10.10(d) the z -component of the magnetic field, $B_z(x, y, z)$, with peak amplitude of 756 pT. To simulate measurement noise in Figure 10.10(e), we add to B_z in Figure 10.10(d) a 0.5-pT amplitude white noise. From this, we compute the real part of the Fourier transform of B_z with added noise in Figure 10.10(f), the imaginary part of the Fourier transform of the J_x image multiplied by a Hanning window with a low-pass filter with $k_c = 30 \text{ mm}^{-1}$ (Figure 10.10(g)), to produce in Figure 10.10(h) the current-density image J_x .

Figure 10.11 shows a comparison of the results of the spatial filtering/Fourier transform inverse approach for equivalent theoretical and experimental images for a current test pattern. This magnetic imaging approach is the basis for extensive work on the magnetic detection of current distributions within integrated circuits [63, 64].

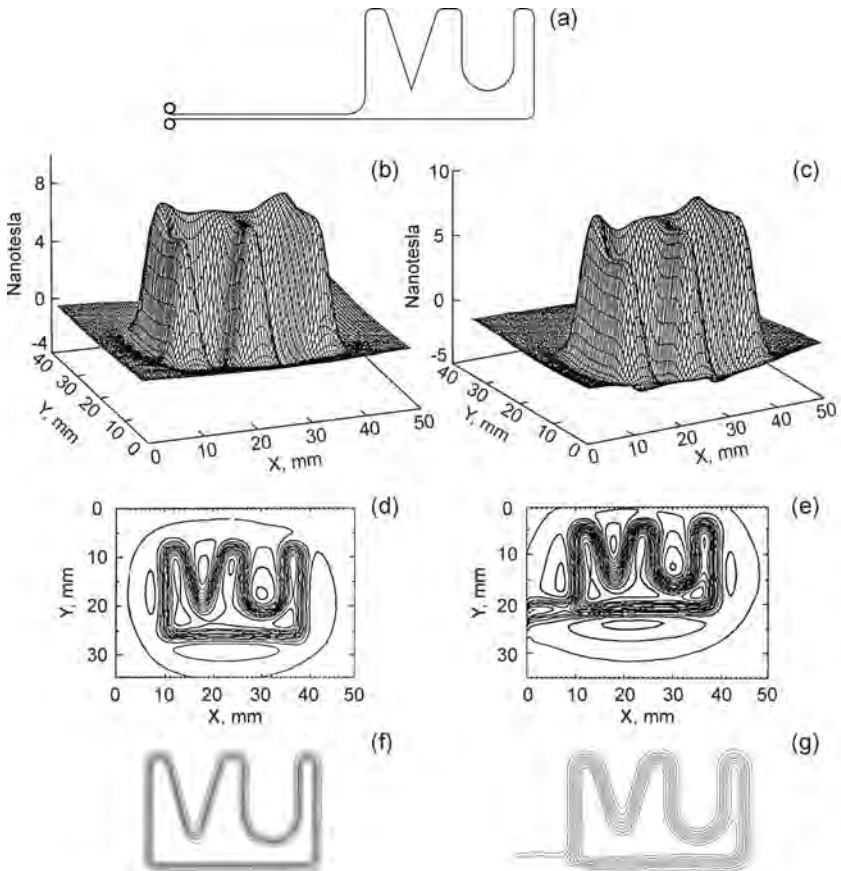


Fig. 10.11 Magnetic imaging of a current pattern: (left) theoretical and (right) experimental images. (a) The source current; (b) and (c) surface plots of the magnetic field; (d) and (e) isocontour plots; and (f) and (g) the deconvolved current images. (Adapted from Ref. [244], with permission.)

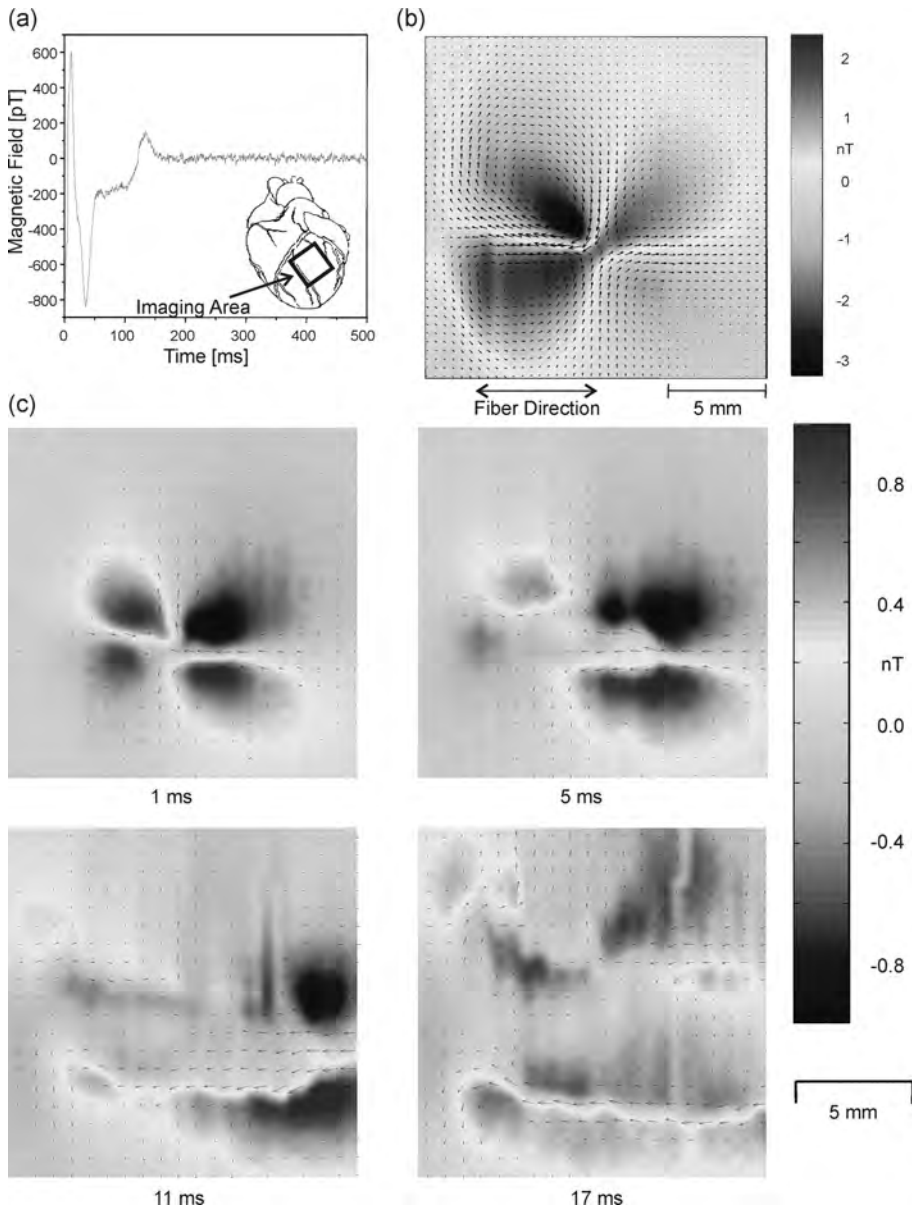


Fig. 10.12 Magnetic imaging of cardiac action currents. (a) MCG taken at a location on the scanning grid. Inset: anterior view of the heart showing the location of the $16 \times 16 \text{ mm}^2$ scanning area. (b) Magnetic field resulting from a cathodal stimulus current of 1.5 mA. The overlaid arrows schematically represent the current distribution under the assumption of two-dimensional sheet currents as determined by inverse Fourier

imaging. (c) Magnetic fields generated by the propagation of action currents resulting from a cathodal point stimulus. The arrows show schematically the current distribution. The octupolar pattern with four current loops can be explained in the framework of a bidomain model with an unequal anisotropy ratio in the intra- and extracellular space. (Adapted from Ref. [174], with permission.)

Figure 10.12 shows a magnetic field map obtained with the original Micro-SQUID magnetometer and the corresponding current image for a slice of isolated cardiac tissue [65, 66]. These measurements provided some of the first proof that cardiac tissue is best described by bidomain models⁶⁾ with unequal anisotropy ratios in the intracellular and extracellular spaces [67].

Magnetometer Separation

The trade-off between stability of the inverse and the cutoff of high spatial frequencies is unfortunate, in that the presence of noise limits the ability to enhance the spatial resolution of a current image obtained with a distant magnetometer. Figure 10.13 shows how the quality of an image is degraded as the magnetometer is moved away from the source distribution. The mean square deviation (MSD) of the image from the modeled source is 0.03 at 0.1 mm with $k_c = 10 \text{ mm}^{-1}$ (Figure 10.13(a)); 0.07 at 0.3 mm with $k_c = 30 \text{ mm}^{-1}$ (Figure 10.13(b)); 0.44 at 1.0 mm with $k_c = 10 \text{ mm}^{-1}$ (Figure 10.13(c)); and 0.95 at 3 mm with $k_c = 3 \text{ mm}^{-1}$ (Figure 10.13(d)).

The primary strengths of the technique are the speed with which the field map can be deconvolved and the ease with which it can be low-pass filtered: a fast Fourier transform of the data is computed, the data are multiplied in the frequency domain by the low-pass filtered Green's function, and the inverse FFT is computed. For a particular measurement geometry, the Green's function needs to be computed only once.

Apodizing

The discussion so far has assumed that the magnetic field is measured at a point. In practice, SQUID magnetometers have pickup coils whose diameter is comparable to the spacing between the coil and the sample, consistent with optimizing the trade-offs between sensitivity and spatial resolution [68]. Since the SQUID measures flux, the pickup coil integrates the magnetic field that threads the coil, and thus the shape of the coil is convolved with the field distribution in a manner that results in further low-pass spatial filtering of the field. The relationship between coil diameter, spatial resolution, and sensitivity is nontrivial. A spatial-filtering analysis can be used to show that a noisier (less sensitive), smaller pickup coil placed close to a sample can in certain circumstances provide better images than a larger, quieter SQUID further away [69, 70].

6) The bidomain model of cardiac tissue addresses the limitations of the uniform double-layer model by treating cardiac tissue as an active, anisotropic, three-dimensional cable, in which the intracellular and extracellular spaces of the interconnected (syncytial) cardiac cells, with their differing electrical anisotropies, are separated by the nonlinear membrane that serves as the current source that drives action currents from the intracel-

lular to extracellular spaces, and vice versa. The double-layer representation corresponds to what would be seen in the extracellular space alone: the appearance and disappearance of the current from opposite surfaces of the wave front. The bidomain model casts this in terms of known membrane electrophysiology and homogenizes the problem to avoid the details of individual cells.

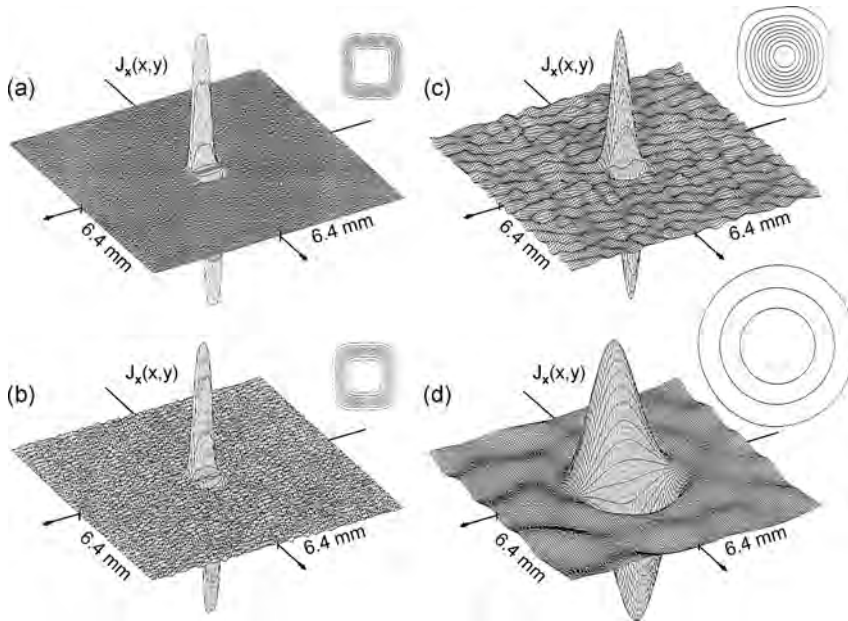


Fig. 10.13 Spatial filtering/Fourier transform inverse image of the current density for four different values of $h(k_x, k_y)$, calculated from the $e^{-\alpha^2 r^2}$ component of the magnetic field produced by the square current loop used in the simulations of Fig. 10.10 after magnetometer noise of 0.5 pT has been added to the

magnetic field. Plots of both $J_x(x, y)$ and the current lines (upper right inset) are shown. Each line corresponds to 0.1 μA , except in (d), where each line is 0.05 μA . (a) $z = 0.1$ mm, (b) 0.3 mm, (c) 1.0 mm, (d) 3.0 mm. (Adapted from Ref. [56], with permission.)

One would suspect that a deconvolution approach could be used to eliminate the effect of the finite coil area. The image processing approach can be extended to examine and correct for the effects of finite-diameter pickup coils [71]. We discuss the flux-field deconvolution in greater detail later in this chapter. For a SQUID with a finite-diameter pickup coil, the magnetic field B_z will be convolved with the spatial sampling (or turns) function H of the coil to give the detected flux Φ . Figure 10.14 shows four different pickup coils [71]. In Fourier space, the magnetic field distribution from the sample $b(k_x, k_y)$ will be multiplied by the turns function $h(k_x, k_y)$ to give the flux $\phi(k_x, k_y)$. Ideally, the effect of the coil could be corrected by dividing $\phi(k_x, k_y)$ by $h(k_x, k_y)$ to obtain $b(k_x, k_y)$, so that an inverse Fourier transform would give the coil-corrected B_z . Unfortunately, for typical coils, the edges of the coil introduce zeros in their spatial frequency transfer function, $h(k_x, k_y)$, which complicate deconvolution of the images at high spatial frequencies: the zero in the forward transfer function produces an infinity in the inverse function, making it difficult to obtain any information from the field at or even near that spatial frequency. This could be ameliorated with windowing, as before, but this leads once again to the loss of high-frequency information instead of to

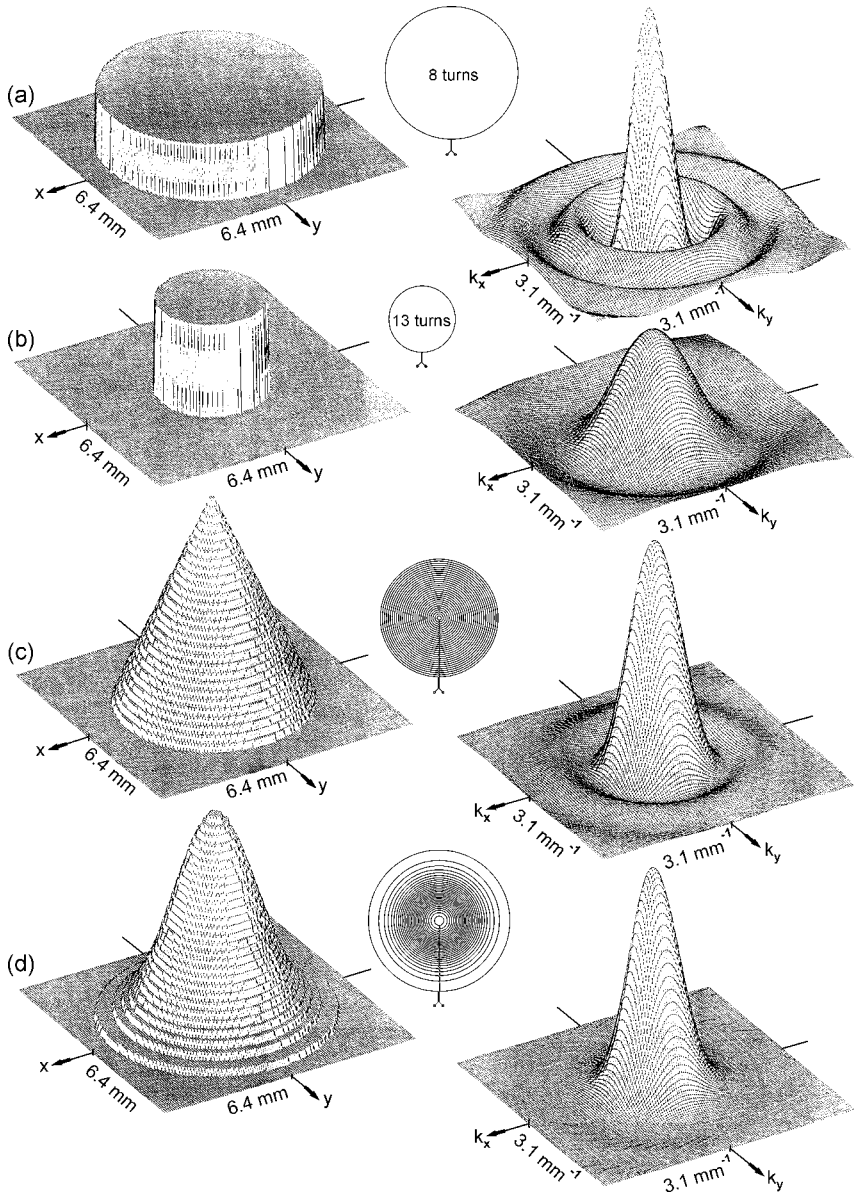


Fig. 10.14 Four SQUID pickup coils with different separations of the turns. Left: the turns function $H(r)$; middle: the coil; right: the Fourier transform of the turns function $h(k_x, k_y)$. The coils are (a) 8 turns with a

5-mm diameter, (b) 13 turns with a 2.5-mm diameter, (c) a pancake coil with 29 turns, and (d) an apodized coil with 29 turns and a turns functions given by $e^{-a^2 r^2}$. (Adapted from Ref. [71], with permission.)

the desired extent of resolution enhancement. As shown in Figure 10.15, even with windowing, the contribution near the zeros produces spikes that appear in the frequency domain at the edge of the window, and these spikes produce noise in the spatial images.

A solution to this problem that has been demonstrated theoretically [71] but not yet implemented is to adjust the spacing of individual turns in a planar coil, so that the zeros in the transfer function

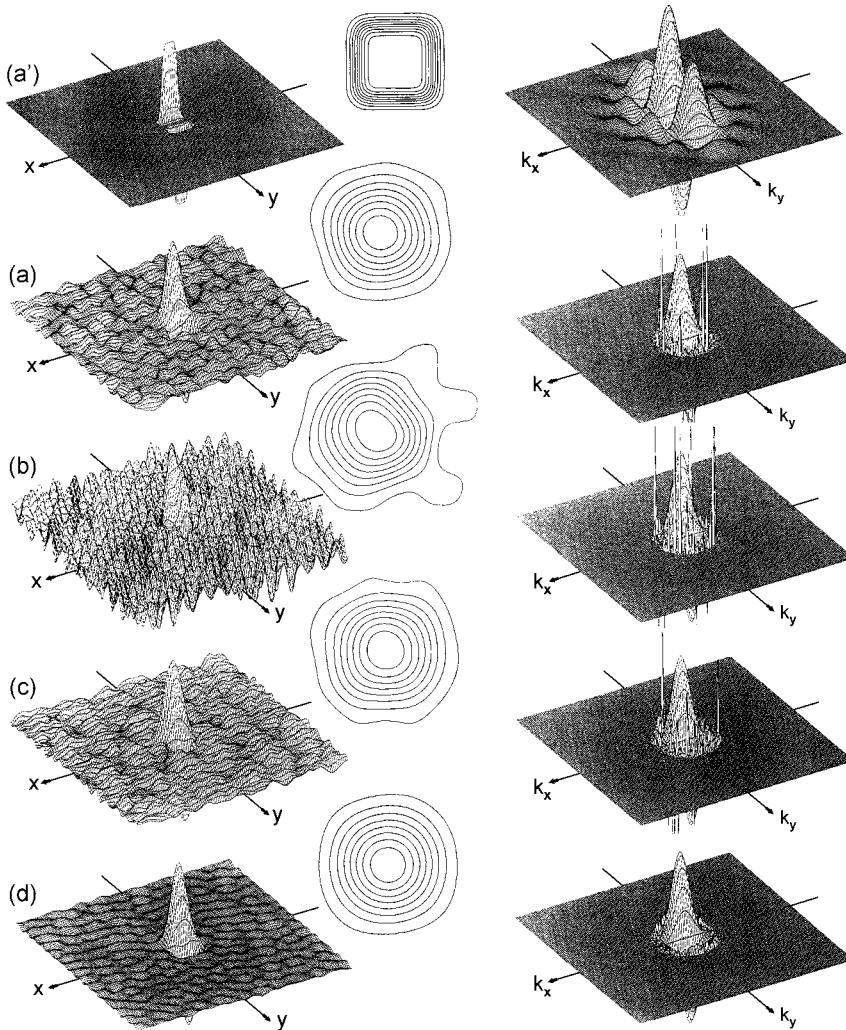


Fig. 10.15 A comparison of the imaging ability of the four different SQUID pickup coils in Fig. 10.14. Left: the x -component of the current density; center: current lines of the image of the current; right: the imaginary part of the

Fourier transform of the current density images. The source current is (a'), and (a)–(d) are the density images from the four coils. (Adapted from Ref. [71], with permission.)

$h(k_x, k_y)$, shown in the right-hand column, are either eliminated or forced to very high spatial frequencies. This process, termed apodizing, could provide a significant enhancement in spatial resolution for certain SQUID imaging applications, particularly SQUID microscopy.⁷ Figure 10.15 illustrates the process. Figure 10.15(a') shows the x -component of a 5 mm square current loop with a 0.75 mm Gaussian width (left), the image of these currents (center), and the spatial Fourier transform of the current. We then used this current to compute magnetic fields at a height of 5 mm above this loop, with a current noise of 15 pA and a k_c of 1.8 mm^{-1} . The current image in Figure 10.15(d) from the apodized coil has lower noise yet provides excellent spatial resolution, despite the fact that the apodized coil has a larger outer diameter than the other three coils.

Estimation of the Maximum Spatial Frequency

While the Nyquist sampling limit is well understood for time-series signal analysis, the extension of this concept to spatial frequencies of magnetic field distribution deserves some explanation, particularly with regard to the complementary issues of maximum spatial frequency in the measured magnetic field, and the spatial sampling generally used in measuring it. The estimation of the maximum spatial frequency of the magnetic field produced by a particular source configuration is of utmost importance, as it determines whether severe information loss happens in the field integration along the coils of a SQUID sensor. In addition, it determines the region in the spatial frequency plane over which the deconvolution has to be calculated and it imposes restrictions on the step size of the mapping grid so as to avoid aliasing, as explained in the next subsection. While a precise value for this frequency is sometimes difficult to obtain, since it requires a detailed model of the field source, an estimate may provide enough information to achieve reliable deconvolutions. Because the spectrum of magnetic fields usually extends towards infinity, some criterion should be used to define a "maximum" frequency. We consider as maximum spatial frequencies the frequencies encompassing 99% of the total field energy. To calculate the maximum spatial frequencies, we first compute the total field energy

$$\mathcal{E} = \int_{-\infty}^{+\infty} \int_{-\infty}^{+\infty} |B_z(x, y, z)|^2 dx dy. \quad (10.77)$$

Then, for fields without circular symmetry, we suppose the maximum frequencies to be the same in both x and y directions, and use Parseval's theorem to obtain

- 7) At present, most biomagnetic SQUID systems are limited by the low-pass filtering of the Green's function, associated with the liftoff, and not by the coil size. However, for SQUID microscopes, apodized coils may provide much better sensitivity than bare SQUIDs and yet offer comparable spatial

resolution. In addition, apodized coils are flat, multiturn coils, thereby avoiding the strong blurring effect associated with the coil thickness of hand-wound coils in SQUID microscopes. Usually, coil thickness is much greater than liftoff in SQUID microscopes.

$$\int_0^{k_{\max}} \int_0^{k_{\max}} |b_z(k_x, k_y, z)|^2 dk_x dk_y = (1/4) \times 4\pi^2 \times 0.99 \times E. \quad (10.78)$$

However, for circularly symmetric fields we can obtain a one-dimensional relation by using the zeroth-order Hankel transform [72] (in this case, k_{\max} is the same in all directions)

$$\int_0^{k_{\max}} k_\rho |b_z(k_\rho, z)|^2 dk_\rho = 4\pi^2 \times 0.99 \times E, \quad (10.79)$$

where $k_\rho = (k_x^2 + k_y^2)^{1/2}$. Equations (10.78) and (10.79) can be numerically solved for k_{\max} .

As an example, consider a current dipole pointing in the x -direction. Then, we have that

$$B_z(x, y, z) = \frac{\mu_0 p_x}{4\pi} \left[\frac{y}{(x^2 + y^2 + z^2)^{3/2}} \right], \quad (10.80)$$

which has a two-dimensional Fourier transform given by

$$b_z(k_x, k_y, z) = \begin{cases} -i\mu_0 p_x \frac{k_y e^{-z\sqrt{k_x^2 + k_y^2}}}{2\sqrt{k_x^2 + k_y^2}} & \text{for } k_x \neq 0 \text{ and } k_y \neq 0. \\ 0 & \text{otherwise.} \end{cases} \quad (10.81)$$

Thus, the total field energy is related to the liftoff distance z by

$$\mathcal{E} = \frac{(\mu_0 p_x)^2}{64\pi z^2}. \quad (10.82)$$

For a magnetic dipole source pointing in the z -direction, the field exhibits circular symmetry

$$B_z(x, y, z) = \frac{\mu_0 m_z}{4\pi} \left[\frac{3z^2}{(x^2 + y^2 + z^2)^{5/2}} - \frac{1}{(x^2 + y^2 + z^2)^{3/2}} \right], \quad (10.83)$$

and the Fourier transform is

$$b_z(k_\rho, z) = \begin{cases} \mu_0 m_z \left[2\sqrt{2\pi} z^2 (k_\rho/z)^{3/2} K_{3/2}(z k_\rho) - (2\pi/z) e^{-z k_\rho} \right], & \text{for } k_\rho \neq 0 \\ 0 & \text{, otherwise,} \end{cases} \quad (10.84)$$

where $K_{3/2}(\cdot)$ is the modified Bessel function of order $3/2$. In this case, the total field energy is given by

$$\mathcal{E} = \frac{3(\mu_0 m_z)^2}{64\pi z^4}. \quad (10.85)$$

The plots of the maximum frequency against liftoff distance for the two dipolar sources are shown in Figure 10.16. We observe that the maximum frequency for a 5-mm liftoff, as used in the examples, ranges from 90 to 160 m^{-1} . Other field sources can be used to estimate more closely the maximum spatial frequencies, depending on the experiment in question.

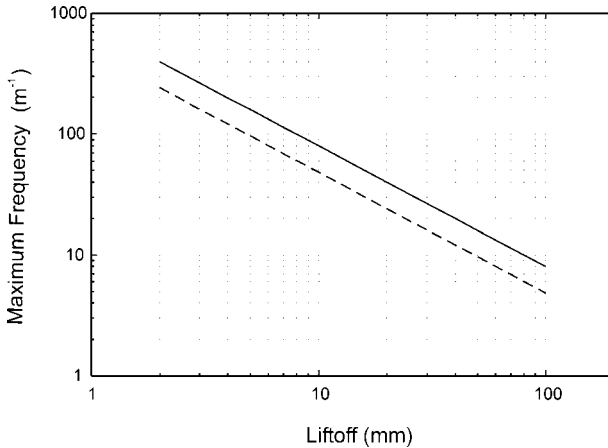


Fig. 10.16 Maximum spatial frequency of the magnetic field as a function of the liftoff for a current dipole (dashed line) on the xy -plane, and a magnetic dipole (solid line) pointing in the z -direction. (Adapted from Ref. [87], with permission.)

Sampling Frequency and Step Size

Before we can proceed further with our analysis of spatial filtering, we must clarify several important issues in spatial sampling, particularly in the context of a scanning magnetometer or a SQUID array used to record a time-varying field. It is important to consider the trade-offs between scanning velocity, SQUID separation, temporal sampling rate, integration time constant, temporal response, spatial resolution, and sensitivity [73]. We will analyze the more complex case of a scanned SQUID, but many of our observations apply to SQUID arrays as well.

The temporal sampling frequency used to construct a magnetic field map should satisfy the Nyquist theorem

$$f_s > 2f_{\max}, \quad (10.86)$$

where f_{\max} is the maximum temporal frequency present in the magnetic field signal. For time-varying fields, f_{\max} is determined either by the SQUID electronics filter cutoff frequency (for low signal-to-noise ratios) or by the field sources. For static fields, f_{\max} is related to the scanning speed and to the maximum spatial fre-

quency k_{\max} of the magnetic field. More accurately, f_{\max} depends on the maximum spatial frequency of the flux, since this is the quantity being sampled. However, because the flux is a low-pass or band-pass filtered version of the magnetic field, ensuring that the field is sampled without aliasing implies that the flux is also correctly sampled. If the scanning speed is ν and $s(k)$ is the spectrum of the magnetic field along a scan line in the x -direction, by using the transformation of variables $x = \nu t$ and the “time-scaling” property of Fourier transforms we obtain

$$s(k) = FT\{S(x)\} = FT\{S(\nu t)\} = \frac{1}{\nu} s\left(\frac{\omega}{\nu}\right) = \frac{1}{\nu} s\left(\frac{2\pi f}{\nu}\right). \quad (10.87)$$

Thus, the spatial and temporal frequencies are related by the following expression

$$k = \frac{2\pi f}{\nu}, \text{ or } f = \frac{k\nu}{2\pi}, \quad (10.88)$$

meaning that the faster the scan is performed, the higher the temporal frequencies that must be recorded, as expected. That also means, however, that one has to increase the bandwidth of the SQUID system, and that leads to increased noise. To avoid spatial aliasing, the temporal sampling frequency should satisfy

$$f_s > \frac{k_{\max}\nu}{\pi}. \quad (10.89)$$

The scanning step size Δ , or the reciprocal of the spatial sampling frequency, is also governed by the Nyquist theorem. The maximum step size (or SQUID separation in an array) that can be used without the occurrence of aliasing is given by

$$\Delta \leq \frac{\pi}{k_{\max}} \quad (10.90)$$

Inward Continuation

Because there is no unique solution to the three-dimensional magnetic inverse problem, most solutions to this inverse problem use heavily constrained models for the sources. Alternatively, if the sources are restricted to a well-defined, bounded volume, Laplace’s equation can be used to continue fields observed at some distance inward to the bounding surface, thereby sharpening or deblurring the field. The continuation can also be performed in the opposite direction: upward continuation transforms the magnetic field measured on one surface to the field that would be measured at another surface farther from the sources. As was discussed in Section 10.1, there is no need to sample the field over the entire volume above the source distribution. The best results, however, will be obtained if the magnetometer is placed as close as possible to the sources so as to minimize the noise-enhancing amplification of high spatial frequencies associated with inward continuation.

As discussed in more detail elsewhere [46–48, 74, 75], this approach can be used to convert, in a model-independent manner, a map of the magnetic field measured 10–20 mm from the surface of the scalp into a sharper map of the mag-

netic field on the surface of the cortex, without having to utilize any physical or physiological constraints. Inward continuation deeper into the cortex could be invalidated by active current sources near the cortical surface.

Both inward and upward continuations are unique. Upward continuation is a stable transformation, as it performs a low-pass attenuation on the original field, whereas inward (or downward) continuation tends to be unstable, because it consists of exponentially boosting high spatial frequencies. In the latter case, the stability of the calculation can be affected by measurement geometry, source configuration, and noise. While inward continuation has not been utilized heavily in biomagnetism, it is a common technique in geophysics to sharpen geomagnetic features deep beneath the soil surface. In the spatial frequency domain, the inward continuation of the field measured at z_1 to the point z_2 is [56]

$$b_z(k_x, k_y, z_2) = e^{(z_1 - z_2)\sqrt{k_x^2 + k_y^2}} b_z(k_x, k_y, z_1). \quad (10.91)$$

When z_2 is less than z_1 , the exponential term acts as a high-pass amplifier, amplifying the high-spatial-frequency components of the image. The advantage of this approach is that it allows sharpening of the image without a specific model for the source. In addition, it preserves the physical dimensions of the original data, unlike other derivative-based techniques used to enhance the spatial resolution of magnetic fields. Therefore, the same analysis tools used on the original data can also be applied to the transformed data. The disadvantages are that it works only between two values of z for which there are no current sources or magnetization, and that it is subject to instabilities due to excessive amplification of high-spatial-frequency noise.

Several techniques have been developed to overcome the instability problem, and the literature in geophysics is abundant in papers dealing with this subject. We just mention two of those techniques, which improve the quality of continued field maps. The integrated second vertical derivative (ISVD) method proposed by Fedi and Florio [76] combines frequency and spatial domain transformations to achieve better stability. The idea is to use a Taylor series expansion in z to continue the field, but to utilize frequency methods in the calculations of derivatives. The first vertical derivative is obtained by initially integrating the field along the z -direction, by means of a frequency-domain operator, and then by computing the second vertical derivative from the horizontal second derivatives, as given by Laplace's equation. All other high-order vertical derivatives can be obtained from Laplace's equation applied to either the field (even-order derivatives) or the first derivative (odd-order derivatives). Because the integration performed in the frequency domain is a stable operation and the second horizontal derivatives are approximated by finite differences, the Taylor series is fairly stable. However, the influence of the low-pass filtering associated with integration on the final spatial resolution of the continued field still has to be assessed.

Using a different approach based on Wiener filter theory, Pawlowski [77] proposed the preferential continuation method, which stabilizes the inward continua-

tion and allows for a discriminated processing of shallow and deep sources. In this method, a band-pass amplification is applied to the original field map, enhancing deep sources while keeping shallow sources (high spatial frequencies) unchanged. The overall effect for nonplanar source distributions is equivalent to “compressing” the map, with shallow and deep sources presenting similar sharpness. Even though this feature is useful in many applications, care should be taken when interpreting or further processing the continued fields. For planar sources, the resulting effect is a controlled increase in the sharpness, while avoiding excess of noise, but compromising spatial resolution.

It is worthwhile noticing that the exponential factor $e^{\pm z\sqrt{k_x^2+k_y^2}}$ associated with inward and upward continuations is already embedded in the expressions of the inverse problem in the spatial frequency domain (e.g., (10.73), (10.207) and (10.209)). Thus, when calculating the solution to the inverse problem by spatial frequency methods we are implicitly performing an inward continuation all the way down to the sources. Consequently, the inward continuation at a smaller lift-off is quite useful when an inverse solution with adequate resolution could not be obtained due to the need of severe regularization (i.e., low-pass filtering), or when just a sharper magnetic map is sufficient to provide the desired information.

To illustrate the capabilities of the method, we used one of the Vanderbilt SQUID microscope systems (monolithic SQUID with $40\ \mu\text{m} \times 40\ \mu\text{m}$ effective area) to scan a sample consisting of a piece of paper containing small symbols printed by two different printers. The original magnetic map is shown in Figure 10.17(a), while an inward continued map is shown in Figure 10.17(b). The

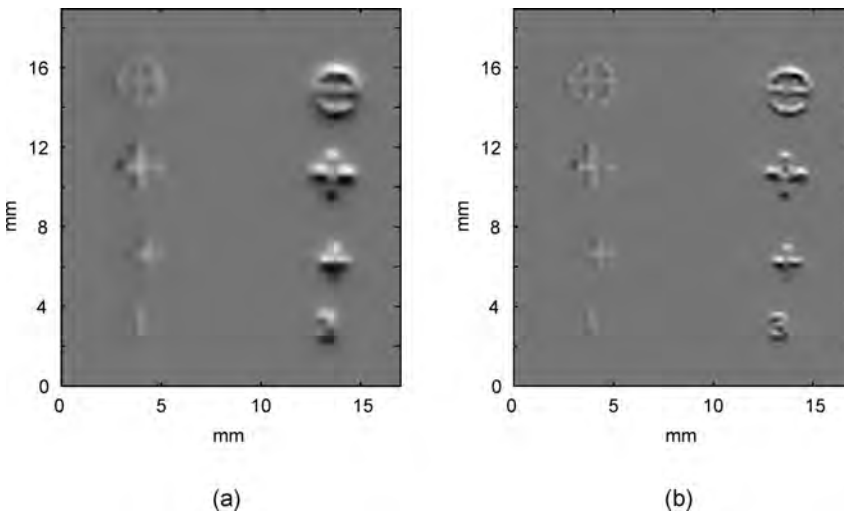


Fig. 10.17 Increasing the spatial resolution of a magnetic map by means of downward continuation techniques. (a) Original magnetic map of a pattern of small symbols printed on a sheet of paper, obtained with one of the

Vanderbilt SQUID microscopes; (b) magnetic map processed by a downward continuation technique. Notice the increase in spatial resolution (deblurring), particularly evident for the right-hand column of symbols.

deblurring effect of the inward continuation is readily apparent, corresponding to an increase in the spatial resolution, particularly for the top and bottom symbols in the right-hand column.

Imaging Discontinuous Currents

In the spatial frequency domain, the z component of the magnetic field from a current-carrying plate of thickness d is given by (10.73), which can be written in a more compact form as

$$b_z = \frac{i\mu_0 d}{2} \left(\frac{k_x}{k} j_y - \frac{k_y}{k} j_x \right) e^{-kz}, \quad z \gg d, \quad (10.92)$$

where

$$k = \sqrt{k_x^2 + k_y^2}. \quad (10.93)$$

Let us consider a measurement of the distortions of the magnetic field associated with discontinuities or heterogeneities in a planar sample, such as a high-temperature superconductor. If current is injected into a planar sample through vertical wires and bus structures on the edges, the current would be uniform were it not for the discontinuities. As shown in Figure 10.18, the magnetic field from the vertical wires is horizontal and does not contribute to the vertical magnetic field B_z . Were the sample homogenous and continuous, the current in the sheet would be uniform, and the magnetic field would be determined solely by the curl of the current associated with the current discontinuity at the edges. Similarly, if we did not choose to use the bus structures, we could include our knowledge of the location of the wires that inject the current by modifying the two-dimensional continuity condition ((10.75)) to include this information [78, 79] as follows:

$$\nabla \cdot \vec{J}(x, y) = F(x, y), \quad (10.94)$$

where $F(x, y)$ describes the current source and sink distribution in the sheet, *i.e.*, I_z in the wires as it enters the sheet. In the spatial frequency domain, our magnetic imaging problem becomes

$$ik_x j_x + ik_y j_y = f(k_x, k_y). \quad (10.95)$$

We then obtain

$$J_x = FT^{-1}\{j_x\} \quad (10.96)$$

$$= FT^{-1}\left\{i \frac{2k_y}{\mu_0 k d} e^{kz} b_z - i \frac{k_x f}{k^2}\right\}, \quad (10.97)$$

and

$$J_y = FT^{-1} \left\{ j_y \right\} \quad (10.98)$$

$$= FT^{-1} \left\{ -i \frac{2k_x}{\mu_0 k d} e^{kz} b_z - i \frac{k_y f}{k^2} \right\}. \quad (10.99)$$

These equations break down for $k = 0$; one cannot recover uniform components of current distributions. This corresponds to an infinite sheet of uniform current producing no perpendicular magnetic field, *i.e.*, with the two edges infinitely far away and the magnetic field being parallel to the sheet.

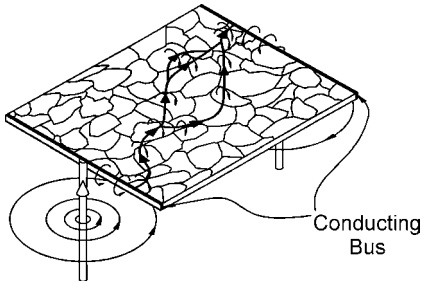


Fig. 10.18 Current injection into a granular substrate. (Adapted from Ref. [9], with permission.)

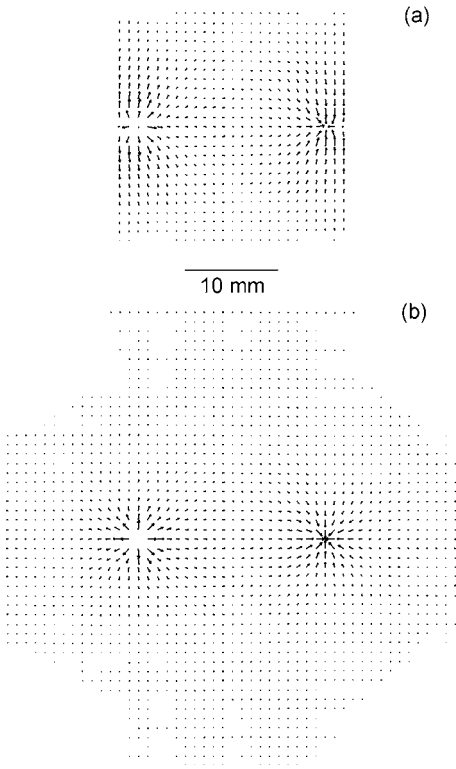


Fig. 10.19 The results of using an unconstrained filtering technique to solve a bounded current source: (a) the original current distribution; (b) the reconstruction using inverse spatial filtering. (Adapted from Ref. [79], with permission.)

Figure 10.19 shows a comparison of the original current distribution and the distribution reconstructed by this approach. Note that the source and the image are in good agreement in the immediate vicinity of the current-injection electrodes. As we shall see later, the inability of the spatial filtering technique to constrain currents to flow within known boundaries limits this technique to situations where the magnetometer is very close to the current distribution.

Planar Current-Injection Tomography

We can extend this approach and use magnetic imaging and the Fourier transform/spatial filtering approach to determine the conductivity distribution within a planar conducting object [60]. We start with Ohm's law, which gives us the current density $\vec{J}(\vec{r})$ in an inhomogeneous, isotropic conductor with conductivity distribution $\sigma(\vec{r})$,

$$\vec{J}(\vec{r}) = \sigma(\vec{r})\vec{E}(\vec{r}). \quad (10.100)$$

As we saw in (10.15), the curl of the current density can be thought of as the "source" of the magnetic field. In inhomogeneous conductors, $\nabla \times \vec{J}$ has two contributions: one from spatial variations, $\nabla\sigma$, and another from EMFs, $\nabla \times \vec{E}$,

$$\nabla \times \vec{J} = \nabla\sigma \times \vec{E} + \sigma\nabla \times \vec{E}. \quad (10.101)$$

A boundary between conducting and insulating regions is simply a sudden spatial variation in σ , at which the discontinuity in the tangential current produces a magnetic field. In the quasistatic limit with no sources of EMF within the conductor, *i.e.*, with currents injected and removed only on the surface of the object, the curl of \vec{E} must be zero, since it is derivable from a scalar potential. In this case, $\nabla \times \vec{J}$ becomes

$$\nabla \times \vec{J}(\vec{r}) = \frac{\nabla\sigma(\vec{r})}{\sigma}(\vec{r}) \times \vec{J}(\vec{r}), \quad (10.102)$$

which can be written as

$$\nabla \times \vec{J}(\vec{r}) = (\nabla \ln \sigma(\vec{r})) \times \vec{J}(\vec{r}). \quad (10.103)$$

As pointed out by Staton [60], the strategy of conductivity imaging via current-injection tomography is to reconstruct $\sigma(\vec{r})$ from a known $\vec{J}(\vec{r})$ using (10.103). However, it is not possible to reconstruct the conductivity distribution using a single distribution of injected current. One problem with a single configuration of injected current is that it is possible to have a nonzero $\nabla \ln \sigma$ and nonzero \vec{J} , but have zero $\nabla \times \vec{J}$. This occurs if both $\nabla \ln \sigma$ and \vec{J} are parallel, for example in a rectangular conducting bar in which the conductivity varies only in one direction, but the current flows uniformly in the bar along that direction. In this case, the currents do not indicate the presence of gradients in the conductivity distribution, and the current distribution could be the result of uniform current injection into

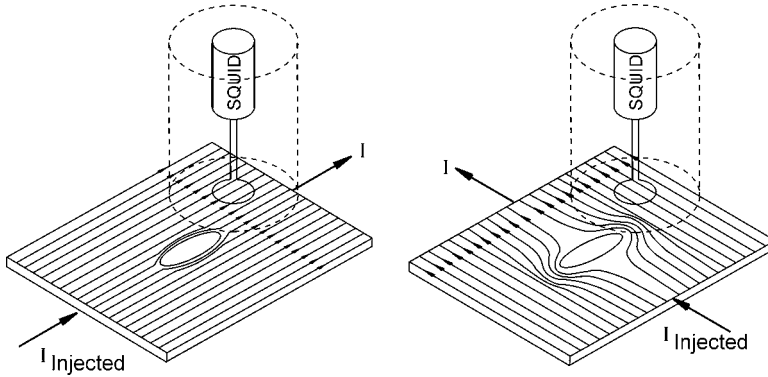


Fig. 10.20 Current-injection tomography in a thin, conducting plate. (Adapted from Ref. [60], with permission.)

an isotropic homogeneous bar. It is thus important that tomography be employed by injecting current into the sample from multiple directions, with magnetic imaging of the current distribution for each configuration of current injection. At the very least, current should be injected in orthogonal directions: two directions for a thin conducting plate and three directions for a rectangular conducting slab, as illustrated in Figure 10.20. When current is injected (left) along the major axis of an elliptical flaw (x direction), the current is perturbed less than when injected (right) orthogonally along the minor axis (y direction). The combined magnetic imaging of both current distributions contains information on the length and width of the flaw.

As should be familiar by now, if the current density \vec{J} were known everywhere in a three-dimensional conducting sample, then it would in principle be possible to solve (10.102). However, there is no unique solution to the general three-dimensional magnetic inverse problem for currents, and hence determination of a three-dimensional conductivity distribution from magnetic measurements alone will, in general, be impossible. However, the two-dimensional current inverse problem does have a unique solution [56], and we can use current tomography with magnetic measurements of $J(\vec{r})$ to determine the conductivity distribution in a planar sample.

To illustrate this approach, let us examine the minimal case of using only two orthogonal distributions of injected current for a planar sample. We can use magnetometer and spatial filtering inverse techniques described previously to obtain images of the two resulting current distributions

$$\vec{J}_1(x, y) = J_{1x}(x, y)\hat{x} + J_{1y}(x, y)\hat{y}, \quad (10.104)$$

$$\vec{J}_2(x, y) = J_{2x}(x, y)\hat{x} + J_{2y}(x, y)\hat{y}. \quad (10.105)$$

For our two-dimensional case, the normal component of the curl of each current-density distribution obeys (10.103), which becomes

$$\begin{aligned}\nabla \times \vec{J}_1(x, y) \cdot \hat{n} &= J_{1y} \left(\frac{\partial \ln \sigma(x, y)}{\partial x} \right) - J_{1x} \left(\frac{\partial \ln \sigma(x, y)}{\partial y} \right) \\ &\equiv c_1(x, y),\end{aligned}\tag{10.106}$$

$$\begin{aligned}\nabla \times \vec{J}_2(x, y) \cdot \hat{n} &= J_{2y} \left(\frac{\partial \ln \sigma(x, y)}{\partial x} \right) - J_{2x} \left(\frac{\partial \ln \sigma(x, y)}{\partial y} \right) \\ &\equiv c_2(x, y).\end{aligned}\tag{10.107}$$

The unknown quantities in this pair of equations are $\partial \ln \sigma(x, y) / \partial x$ and $\partial \ln \sigma(x, y) / \partial y$. In tomography, with a large number of directions of injected current, there will be a highly overdetermined set of equations for these two unknown distributions that would be solved numerically. In our simple two-current example, we can reduce the pair of equations into a more tractable form analytically

$$\frac{\partial \ln \sigma(x, y)}{\partial x} = (J_{x1}c_2 - J_{x2}c_1) / (J_{x1}J_{y2} - J_{x2}J_{y1}) \equiv f_x(x, y),\tag{10.108}$$

and

$$\frac{\partial \ln \sigma(x, y)}{\partial y} = (J_{y1}c_2 - J_{y2}c_1) / (J_{x1}J_{y2} - J_{x2}J_{y1}) \equiv f_y(x, y).\tag{10.109}$$

To obtain the conductivity distribution, we simply numerically integrate each of these equations

$$\ln \sigma(x, y) = \ln \sigma(x_0, y_0) + \int_{x_0}^x f_x(x', y) dx' + \int_{y_0}^y f_y(x_0, y') dy'.\tag{10.110}$$

The conductivity distribution is thus

$$\sigma(x, y) = \sigma(x_0, y_0) e^{\left(\int_{x_0}^x f_x(x', y) dx' + \int_{y_0}^y f_y(x_0, y') dy' \right)}.\tag{10.111}$$

Note that in the integration, we include explicitly as a constant of integration the conductivity $\sigma(x_0, y_0)$ at the single point where we began the integration. If that conductivity is not known, we can determine only normalized conductivity $\sigma(x, y) / \sigma(x_0, y_0)$. Alternatively, if we measure the resistance between the current injection electrodes, we should be able to obtain a value for $\sigma(x_0, y_0)$. Figure 10.21

shows the results of a numerical simulation of this process for an elliptically shaped, Gaussian flaw in a copper plate, given by

$$\sigma(x, y) = \sigma_0 \left(1 - 0.8 e^{-\frac{1}{2} \left[\left(\frac{x}{a} \right)^2 + \left(\frac{y}{b} \right)^2 \right]} \right) \quad (10.112)$$

where $\sigma_0 = 5.8 \times 10^7$ S/m, $a = 5$ mm, and $b = 2$ mm. The thin, conducting plate is of length $l = 0.1$ m, width $w = 0.1$ m, and thickness $100 \mu\text{m}$. For the simulation, a total of 10 mA of current was injected uniformly into the plate along the major axis of the elliptical flaw (x -direction), and also in a separate current injection along the minor axis of the elliptical flaw (y -direction) as illustrated in Figure 10.21. The forward problem consisted of calculating the electrical potentials, current densities, curl of the current densities, and magnetic fields. The inverse problem consisted of reconstructing the conductivity distribution from the magnetic fields. As discussed in more detail by Staton [60] the accuracy of this method is determined by the ability to image current densities and curl distributions from the magnetic fields. The error in the inverse procedure depends on a variety of factors: the distance between the current distribution and detector, the signal-to-noise ratio of the measurement, the distance between magnetic measurements, and the spatial extent of the measurement. This calculation demonstrates the fea-

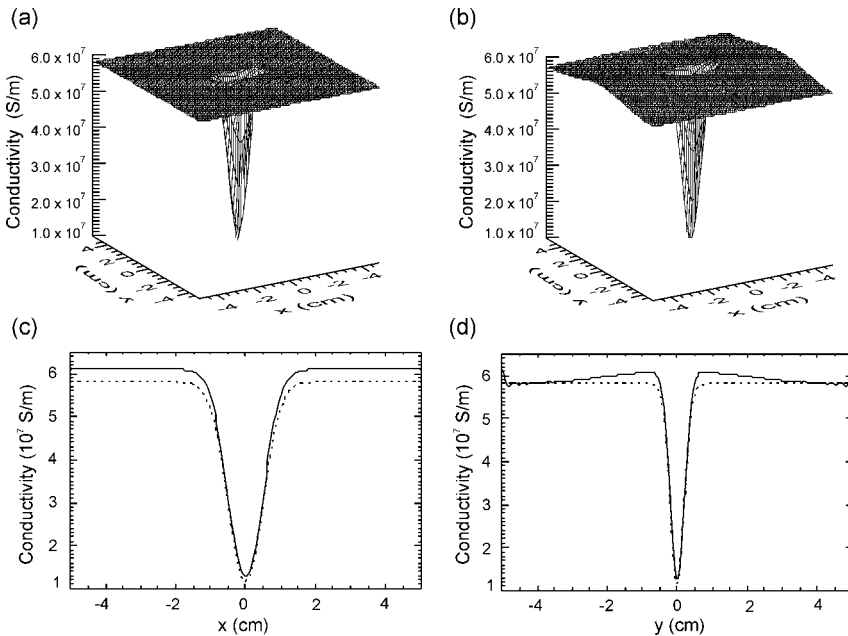


Fig. 10.21 A comparison of (a) original conductivity distribution and (b) magnetically reconstructed solution using current-injection tomography, and cross-section comparison of original conductivity distribution (dotted line)

and reconstructed solution (solid line) along the (c) major axis and (d) minor axis of the elliptically shaped, Gaussian flaw. (Adapted from Ref. [60], with permission.)

sibility of the technique; further studies will require adding noise and varying the sampling parameters, and should also address the possible advantages of applying current to the sample from multiple directions (more than the minimally required number of two or three).

The Hosaka-Cohen Transformation

A “current pattern” in the xy -plane can be obtained from B_z by the Hosaka-Cohen (HC) transformation [80]

$$HC \equiv \frac{\partial B_z}{\partial y} \hat{x} - \frac{\partial B_z}{\partial x} \hat{y}, \quad (10.113)$$

where the field is measured a distance z above the currents. The components of HC resemble the currents, *i.e.*,

$$J_x \propto \frac{\partial B_z}{\partial y} \equiv HC_x \quad (10.114)$$

$$J_y \propto \frac{\partial B_z}{\partial x} \equiv HC_y. \quad (10.115)$$

The HC transformation is believed valid for two-dimensional current distributions, but has been applied to data from three-dimensional sources [80, 81]. The uncertainty lies with the derivation of the HC transformation, which is based upon the curl of \vec{B} . Ampère’s law states that

$$\begin{aligned} \vec{J} &= \frac{1}{\mu_0} \nabla \times \vec{B} \\ &= \frac{1}{\mu_0} \left\{ \left(\frac{\partial B_z}{\partial y} - \frac{\partial B_y}{\partial z} \right) \hat{x} - \left(\frac{\partial B_z}{\partial x} - \frac{\partial B_x}{\partial z} \right) \hat{y} + \left(\frac{\partial B_y}{\partial x} - \frac{\partial B_x}{\partial y} \right) \hat{z} \right\}. \end{aligned} \quad (10.116)$$

Within a current distribution of infinite extent with no z -dependence,

$$\frac{\partial B_y}{\partial z} \simeq \frac{\partial B_x}{\partial z} \simeq 0. \quad (10.117)$$

If we add the tighter constraint that $J_z = 0$ everywhere, then

$$\vec{J} \simeq \frac{1}{\mu_0} \left\{ \frac{\partial B_z}{\partial y} \hat{x} - \frac{\partial B_z}{\partial x} \hat{y} \right\}. \quad (10.118)$$

Within a constant, this is the same as (10.113). However, this equation, as derived, applies only within the conductor, since outside a conductor both \vec{J} and $\nabla \times \vec{B}$ are everywhere zero in the quasistatic limit. In practice, one cannot readily measure \vec{B} inside a conductor. However, the symmetry for a two-dimensional planar current distribution is the same as for a three-dimensional current distribution with no J_z

and no z -dependence of either J_x or J_y . The validity of the HC transformation is unclear when it is possible only to measure \vec{B} at height z above the xy -plane.

We can shed some light on the meaning of the HC transformation by using Fourier spatial filtering [78]. In the spatial-frequency domain, we had the exact inverse solution for two-dimensional current distributions

$$j_x(k_x, k_y) = i \frac{2}{\mu_0 d} \frac{k_y}{\sqrt{k_x^2 + k_y^2}} e^{z\sqrt{k_x^2 + k_y^2}} b_z(k_x, k_y) \quad (10.119)$$

$$j_y(k_x, k_y) = -i \frac{2}{\mu_0 d} \frac{k_x}{\sqrt{k_x^2 + k_y^2}} e^{z\sqrt{k_x^2 + k_y^2}} b_z(k_x, k_y). \quad (10.120)$$

This can be expanded in a Taylor series

$$j_x(k_x, k_y) = i \frac{2}{\mu_0 d} \frac{k_y b_z(k_x, k_y)}{k} \left(1 + kz + \frac{1}{2!} k^2 z^2 + \dots \right), \quad (10.121)$$

where

$$k = \sqrt{k_x^2 + k_y^2}. \quad (10.122)$$

If k and z are sufficiently small, then

$$j_x(k_x, k_y) \approx i \frac{2}{\mu_0 d} k_y b_z(k_x, k_y) f, \quad (10.123)$$

where

$$f = 1/k + z + kz^2/2. \quad (10.124)$$

Similarly,

$$j_y(k_x, k_y) \approx -i \left(\frac{2}{\mu_0 d} \right) k_x b_z(k_x, k_y) f. \quad (10.125)$$

For comparison, the two-dimensional Fourier transform of HC is

$$j_x(k_x, k_y) \propto ik_y b_z(k_x, k_y) \quad (10.126)$$

$$j_y(k_x, k_y) \propto -ik_x b_z(k_x, k_y). \quad (10.127)$$

By fitting a straight line to the exact expression, we obtain [78]

$$j_x \approx i \frac{2\pi z}{\mu_0 d} k_y b_z(k_x, k_y) \quad (10.128)$$

$$j_y \approx -i \frac{2\pi z}{\mu_0 d} k_x b_z(k_x, k_y). \quad (10.129)$$

By taking the inverse Fourier transform, we can find the relation between the current density and the field gradients

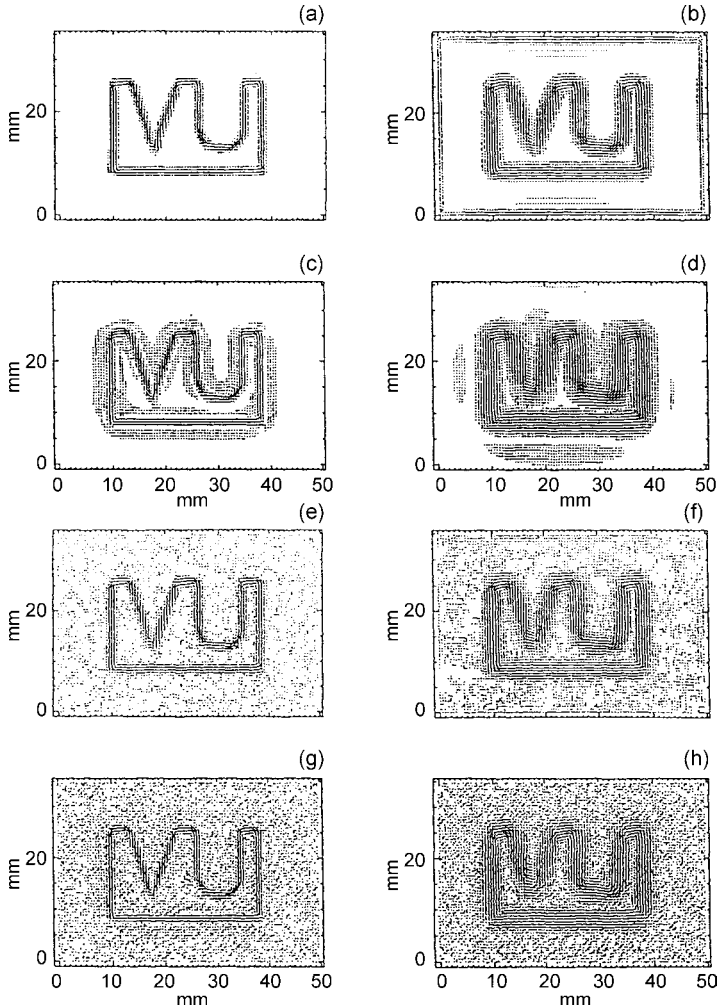


Fig. 10.22 A comparison of the exact and HC reconstructions for a “VU” current source similar to that in Fig. 10.11. Left: $z = 1.5$ mm; right: $z = 3.0$ mm. (a,b,c,d) No noise; (e,f,g,h) SNR = 10. (a,b,e,f) Exact reconstruction; (c,d,g,h) HC reconstruction. (Adapted from Ref. [78], with permission.)

$$J_x \approx \frac{2\pi z}{\mu_0 d} \frac{\partial B_z}{\partial y} \quad (10.130)$$

$$J_y \approx -\frac{2\pi z}{\mu_0 d} \frac{\partial B_z}{\partial x}, \quad (10.131)$$

and we see that the HC transformation is the first-order approximation to the exact inverse result. The approximation is best for small z and k . Figure 10.22 compares the results of the HC transformation and the exact result for data similar to those in Figure 10.12.

Alternating Projections to Enhance High-Frequency Information

A variety of general-purpose techniques common to image processing can be used to enhance the magnetic images obtained with scanning magnetometers. Examples include high- and low-pass spatial filtering [82], and background subtraction using polynomial fits. Alternating projections is a useful iterative technique to apply either constraints or *a priori* knowledge about the source [83]. As an example of this approach, suppose that we have an unknown current distribution, $\vec{J}^u(x, y)$, that corresponds to a wire of unknown shape. This current produces a magnetic field $B_z(x, y)$ by a known Green's function $G(x - x', y - y')$. In the spatial frequency domain, we have that

$$b_z(k_x, k_y) = FT\{B_z(x, y)\} \quad (10.132)$$

$$g(k_x, k_y) = FT\{G(x - x', y - y')\}. \quad (10.133)$$

The inverse problem is simply

$$j_x(k_x, k_y) = \frac{b_z(k_x, k_y)}{g(k_x, k_y)}. \quad (10.134)$$

However, as we discussed before, this results in numerical instabilities when $g(k_x, k_y)$ is small at large k . We avoid this problem by low-pass filtering the inverse process to obtain an approximate current image $\hat{j}_x(k_x, k_y)$, where

$$\hat{j}_x(k_x, k_y) = LPF \left\{ \frac{b_z(k_x, k_y)}{g(k_x, k_y)} \right\} \quad (10.135)$$

with the low-pass filter function $LPF = 0$ when $k_{LPF} < \sqrt{k_x^2 + k_y^2} < \infty$, and $LPF = 1$ otherwise. However, a spatial low-pass filter blurs the image and reduces the spatial resolution. The challenge is to return as much of the high-frequency information as possible while avoiding the instabilities that plague the Fourier inverse

approach. Because we know that the current is contained in a wire, we can sharpen the image by assuming that signals below a certain amplitude in the spatial domain are noise and eliminate them by a thresholding operation. We then use the added high-frequency information in the spatial-frequency domain to replace the high-frequency information that was lost in the low-pass filtering operation. Iteration between the spatial and spatial-frequency domains is why this approach is termed alternating projections.

We prepare for the iteration by assuming that our zeroth current distribution is the one that was obtained by the low-pass filtered Fourier inverse

$$j_x^0(k_x, k_y) = \hat{j}_x(k_x, k_y). \quad (10.136)$$

We select a threshold T and let $n = 1$. As step 1, we compute

$$J_x^n(x, y) = FT^{-1} \left\{ j_x^{n-1}(k_x, k_y) \right\}. \quad (10.137)$$

Step 2 is to form the thresholded image $\tilde{J}_x^n(x, y)$ by setting to zero all the values of $J_x^n(x, y)$ whose amplitudes are less than T , which sharpens the current distribution and adds high-frequency information. Step 3 converts this image into the spatial-frequency domain,

$$j_x^n(k_x, k_y) = FT \left\{ \tilde{J}_x^n(x, y) \right\}. \quad (10.138)$$

The difficulty is that the low-frequency information in this image is not as accurate as that in the original $\hat{j}_x(k_x, k_y)$. We correct for this with step 4: we substitute the more accurate $\hat{j}_x(k_x, k_y)$ for the less accurate $\hat{j}_x^n(k_x, k_y)$ in the region $0 < \sqrt{k_x^2 + k_y^2} < k_{LPF}$. We keep the sharpened $\hat{j}_x^n(k_x, k_y)$ in the region $\sqrt{k_x^2 + k_y^2} > k_{LPF}$. Finally, we decide whether or not to terminate the iteration, and if not, we let $n \leftarrow n + 1$ and return to step 1. The results of this process are shown in Figure 10.23. This is but one example of alternating projections. The technique can be further improved by adding a current-continuity constraint as a third projection [84]. Other criteria can be used to sharpen or modify the image, such as the selective enhancement of line-like structures in the image [83]. As with other sharpening algorithms, it is important to realize that the alternating projection approach does not reconstruct the original current distribution in a quantitative manner as do the other techniques we have reviewed, but instead processes the observed field pattern in a manner that can make it resemble more closely the original currents, with no guarantee of quantitative accuracy.

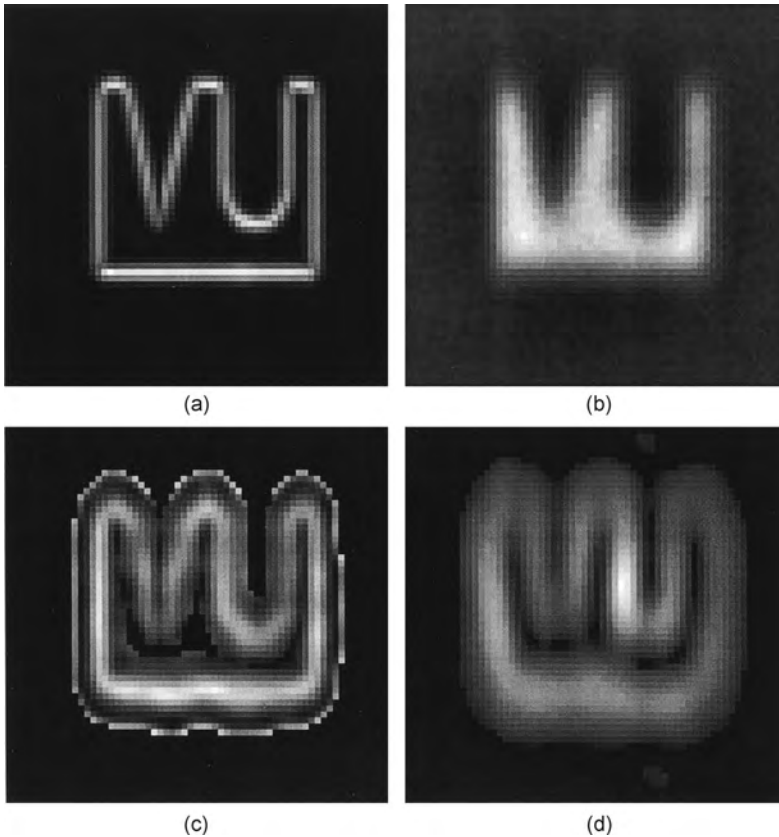


Fig. 10.23 Alternating projection enhancement of magnetic field maps: (a) the original current image; (b) the magnetic field at 1.5 mm with noise; (c) the recovered image after the first iteration; (d) after ten iterations. (Adapted from Ref. [84], with permission.)

Flux-Field Deconvolution

When inverting experimental data, often one cannot neglect the effects of the field integration over SQUID pickup and compensation coils. Since SQUID sensors detect magnetic flux and not magnetic field directly, the approximation $\Phi = \vec{B} \cdot \vec{A}$ is only valid if the field is uniform or the sources of the magnetic field are located far away from the coils, so that \vec{B} can be considered constant within the integration area. In many situations, especially with planar gradiometers, this is a coarse approximation and it can lead to substantial error in the solution of the inverse problem. In order to avoid this issue, we can try to incorporate sensor modeling into the formulation of the inverse problem. Unfortunately, for some common coil layouts this results in cumbersome calculations that frequently do not have a closed-form solution.

In cases where the magnetic field mapping area is not very restricted, it is possible to use spatial filtering tools to formulate the flux integral as a convolution and undo the integration by means of a deconvolution. By extending the approach used to analyze and design apodized coils, we can obtain models associated with different SQUID magnetometer and gradiometer designs. In addition to allowing for the recovery of magnetic field maps from magnetic flux measurements, such models can be a valuable aid in tailoring the geometry and arrangement of coils so as to optimize the SQUID performance for particular applications. Furthermore, spatial filtering models make it possible to effectively compare a multitude of magnetometer and gradiometer designs independent of any particular magnetic field source distribution, by using a common mathematical framework [85–89].

To demonstrate the relevance of modeling field integration in SQUID sensors, compare Figures 10.24(a) and (b). Figure 10.24(a) shows the simulated vertical component of the magnetic field produced by a single current dipole placed on the xy plane, at a 5-mm lift-off. Figure 10.24(b) shows the map that is obtained if a first-order planar gradiometer with square coils is used to scan the field. It is clear that both graphs bear little resemblance to one another and one cannot expect to obtain consistent solutions to inverse problems by disregarding such transformations to the magnetic field.

We begin by analyzing planar gradiometer designs and then extend the formulation to include axial gradiometers. We will not discuss magnetometer designs in this subsection, as they can be considered a special case of a planar gradiometer, and also to avoid repeating information presented in previous sections. However, we highlight that the formalism presented herein can be directly applied to magnetometers, since gradiometers are intrinsically more complex. Part of this section draws extensively from Ref. [87].

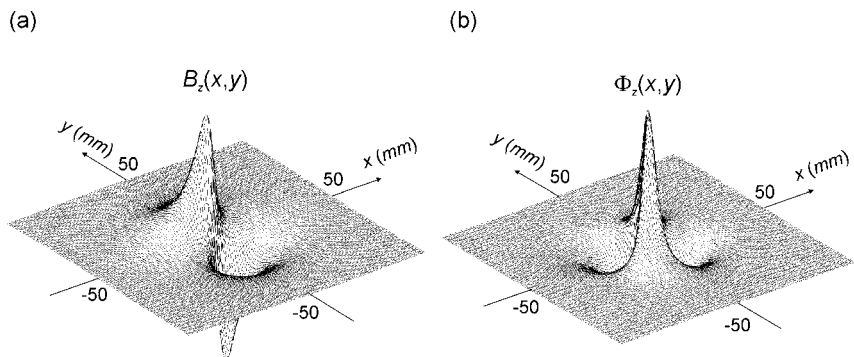


Fig. 10.24 Differences between the magnetic field map associated with a current dipole and the corresponding magnetic flux map obtained with a planar SQUID gradiometer: (a) vertical (z) component of the magnetic field generated by a current dipole located on

the xy -plane, at a 5-mm lift-off; (b) net magnetic flux through a first-order planar gradiometer with 5-mm square coils and 5-mm baseline in the x -direction. (Adapted from Ref. [87], with permission.)

Planar Gradiometers. The key idea behind modeling gradiometers through the use of frequency methods is the manipulation of the magnetic flux definition, so as to express the net flux through the gradiometer as the two-dimensional convolution of the magnetic field with a stepwise function F_G (the planar gradiometer is assumed to be parallel to the xy -plane)

$$\begin{aligned}\Phi(x, y, z) &= \iint_S \vec{B} \cdot \hat{n} \, da = \int_{-\infty}^{+\infty} \int_{-\infty}^{+\infty} B_z(x', y', z) F_G(x - x', y - y') \, dx' dy' \\ &= F_G(x, y) * B_z(x, y, z).\end{aligned}\quad (10.139)$$

This stepwise function accounts for the region of integration S , which in turn is related to the geometrical characteristics of the gradiometer. The function F_G is defined for an arbitrary point on the gradiometer plane as the number of turns of the coils enclosing the point, taking into account the winding direction.

The deconvolution operation aims to invert (10.139), thereby obtaining the magnetic field B_z associated with a known net flux through a specific gradiometer. Taking the two-dimensional Fourier transform on (10.139) and using the convolution property, we obtain

$$\varphi(k_x, k_y, z) = f_G(k_x, k_y) b_z(k_x, k_y, z).\quad (10.140)$$

Hence, gradiometers can be characterized in the frequency domain by a function f_G known as the spatial frequency response. In order to obtain the recovered field \tilde{B}_z , we first divide the Fourier transform of the flux by the frequency response, and then take the inverse Fourier transform:

$$\tilde{B}_z(x, y, z) = FT^{-1} \left[\frac{\varphi(k_x, k_y, z)}{f_G(k_x, k_y)} \right] = FT^{-1} \left[f_G^1(k_x, k_y) \varphi(k_x, k_y, z) \right],\quad (10.141)$$

where $f_G^1 = 1/f_G$ is the inverse spatial filter.

As an example, consider a first-order planar gradiometer with baseline d in the x -direction, comprised of two identical N -turn square coils with sides of length L wound in opposite directions. The stepwise function, also known as the turns function, is given by

$$F_G(x, y) = \begin{cases} N, & |x - d/2| \leq L/2 \text{ and } |y| \leq L/2 \\ -N, & |x + d/2| \leq L/2 \text{ and } |y| \leq L/2 \\ 0, & \text{otherwise,} \end{cases}\quad (10.142)$$

and the gradiometer frequency response is

$$f_G(k_x, k_y) = -2iL^2 N \sin(k_x d/2) \operatorname{sinc}\left(\frac{k_x L}{2\pi}\right) \operatorname{sinc}\left(\frac{k_y L}{2\pi}\right),\quad (10.143)$$

where $\text{sinc}(u) = \sin(\pi u)/\pi u$. Figure 10.25(a) shows the graph of the magnitude of the frequency response for $L = 5$ mm, $d = 5$ mm, and $N = 1$.

Several characteristics can be observed from both the graph and (10.143). First, this gradiometer configuration lacks circular symmetry, which means that the gradiometer effects are not the same along different directions. Therefore, direct interpretation of maps can be difficult if the source arrangement is not known *a priori*: if the sample is scanned with the sensor oriented in different ways, different maps will be obtained. Moreover, (10.143) is separable, which means that the effects in the x and y directions are independent.

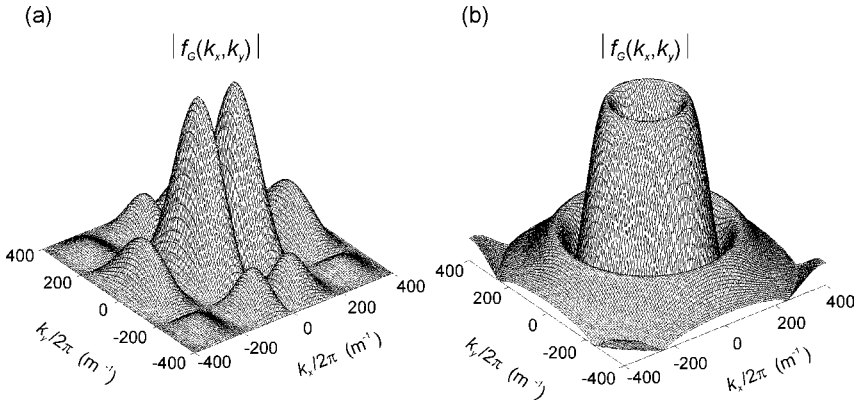


Fig. 10.25 Magnitude of the normalized gradiometer spatial frequency response: (a) first-order planar gradiometer comprised of two 5-mm single-turn square coils and 5-mm baseline in the x direction; (b) first-order

concentric planar gradiometer made up of a four-turn 2.5-mm radius circular coil and a single-turn 5-mm radius circular coil. (Adapted from Ref. [87], with permission.)

Second, there exists a line of zeros $k_x = 0$ through the origin of the spatial frequency plane which is associated with the sine term in (10.143). As discussed in previous sections, a zero in the frequency domain corresponds to permanent loss of information. Because gradiometers are intended to selectively reject some information, such as uniform fields, inevitably zeros will appear in the frequency response. A rejection of uniform fields is equivalent to a zero at the origin of the frequency plane $k_x = k_y = 0$, and therefore the mean value of the field cannot be recovered by the deconvolution procedure. However, the line of zeros $k_x = 0$ intrinsic to this configuration (note that changing L or d will produce no change on that line) corresponds to a rejection of any field that is constant in the x direction but not necessarily in the y direction. Although this can be useful in some specific applications [86], it leads to severe distortions in the recovered field. Figure 10.26(a) shows the magnetic field recovered from the flux depicted in Figure 10.24(b).

Third, the baseline introduces lines of zeros $k_x = \pm 2\pi(n-1)/d$, for $n = 1, 2, \dots$, whereas the coil introduces lines of zeros $k_x = \pm 2\pi m/L$ and $k_y = \pm 2\pi m/L$, for $m = 1, 2, \dots$. If $L = d$, as in our example design, then the lines of zeros associated

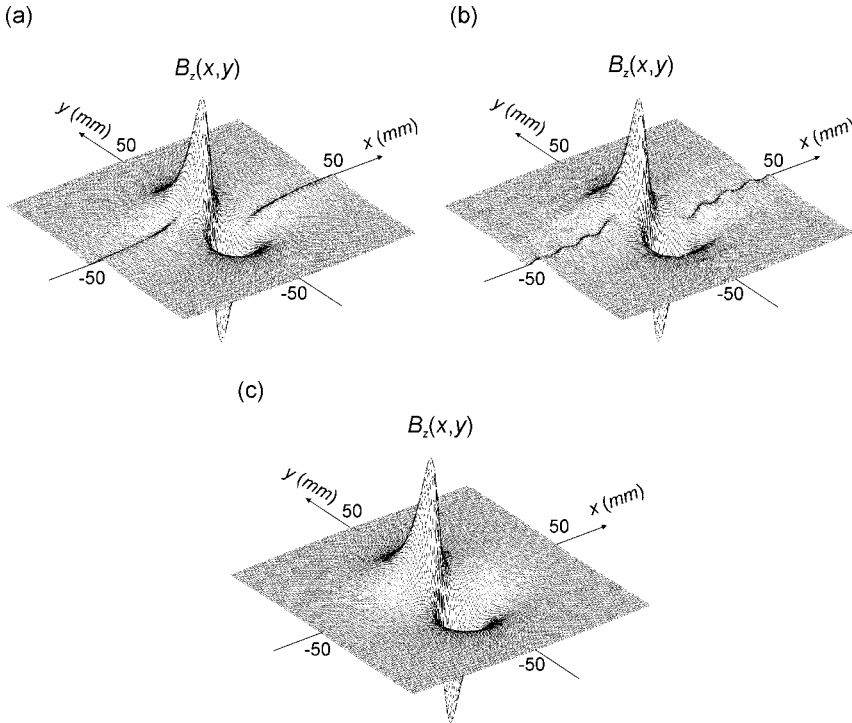


Fig. 10.26 Magnetic field maps recovered by the flux-field deconvolution for different gradiometer designs: (a) first-order gradiometer comprised of 5-mm single-turn square coils and 5-mm baseline in the x direction; (b) same as (a) except for 10-mm coils and

10-mm baseline; (c) first-order concentric planar gradiometer made up of a four-turn 2.5-mm radius circular coil and a single-turn 5-mm radius circular coil. (Adapted from Ref. [87], with permission.)

with the baseline (for $n \geq 2$) coincide with the lines of zeros in the same direction which are related to the coil geometry. If the source distribution generates a magnetic field with information at higher spatial frequencies, reaching those other lines of zeros, then additional information is lost and more distortion is introduced in the recovered field. Figure 10.26(b) shows the recovered field obtained from the same flux map, but with a gradiometer with $L = d = 10$ mm. (Note that increasing L or d results in moving the lines of zeros closer to the origin.)

It is worthwhile observing that other configurations of planar gradiometers have better spatial frequency characteristics and do not suffer from some of the pathologies described above. For instance, Figure 10.26(c) shows the recovered field obtained using a concentric planar design with circular coils (four-turn 5-mm radius coil surrounded by a single-turn 10-mm coil). It can be seen that an excellent recovery of the magnetic field could be obtained in this case. For this configuration, we have

$$F_G(x, y) = \begin{cases} N_1 - N_2, & \sqrt{x^2 + y^2} \leq a_1 \\ -N_2, & a_1 < \sqrt{x^2 + y^2} \leq a_2 \\ 0, & \text{otherwise,} \end{cases} \quad (10.144)$$

and

$$f_G(k_x, k_y) = \frac{2\pi N_1 a_1}{\sqrt{k_x^2 + k_y^2}} \left[J_1\left(a_1 \sqrt{k_x^2 + k_y^2}\right) - J_1\left(a \cdot a_1 \sqrt{k_x^2 + k_y^2}\right) / a \right], \quad (10.145)$$

where the condition $N_1 / N_2 = (a_2 / a_1)^2$ must be satisfied to reject uniform fields, $J_1(\cdot)$ is the Bessel function of first kind and first order, and $a = a_2 / a_1$. Observe that the frequency response is circularly symmetrical, as it depends on $\sqrt{k_x^2 + k_y^2}$ only, as shown in Figure 10.25(b). There is a zero at the origin, with the subsequent zeros appearing at circles around the origin of the spatial frequency plane.

Differently from the inverse problem, we always have to handle zeros in the division operation in (10.141), because gradiometers have at least one zero at the origin of the frequency plane. If noise is present in the flux map at moderate to high levels, improper handling of the zeros in the gradiometer frequency response can lead to noisy recovered fields. To address this issue by reducing the sensitivity of the inverse filter to noise and assigning to the inverse filter frequency response a defined value at the zeros of the gradiometer frequency response, we use a pseudoinverse filter defined as follows:

$$f_G^1(k_x, k_y) = \begin{cases} \frac{1}{f_G(k_x, k_y)}, & \text{if } |f_G(k_x, k_y)| > \gamma \\ \frac{1}{\gamma} \frac{|f_G(k_x, k_y)|}{f_G(k_x, k_y)}, & \text{otherwise,} \end{cases} \quad (10.146)$$

where γ is an adjustable threshold value. Equation (10.146) shows that the pseudoinverse filter limits $|1/f_G|$ to a maximum value of $1/\gamma$, while preserving the phase information. If the threshold is too small then the recovered field can be noisy, whereas making it too big can lead to loss of information on large regions of the frequency plane around the zeros.

However, even with the pseudoinverse approach, the recovered field may still be noisy due to the amplification of the noise component by a factor of $1/\gamma$ near the lines or circles of zeros. In order to tame noise amplification, we only calculate the deconvolution for spatial frequencies in the first lobe of the frequency response, that is, in the region of the frequency plane delimited by the first line or circle of zeros. As discussed before, gradiometers and magnetometers should ideally be designed so that the relevant information in the spectrum of the magnetic field does not extend past lines or circles of zeros. This way, we ensure that only the noise component is discarded.

Figure 10.27(a) shows the recovered field obtained by deconvolving the flux map shown in Figure 10.24(b), with white noise added to the flux so as to provide a

signal-to-noise ratio of 30 dB. The solution was obtained by calculating the deconvolution over the whole frequency plane, leading to degradation by noise amplification. By restricting the computation of the deconvolution to the first lobe of the gradiometer frequency response, we get the result shown in Figure 10.27(b). Similar recovery quality can be achieved for other sources, provided the spectrum of interest lies within the first lobe. Figure 10.27(c) shows the magnetic field produced by a magnetic dipole pointing in the z -direction, at a 5-mm liftoff, and Figure 10.27(d) shows the recovered field.

Note that restricting the calculation of the convolution to a region in the frequency plane is equivalent to applying a filter $h(k_x, k_y)$:

$$\tilde{\tilde{b}}_z(k_x, k_y, z) = \left[f_G^I(k_x, k_y) \varphi(k_x, k_y, z) \right] h(k_x, k_y) = \tilde{b}_z(k_x, k_y, z) h(k_x, k_y). \quad (10.147)$$

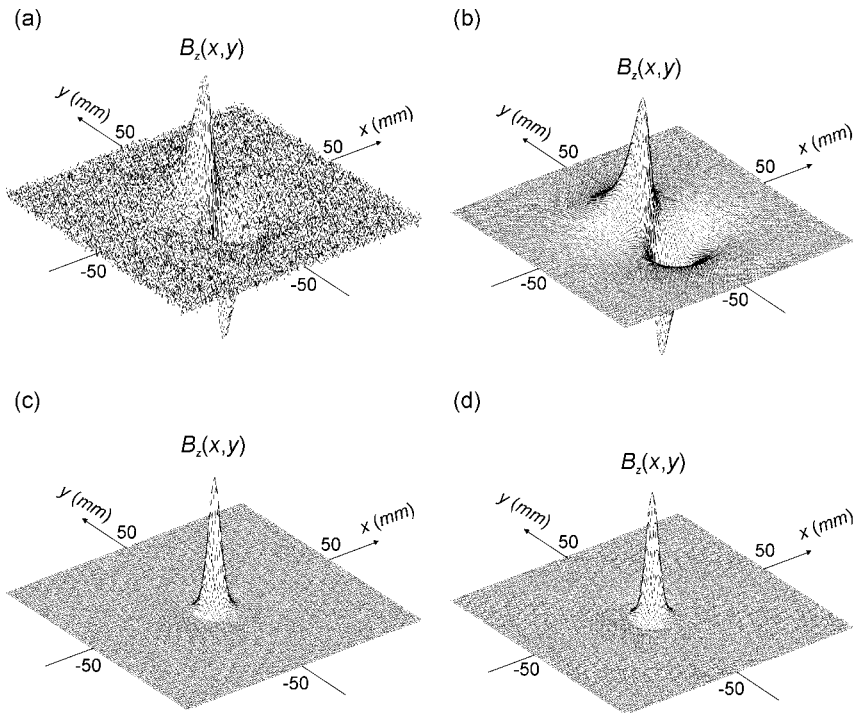


Fig. 10.27 Magnetic field recovered from flux maps with a 30-dB signal-to-noise ratio using the concentric planar design described before: (a) magnetic field map obtained by calculating the deconvolution over the whole spatial frequency plane; (b) magnetic field map obtained by restricting the calculation of the deconvolution to the first lobe of the

gradiometer spatial frequency response; (c) original magnetic field map associated with a magnetic dipole pointing in the z -direction, at a 5-mm liftoff; (d) recovered magnetic field map using the same concentric gradiometer as before, and restricting the deconvolution to the first lobe of the frequency response. (Adapted from Ref. [87], with permission.)

In the simplest case, h is a two-dimensional rectangular window: $h(k_x, k_y) = 1$ within the first lobe and $h(k_x, k_y) = 0$ everywhere else. In the space domain, this is equivalent to convolving the recovered field $\tilde{B}_z(x, y, z)$ with the inverse Fourier transform of $h(k_x, k_y)$, yielding $\tilde{B}_z(x, y, z)$. Depending on how narrow this window is, perceptible ringing can be introduced in $\tilde{B}_z(x, y, z)$, as a consequence of convolving with sinc or jinc⁸⁾ functions associated with the impulse response of ideal low-pass filters. Choosing other window types with smaller sidelobes or two-dimensional nonrecursive filters may considerably improve the quality of the recovered field.

Axial Gradiometers. In order to extend the modeling to include axial gradiometers, we first realize that the baseline effect is now decoupled from the field integration. Therefore, it is necessary to increase the dimension of the model. Let us suppose a generic axial gradiometer made up of N identically shaped coils with negligible thickness along the z -direction. The net flux in the gradiometer can then be expressed as

$$\Phi(x, y, z) = \int_{-\infty}^{+\infty} \int_{-\infty}^{+\infty} \int_{-\infty}^{+\infty} B_z(x', y', z') F_G(x - x', y - y', z - z') dx' dy' dz' \quad (10.148)$$

where

$$F_G(x, y, z) = \hat{F}(x, y) \sum_{j=0}^{N-1} n_j \delta(z - d_j). \quad (10.149)$$

The stepwise function $\hat{F}(x, y)$ is related to a normalized (single-turn) coil, while the number of turns and winding direction of each coil is given by n_j . Assuming the origin of the coordinate system at the center of the bottommost (pickup) coil, we have $d_0 = 0$ and each d_j is the distance of the j th coil to the pickup coil. Note that the delta function represents that the coils have no thickness, and therefore are “concentrated” at discrete values of z .

Taking the three-dimensional Fourier transform on (10.149), we obtain

$$f_G(k_x, k_y, k_z) = \hat{f}(k_x, k_y) \left(\sum_{j=0}^{N-1} n_j e^{-ik_z d_j} \right) = f_1(k_x, k_y) f_2(k_z), \quad (10.150)$$

which is the general expression for the spatial frequency response of an axial gradiometer. Even though f_G is separable, it is also a function of three variables, and therefore a graphic visualization is difficult to attain. However, if the coils are circular, (10.150) can be further simplified, since it becomes a function of just two spatial variables $k_\rho = \sqrt{k_x^2 + k_y^2}$ and k_z .

8) $\text{jinc}(x) = J_1(x)/x$.

As an example, consider an ordinary second-order axial gradiometer design, comprised of three circular coils of radius a , with N , $2N$, and N turns, separated by a baseline d . In this case, the gradiometer frequency response is given by

$$\begin{aligned} f_G(k_\rho, k_z) &= \hat{f}(k_\rho)N(1 - 2e^{-ik_z d} + e^{-i2k_z d}) \\ &= 4\pi a N \frac{J_1(ak_\rho)}{k_\rho} e^{-ik_z} [\cos(k_z d) - 1]. \end{aligned} \quad (10.151)$$

Should we wish to take the coil thickness into account, (10.150) can still be used, provided that we model a multi-turn coil as a stack of single-turn coils. In this way, j now sequentially indexes the turns of the coils and d_j stands for the distance between the (cumulative) j th turn and the first turn of the pickup coil. We observe that only f_2 is affected by this change.

It should be highlighted that (10.148) and (10.149) can also be used to model planar gradiometers, providing a way to compare the frequency responses of axial and planar configurations. By having $N=1$ and $d_0=0$ in (10.150), and having $\hat{f}(k_x, k_y)$ represent the two-dimensional planar gradiometer frequency response, we obtain the simple equation

$$f_G(k_x, k_y, k_z) = \hat{f}(k_x, k_y). \quad (10.152)$$

This equation expresses that the three-dimensional gradiometer frequency response is independent of k_z . Thus, the gradiometer behaves as an all-pass filter in the z -direction.

The deconvolution of (10.148) is much more complex than the two-dimensional case. In principle, a two-dimensional map is not enough to invert the equation and the flux must be known in a volume. This poses some serious experimental problems, as it requires mapping the field at several liftoffs and then interpolating the scans in order to generate a uniform three-dimensional grid of data. However, for deconvolution purposes an alternative approach is possible. Although it is not suitable to analyze the spatial frequency characteristics of gradiometers, it enables us to perform a two-dimensional deconvolution of a single flux map obtained with an axial gradiometer.

Let $\Phi(x, y, z_0)$ denote the net magnetic flux through the generic axial gradiometer described above, whose pickup coil is placed at a fixed height z_0 :

$$\Phi(x, y, z_0) = \sum_{j=0}^{N-1} n_j \int_{-\infty}^{\infty} \int_{-\infty}^{\infty} B_z(x', y', z_0 + d_j) \hat{F}(x - x', y - y') dx' dy'. \quad (10.153)$$

We can take the Fourier transform to obtain

$$\varphi(k_x, k_y, z_0) = \sum_{j=0}^{N-1} n_j b_z(k_x, k_y, z_0 + d_j) \hat{f}(k_x, k_y). \quad (10.154)$$

At first glance, it would appear that we cannot invert (10.154), since it relates (in the spatial frequency domain) magnetic fields at different heights $z_0 + d_j$ with a single flux at z_0 . Nevertheless, upward continuation can solve this problem, allowing us to bring all of the fields to a common single height z_0 :

$$\varphi(k_x, k_y, z_0) = \sum_{j=0}^{N-1} n_j b_z(k_x, k_y, z_0) e^{-d_j \sqrt{k_x^2 + k_y^2}} \hat{f}(k_x, k_y). \quad (10.155)$$

Therefore, (10.155) can now be inverted and solved for the field

$$\tilde{B}_z(x, y, z_0) = FT^{-1} \left\{ \frac{\varphi(k_x, k_y, z_0)}{\hat{f}(k_x, k_y) \left[\sum_{j=0}^{N-1} n_j e^{-d_j \sqrt{k_x^2 + k_y^2}} \right]} \right\}. \quad (10.156)$$

Note that, depending on the values of n_j and d_j , the term in square brackets may introduce other zeros in the deconvolution problem, in addition to the zero at the origin present in all gradiometer frequency responses. Also note that the deconvolution of the field integration and the deconvolution of the baseline can be carried out independently. In this way, depending on the parameter values associated with the experimental setup and the sensor, we can choose to undo just the predominant effect.

The model can be readily extended to incorporate axial gradiometers made up of coils of different sizes and/or shapes [68] if we assume different stepwise functions for each coil in (10.148). Similarly, (10.153) can be generalized to handle such designs.

Mapping Area. In addition to the sampling frequency and the scanning step size, discussed before, the mapping area also plays a significant influence on the quality of deconvolutions and solutions to the inverse problem. Let $\Phi(x, y, z)$ denote the magnetic flux through a gradiometer at a height z , associated with an arbitrary source distribution, and $\Phi'(x, y, z)$ denote the actual finite-length flux map. We define Φ' as

$$\Phi'(x, y, z) = \begin{cases} \Phi(x, y, z) & , \text{ for } (x, y) \text{ within the mapping area} \\ 0 & , \text{ otherwise.} \end{cases} \quad (10.157)$$

Equivalently,

$$\Phi'(x, y, z) = \Phi(x, y, z) W(x, y), \quad (10.158)$$

where $W(x, y)$ is a rectangular window representing the mapping area. Therefore, to determine the effect of using the truncated flux map Φ' instead of Φ on the recovered field $\tilde{B}_z(x, y, z)$, we replace φ by φ' in (10.141):

$$\begin{aligned}\tilde{\mathbf{B}}_z(x, y, z) &= FT^{-1} \left[f_G^1(k_x, k_y) \varphi'(k_x, k_y, z) \right] \\ &= FT^{-1} \left[f_G^1(k_x, k_y) \left(\varphi(k_x, k_y, z) \otimes w(k_x, k_y) \right) \right],\end{aligned}\tag{10.159}$$

where \otimes represents a convolution performed in the frequency domain. If the mapping area is large enough to ensure that $\Phi'(x, y, z) \approx \Phi(x, y, z)$ then the convolution with the product of sinc functions, which is associated with a two-dimensional rectangular window, can be neglected. Otherwise, significant distortion may be introduced in the recovered field, as it creates edges in the flux map and oscillations in the spectrum due to the sincs. An artifice that can be used to decrease this sort of distortion consists of generating a larger map by appending flipped/mirrored versions of the original map at its edges. Additional nonrectangular windows may then be applied to the enlarged map so as to taper the edges, thereby decreasing ringing in the recovered map.

A final remark is in order regarding computer implementation of deconvolution algorithms: when using FFT algorithms, one should be careful to sample (in the frequency domain) the continuous transforms, such as (10.143) and (10.145), the same way the FFT does. Otherwise, symmetries in the spectrum are broken and the recovered field contains a large complex component, besides being inaccurate.

Other Applications of Spatial Filtering

As can be seen from the breadth of applications we have just outlined, spatial filtering is a powerful approach. There are further applications of the technique relevant to magnetic imaging, including the interpretation of gradiometers as one-dimensional spatial filters, neglecting area effects [90–93], and the use of filters to determine multipole moments from measurement of the normal component of the field above the surface of a sphere or plane [94]. As a final remark, several improvements have been made to the inverse filtering method, notably for applications in magneto-optical imaging. In particular, Jooss and co-workers [95] extended the method to handle samples with finite thickness, and corrections have been introduced for the in-plane field effect [96]. In addition, there have been detailed studies of the influence of noise on the spatial resolution of the inverse filtering method [97].

Summary of Findings for Spatial Filtering

From this overview and the more detailed analyses of spatial filtering in the literature, we find that the coil-to-source spacing limits spatial resolution, that coil diameter should equal coil-to-source spacing, that inverse spatial filtering is unique in one and two dimensions, that inward continuation separates the problems of uniqueness from those of instability, that noise limits stability, that apodizing can improve spatial resolution and sensitivity, and that windowing to filter out noise and improve stability compromises spatial resolution. The spatial filtering approach is powerful and easy to implement with commercial software packages,

but it is limited primarily by the difficulty in applying specialized boundary conditions and utilizing other *a priori* knowledge of the sources. Planar current tomography offers promise for the characterization of the conductivity distribution within a planar conducting object, but further algorithm development is required. While spatial filtering at first glance is limited to two-dimensional problems, the use of inward and outward continuation makes it a versatile approach for some three-dimensional problems. Alas, it does not provide a solution to the nonuniqueness of the three-dimensional magnetic inverse problem.

10.3.2.3 Dipole Fitting

The conceptually easiest inverse solution is to divide the two-dimensional object into N elements, and then to assign an unknown current dipole to each element, *i.e.*, $p_{x,i}$ and $p_{y,i}$, where the magnetic field from the i th elemental current dipole is given by our differential form of the law of Biot and Savart ((10.32))

$$B_{z,i}(\vec{r}) = \frac{\mu_0}{4\pi} \frac{p_{x,i}(\vec{r}'_i)(y - y'_i) - p_{y,i}(\vec{r}'_i)(x - x'_i)}{|\vec{r} - \vec{r}'_i|^3}. \quad (10.160)$$

A least-squares solution, singular-value decomposition,⁹⁾ or an iterative approach can be used to determine the components of each elemental dipole [100]. The solution will be most stable when the magnetometer is close to the sample. While this approach can be used in three dimensions, troublesome instabilities can occur if more than a few dipoles are used. Even in two dimensions, there are several problems with this approach. For a large number of dipoles, the approach is computationally demanding. If there are no constraints between the adjacent dipoles, current will not be conserved. While a stable solution to the equation may be obtained, interpretation of the results in such a situation may be unclear. Furthermore, the presence of noise can lead to instabilities in the solution, particularly if a very fine discretization is used, and it can become necessary to devise constraints to avoid the appearance of large opposing dipoles in adjacent elements. Minimum norm techniques, discussed in Section 10.3.5 and in Chapter 11, may improve the performance of this approach [101], but at the risk of smoothing features in the inverse solution.

9) Let $\tilde{\tilde{\mathbf{A}}}$ be an $m \times n$ real matrix with $m > n$. Then $\tilde{\tilde{\mathbf{A}}}$ can be decomposed into a product of three matrices, using singular-value decomposition (SVD), $\tilde{\tilde{\mathbf{A}}} = \tilde{\tilde{\mathbf{U}}}\tilde{\tilde{\mathbf{\Sigma}}}\tilde{\tilde{\mathbf{V}}}^T$, where $\tilde{\tilde{\mathbf{U}}}$, $\tilde{\tilde{\mathbf{\Sigma}}}$, and $\tilde{\tilde{\mathbf{V}}}$ are matrices of dimensionality $m \times n$, $n \times n$, and $n \times n$, respectively. The

matrix $\tilde{\tilde{\mathbf{\Sigma}}}$ is diagonal and contains the singular values of $\tilde{\tilde{\mathbf{A}}}$ arranged in decreasing magnitude. Both $\tilde{\tilde{\mathbf{U}}}$ and $\tilde{\tilde{\mathbf{V}}}$ are unitary. For a detailed account of how to compute the SVD, see Refs. [98,99].

10.3.2.4 Methods for Regularization

Recently, Feldmann addressed the inversion of the Biot–Savart law with a more general method [102]. In this approach, the problem is formulated as a Fredholm integral equation of the first kind by expressing the current density in terms of a scalar field $F(x, y)$

$$\vec{J} = \nabla \times [F(x, y)\hat{z}], \quad (10.161)$$

which was proposed beforehand by Brandt [103]. Therefore, the z -component of the magnetic field is given by

$$B_z(x, y) = \int_{-\infty}^{+\infty} \int_{-\infty}^{+\infty} H(x - x', y - y') F(x', y') dx' dy'. \quad (10.162)$$

Three different kernels H were analyzed, depending on the geometry: slab, thin films of finite thickness, and sheet currents. Note that, in this method, we first obtain $F(x, y)$ and then we determine J_x and J_y by means of (10.161). Since (10.162) is an ill-posed problem, the Tikhonov–Philips regularization method is used to impose smoothness on the solution. Thus, the inversion of (10.162) is replaced by the minimization of

$$C(F, \lambda) = \left\| \int_{-\infty}^{+\infty} \int_{-\infty}^{+\infty} H(x - x', y - y') F(x', y') dx' dy' - B_z(x, y) \right\|_2^2 + \lambda \Omega[F], \quad (10.163)$$

with respect to F , where λ is the regularization parameter, the L^2 -norm of a function f of two variables is given by $\|f\|_2 = \sqrt{\int_{-\infty}^{+\infty} \int_{-\infty}^{+\infty} |f(x, y)|^2 dx dy}$, and the operator Ω , which measures the smoothness of F , is

$$\Omega[F] = \left\| \frac{\partial^2 F}{\partial x^2} + \frac{\partial^2 F}{\partial y^2} \right\|_2^2 \quad (10.164)$$

The minimizer of (10.163) is given by

$$\begin{aligned} F_\lambda(x, y) &= \\ &= \int_{-\infty}^{+\infty} \int_{-\infty}^{+\infty} \frac{|h(k_x, k_y)|^2}{|h(k_x, k_y)|^2 + \lambda (2\pi)^4 (k_x^2 + k_y^2)^2} \left[\frac{b_z(k_x, k_y)}{h(k_x, k_y)} \right] e^{i2\pi(k_x x + k_y y)} dk_x dk_y. \end{aligned} \quad (10.165)$$

A (sub)optimal value for λ can be found by means of the generalized cross-validation (GCV) method, which is based on statistical considerations. Therefore, in contrast to the inverse spatial filtering method presented before, in principle it is not necessary to obtain the regularization parameter (k_c for the inverse filtering) empirically.

A thorough comparison of inversion methods for the Biot–Savart law is also presented in Ref. [102], where the regularized integral equation, the inverse spatial filtering and the conjugate gradient (CG) methods were analyzed under noiseless and noisy conditions. (The iterative CG method is presented in Ref. [104].) The overall conclusion is that for noiseless and high-precision data, the CG method produces the best inversions, since it can automatically choose an optimal value for the regularization parameter directly from the data by means of the GCV method. In contrast, the automatic choice of the parameter for the integral equation method is far from the optimal value for noiseless data. It is important to highlight, though, that given the optimal values for the regularization parameters, all three methods yield excellent results in the noiseless case.

When data with realistic signal-to-noise ratios are used, the performance of the CG method is severely compromised, due to the lack of regularizing effect. However, excellent results were obtained over a broad range of signal-to-noise ratios with both the regularized integral equation and the inverse spatial filtering methods, and only slight differences in the quality of the inversions could be perceived. Consequently, the main drawback of the inverse filtering method is the lack of a criterion to determine the spatial frequency k_c . Although there are no theoretical impediments to automatically obtaining this parameter from the data, a reliable method has yet to be developed. Recently, a criterion has been proposed by Soika and Möller [105], but further systematic analyses are required to determine its applicability to different source distributions. Therefore, depending on the problem at hand, one may opt to use the more complex method of the regularized integral equation.

10.3.2.5 Lead Field Analysis

The intrinsic limitation of the three-dimensional magnetic inverse problem is the presence of degrees of freedom in the hypothetical current source distribution that are magnetically silent, such as spherical batteries or radially symmetric arrays of current dipoles. One particularly useful method to prevent the mathematical instabilities associated with the potential existence of silent sources is to use lead-field expansions to constrain the inverse problem so as to limit the set of sources only to those that produce measurable magnetic fields in the particular magnetometer arrangement used. Figure 10.28(a) shows how the energization of an ECG lead will produce a current distribution in the torso that provides information about the spatial sensitivity of that lead to current sources, while Figure 10.28(b) shows the same when an alternating current in a magnetometer pickup coil induces circulating currents in the torso, also providing information about the sensitivity of the magnetometer to cardiac current sources.

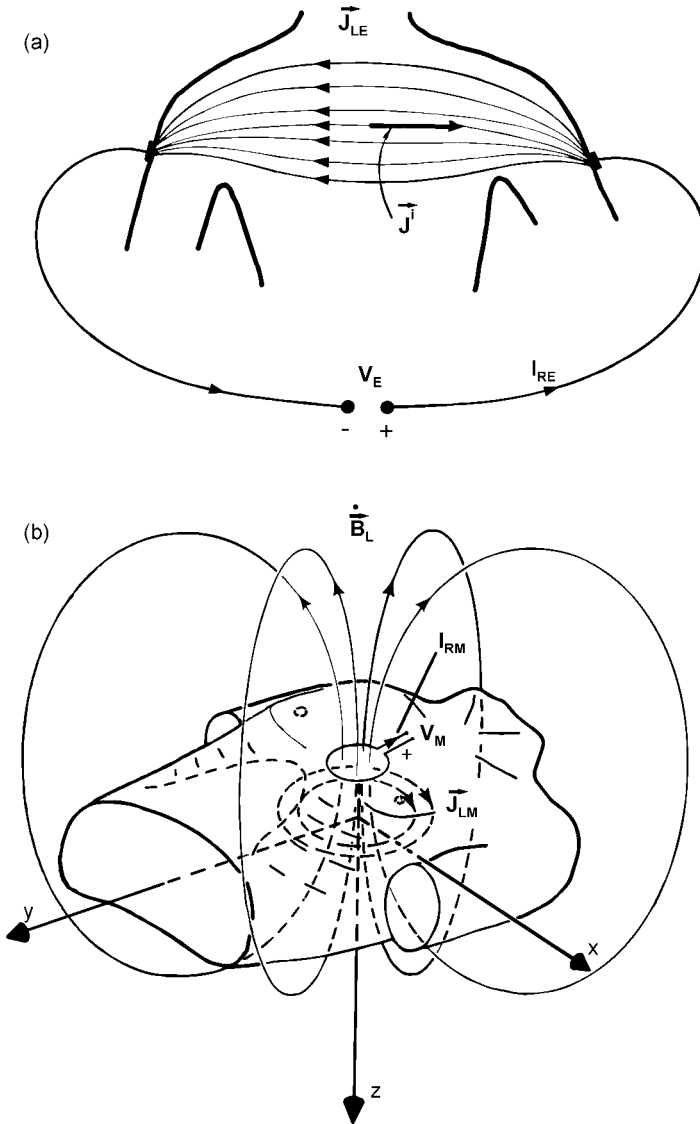


Fig. 10.28 A schematic representation of simple ECG and MCG leads and lead fields. Here, I_{RE} is the current used to “reciprocally” energize the electric lead and produce the electric lead field \vec{j}_{LE} . In the magnetic lead, a time-varying current I_{RM} produces a time-varying magnetic field B_L which by Faraday

induction produces the magnetic lead field. The outputs of the electric and magnetic leads, V_E and V_M , respectively, can be determined by summing the projection of each element of the impressed current density \vec{j} on the lead field current densities. (Adapted from Ref. [22], with permission.)

Lead Fields

To understand quantitatively the process outlined in Figure 10.28, we first need to define the lead fields [22, 106, 107]. Note that this analysis is valid either for a fixed array of N sensors, or for a scanning SQUID sensor that samples the magnetic field at N different positions \vec{r}_i . Suppose that a magnetometer measures B_z at a specific point \vec{r} . As shown in (10.65), this measurement represents a convolution of the source current distribution $\vec{J}(\vec{r}')$ and the Green's function $G(\vec{r}, \vec{r}')$ over the points \vec{r}' where both \vec{J} and G are nonzero. This Green's function is equivalent to a mutual inductance, M_{pq} , between a particular source element, $d\vec{p}$, of a current dipole distribution and a single, specific pick-up coil, q . The principle of reciprocity states that M_{pq} equals M_{qp} , which is equivalent to saying that the Green's function is the same whether the current source is at \vec{r} and the coil is at \vec{r}' or visa versa, *i.e.*, $G(\vec{r}, \vec{r}') = G(\vec{r}', \vec{r})$. The lead field $\vec{L}_i^J(\vec{r})$ for the i th magnetometer at \vec{r}_i is simply the current distribution \vec{J} that would be produced were the magnetometer pickup loop replaced by a coil carrying a low-frequency ac current. In this approach, the output of the i th SQUID magnetometer, a scalar variable, is simply the convolution of the source currents and the lead field for that magnetometer

$$B_i(\vec{r}) = \int_V \vec{L}_i^J(\vec{r}') \cdot \vec{J}(\vec{r}') d^3r' \quad (10.166)$$

Note the index i in \vec{L}_i^J contains within it the location \vec{r}_i , and hence we need not carry the dual-position notation of $G(\vec{r}, \vec{r}')$. If a current source at a particular point \vec{r}' is orthogonal to $\vec{L}_i^J(\vec{r}')$ at that same point, then that source cannot contribute to the field detected by the SQUID at \vec{r}_i . Reciprocally, a measurement of that component of the magnetic field cannot determine the strength of that component of the current source at \vec{r}' , although it may be able to detect another component at that location.¹⁰⁾ The requirement that the solution set is to be restricted to those currents that produce fields that can be measured by the chosen magnetometers is equivalent to stating that all of the imaged currents have to lie along the lines of the lead fields of one or more of the magnetometers.

Lead Field Expansions

Equation (10.166) suggests that we use the set of lead fields for our N magnetometers to constrain the inverse source distribution [78, 107, 108]. While lead-field expansions were originally developed for three-dimensional inverse problems, to maintain the consistency of our derivations we shall restrict ourselves to measurement of two-dimensional current distributions. We begin with the law of Biot and

10) This is an easy explanation for the inability of a SQUID to measure magnetic fields from radial dipoles in a conducting sphere: it is impossible, by means of external coils, to induce in the sphere eddy currents with radial components, *i.e.*, radial lead fields. For this reason, it is impossible to use exter-

nal coils to create a lead field that would detect a spherical battery. Also note that were we trying to measure a magnetization \vec{M} rather than a current \vec{J} , we would utilize the magnetic lead field \vec{L}^B , rather than the current lead field \vec{L}^J .

Savart for B_x at the i th measurement point above a two-dimensional current distribution

$$B_{x,i}(\vec{r}_i) = \left(\frac{\mu_0 d}{4\pi} \right) \int_S \frac{J_y(\vec{r}') (z_i - z')}{|\vec{r}_i - \vec{r}'|^3} dx' dy', \quad (10.167)$$

where S is the surface containing the sources. We can write this in terms of the lead field for that magnetometer

$$B_{x,i}(\vec{r}_i) = \int_S \vec{L}_i^J(\vec{r}') \cdot \vec{J}(\vec{r}') d^2 r'. \quad (10.168)$$

The dot product and the orientation of the lead field automatically selects the J_y component of the source current.

Let us suppose that we can expand $\vec{J}(\vec{r}')$ in terms of the nonorthogonal set of m lead-field functions \vec{L}_i^J

$$\vec{J}(\vec{r}') = \sum_{k=1}^m A_k \vec{L}_k^J(\vec{r}') w(\vec{r}'), \quad (10.169)$$

where $w(\vec{r}')$ is the *a priori* probability density for the current density, and A_k are the expansion coefficients. If we know, for example, that the currents in a particular region are zero, then we can at the beginning of our calculation set $w(\vec{r}')$ to zero at those locations. To determine A_k , we substitute (10.169) into (10.168), and exchange the order of summation and integration

$$B_{x,i}(\vec{r}_i) = \sum_{k=1}^m A_k \int_S \vec{L}_i^J(\vec{r}') \cdot \vec{L}_k^J(\vec{r}') w(\vec{r}') d^2 r'. \quad (10.170)$$

The field is thus

$$B_{x,i} = \sum_{k=1}^m P_{ik} A_k \quad (i = 1, 2, \dots, N) \quad (10.171)$$

where

$$P_{ik} = \int_S \vec{L}_i^J(\vec{r}') \cdot \vec{L}_k^J(\vec{r}') w(\vec{r}') d^2 r'. \quad (10.172)$$

While computation of P_{ik} can be tedious, it needs to be done only once for a particular measurement geometry. Singular-value decomposition or some other numerical technique is used to solve this set of linear equations for A_k , which are then

substituted into (10.169) to find $\vec{J}(\vec{r})$. The process can be iterated to refine the images, where $w(\vec{r})$ is adjusted each time. Figure 10.29 shows how this can be used to determine the distribution of currents flowing on the surface of a current-carrying tube with a small flaw [78, 108, 109]. This approach has the advantage that constraints can be applied through both the lead fields and the weighting function $w(\vec{r})$, but it is difficult to apply boundary conditions and other *a priori* knowledge of the source. In the case of the current-carrying tube, the lack of an analytical expression for the Fourier transform of the Green's function for currents flowing on the cylinder precludes the easy application of the Fourier transform approach. One limitation of the approach is that if there are too many magnetic field points, or too many basis functions are chosen, then the inner products used to determine P_{ik} are so similar to each other that the related matrix equation (10.171) becomes highly singular. Thus, for this approach, the number of magnetic field data points and basis functions must be limited [78].

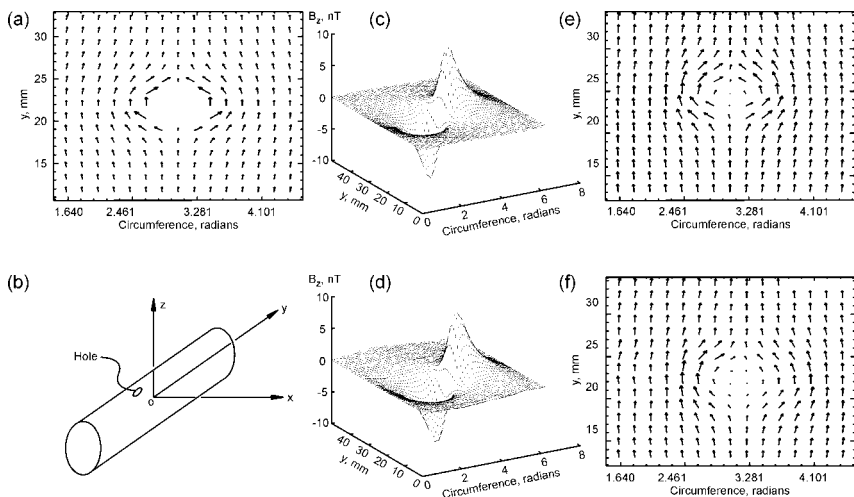


Fig. 10.29 An example of a lead-field inverse for a current-carrying tube with a small hole: (a) original current distribution; (b) geometry; (c) calculated magnetic field; (d) measured magnetic field; (e) currents reconstructed from theoretical magnetic field; (f) currents reconstructed from measured magnetic field. (Adapted from Ref. [136], with permission.)

As summarized by Tan [78], the lead-field analysis introduced by Ioannides [110] provides a method to constrain the current-imaging space. However, because the lead-field functions are defined over all space by using the *a priori* probability density function $w(\vec{r})$, lead-field analysis can incorporate only a constraint condition, such as the absence of current from a particular region, but not boundary conditions, such as the specification that current can flow only tangentially to an insulating boundary. Also, the lead-field interpolation functions are neither complete nor orthogonal, and this approach can recover only the components of the

current distribution to which the pickup coil is sensitive. Therefore, the reconstructions are sensitive to the choice of the measurement locations and hence the lead-field functions.

Sensor Array Optimization

The lead-field approach can be used to optimize sensor arrays for optimum inverse solutions [3], particularly with regard to the distribution of single-component *versus* vector magnetometers. Nalbach and Dössel analyzed the distribution of the sensors in a multichannel SQUID system and showed that fewer sensors nonuniformly distributed can provide better information to the inverse problem in MCG and ECG than a larger number of sensors distributed over a regular grid [4]. The lead-field method combined with realistic torso modeling was used to compare different sensor arrangements. In essence, the inverse problem consists of inverting the lead-field matrix, which in this analysis maps cardiac sources onto body surface potentials \tilde{b}_{el} or magnetic fields \tilde{b}_{mag}

$$\tilde{\mathbf{A}}\tilde{\mathbf{x}} = \tilde{b}_{mag,el} \quad \therefore \tilde{\mathbf{x}} = \tilde{\mathbf{A}}^{-1}\tilde{b}_{mag,el}. \quad (10.173)$$

Since the lead-field matrix is ill-conditioned, singular-value decomposition (SVD) is used to decompose $\tilde{\mathbf{A}}$, and to obtain an inverse solution

$$\tilde{\mathbf{A}} = \tilde{\mathbf{U}}\tilde{\Sigma}\tilde{\mathbf{V}}. \quad (10.174)$$

The matrix $\tilde{\mathbf{U}}$ can be seen as an orthonormal basis for the measurement space, and the matrix $\tilde{\mathbf{V}}$ as an orthonormal basis of the source space. The singular values, which are sorted in descending order in $\tilde{\Sigma}$, represent the magnitude with which vectors in the source space base are mapped into the measurement space base. Because a division by the singular values is performed in the calculation of the inverse solution, the slope of the singular value curve is related to the ill-posedness of the problem.

To obtain a sensor arrangement that is optimized for the inverse MCG, the calculation started with an even distribution of 990 sensors on a grid comprised of 15 elliptical layers surrounding the torso and containing 66 sensors each. If the canceling of a sensor did not change the set of maximal reconstructible base vectors, then such a sensor was discarded. Following this procedure, an optimized 32-channel arrangement was obtained. This configuration allowed the reconstruction of a larger number of base vectors than a 99-channel arrangement of evenly distributed sensors, comprised of 33 magnetometers, 33 planar gradiometers in the x -direction, and 33 planar gradiometers in the y -direction. It should be taken into account, though, that not every optimized configuration is feasible, due to constraints imposed by Dewar design.

10.3.2.6 The Finite-Element Method

One of the potentially most powerful approaches to the two-dimensional magnetic inverse problem may be the finite-element inverse, which can readily incorporate known source geometry and a wide variety of boundary conditions [78, 79]. Constrained reconstruction was originally proposed to solve the unbounded inverse Fourier transform problem in magnetic resonance imaging [111]. This method used a series of box-car functions as the interpolation functions to represent the original function, so that the solution of the inverse Fourier transform is bounded. Tan *et al.* [79] examined the applicability of this approach to the magnetic imaging problem and then developed a more flexible approach that utilized the finite-element interpolation functions. A recent comparison of the finite-element method (FEM) *versus* the boundary-element method (BEM) for lead-field computation in ECG is provided in Ref. [112].

We can write the Biot-Savart law for the z -component of the magnetic field above a two-dimensional current distribution $\vec{J}(x, y)$ in the xy -plane at $z = 0$ in the expanded form

$$B_z(x, y, z) = \frac{\mu_0 d}{4\pi} \int \frac{J_x(x', y')(y - y') - J_y(x', y')(x - x')}{[(x - x')^2 + (y - y')^2 + z^2]^{3/2}} dx' dy'. \quad (10.175)$$

In order to reconstruct the current image \vec{J} from the magnetic field data recorded in the xy -plane at a height z above the current distribution, we section the current-source space into a mesh of elements, as shown in Figure 10.30, that represents our prior knowledge about the conductor geometry.

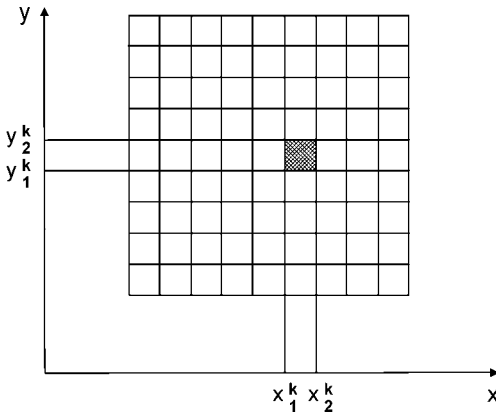


Fig. 10.30 A finite-element mesh describing a square conducting sheet. (Adapted from Ref. [79], with permission.)

We can represent the current distribution $\vec{J}(\vec{r})$ anywhere within an element k by using a set of two-dimensional interpolation functions and the values of the current at the nodes in the mesh

$$\begin{aligned} J_x^k &= \sum_j J_{xj}^k N_j^k(x', y') \\ J_y^k &= \sum_j J_{yj}^k N_j^k(x', y'), \end{aligned} \quad (10.176)$$

where N_j^k are the two-dimensional interpolation functions for the k th element, J_{xj}^k , J_{yj}^k is the set of the nodal values that need to be determined, and j is the index for all interpolation functions in a single element. With this approach, we need to specify the values of the currents only at the nodes of the mesh; the interpolation functions provide us with analytical expressions for determining the current at all other points in the sample. As we did with the lead-field expansion for the current, we substitute (10.176) into (10.175), sum up all the elements, and reverse the order of summation and integration to obtain a set of linear equations that describe the magnetic field

$$[B_{zi}] = \sum_k \left[A_{zi,xj}^k \right] [J_{xj}^k] - \left[A_{zi,yj}^k \right] [J_{yj}^k], \quad (10.177)$$

where the subscript i stands for the i th measurement point and

$$A_{zi,xj}^k = \frac{\mu_0 d}{4\pi} \int \int_{(k)} \frac{N_j^k(x', y')(y_i - y')}{\left[(x_i - x')^2 + (y_i - y')^2 + z^2 \right]^{3/2}} dx' dy' \quad (10.178)$$

$$A_{zi,yj}^k = \frac{\mu_0 d}{4\pi} \int \int_{(k)} \frac{N_j^k(x', y')(x_i - x')}{\left[(x_i - x')^2 + (y_i - y')^2 + z^2 \right]^{3/2}} dx' dy'. \quad (10.179)$$

If we measure B_{zi} , calculate all A^k and invert (10.177), we should be able to solve for J_{xj}^k and J_{yj}^k . However, because we are measuring only one variable (B_z) over the mesh of the field map and are trying to determine two variables (J_x) and (J_y) over a coarser mesh of a current map, it may be difficult or impossible to solve (10.177) for J_x and J_y , since the equations can be highly singular and unstable. As before, we can incorporate the current-continuity condition to improve greatly the stability of the solution from B_z . Similar equations can be derived for measurement of either B_x or B_y

$$[B_{xi}] = \sum_k \left[A_{xi,yj}^k \right] [J_{yj}^k] \quad (10.180)$$

$$\begin{bmatrix} B_{yi} \end{bmatrix} = \sum_k \begin{bmatrix} A_{yi,xj}^k \end{bmatrix} \begin{bmatrix} J_{xj}^k \end{bmatrix}, \quad (10.181)$$

where

$$A_{xi,yj}^k = -A_{yi,xj}^k = \frac{\mu_0 d}{4\pi} \int \int_{(k)} \frac{N_j^k(x', y') z}{[(x_i - x')^2 + (y_i - y')^2 + z^2]^{3/2}} dx' dy'. \quad (10.182)$$

Because B_x is determined solely by J_y , and B_y by J_x , the determination of a single component by the measurement of only one tangential component is straightforward. The continuity equation can be used to determine the other component. Alternatively, the independent measurement of B_x and B_y would allow the imaging of both J_x and J_y , and hence the determination of whether or not current was conserved on the surface being mapped. This may be of great practical importance for the creation of maps of an effective surface corrosion current for three-dimensional objects, since the surface-current distribution will be determined by underlying galvanic activity.

It is time consuming to calculate A^k and their inverses, but since they depend only upon the geometry of the finite-element mesh and the measurement arrangement, they must be calculated only once for each measurement configuration. On the other hand, once the inverses are determined, calculating a particular solution is computationally modest.

Continuous Two-Dimensional Current Distributions

In SQUID nondestructive evaluation (NDE), we encounter two types of current-imaging problems: those with a continuous current distribution, such as when a uniform current sheet is perturbed by a localized flaw, for which the electrodes used to apply the current to the test object are distant and can be ignored; and those problems with a discontinuous current distribution, as would occur when current is injected into the planar sample by vertical wires, as shown in Figure 10.18. As an example of the first case, Figure 10.31 shows a simulation using the square current pattern.

For this application, we can use a bilinear finite element with an interpolation function of the form [79]

$$N_j^k(x, y) = a_j^k + b_j^k x + c_j^k y + d_j^k xy, \quad (10.183)$$

where a_j^k, b_j^k, c_j^k and d_j^k are the parameters specific to the k th element. Inside the k th element, the current distribution $\vec{J}(x, y)$ can be expressed in terms of the vector current density \vec{S}_n at the four corners

$$\begin{aligned} J_x^k &= \mathfrak{S}_{x1}^k N_1^k + \mathfrak{S}_{x2}^k N_2^k + \mathfrak{S}_{x3}^k N_3^k + \mathfrak{S}_{x4}^k N_4^k \\ J_y^k &= \mathfrak{S}_{y1}^k N_1^k + \mathfrak{S}_{y2}^k N_2^k + \mathfrak{S}_{y3}^k N_3^k + \mathfrak{S}_{y4}^k N_4^k \end{aligned} \quad (10.184)$$

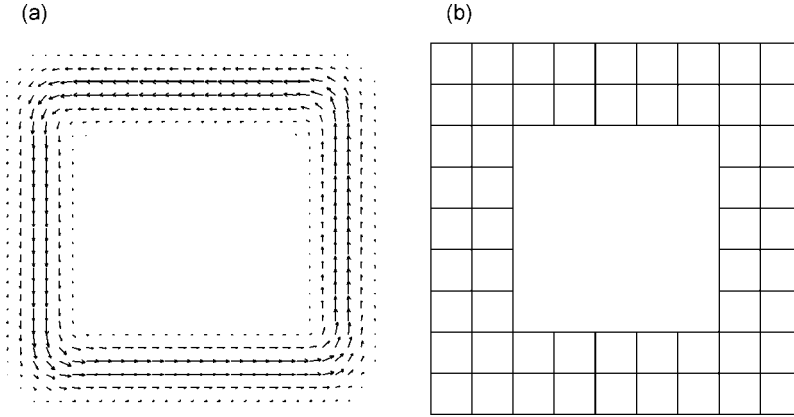


Fig. 10.31 Finite-element model for a bounded source: (a) the simulated current source used to test the continuous-current reconstruction algorithm; (b) the grid used to section the current space corresponding to (a). (Adapted from Ref. [79], with permission.)

We can utilize within each element a set of normalized, local coordinates, termed natural coordinates η and ξ , that range from +1 to -1, so that we can write the continuity condition ((10.75)) as

$$\frac{\partial J_x}{\partial \xi} \frac{\partial \xi}{\partial x} + \frac{\partial J_y}{\partial \eta} \frac{\partial \eta}{\partial y} = 0. \quad (10.185)$$

Substituting (10.184) into the above equation and sorting the coefficients by the order of the polynomial, we obtain a polynomial expression for the continuity equation [79]

$$\begin{aligned} & \frac{1}{a^k} \left(-\mathfrak{J}_{x1}^k + \mathfrak{J}_{x2}^k - \mathfrak{J}_{x3}^k + \mathfrak{J}_{x4}^k \right) + \frac{1}{b^k} \left(-\mathfrak{J}_{y1}^k - \mathfrak{J}_{y2}^k + \mathfrak{J}_{y3}^k + \mathfrak{J}_{y4}^k \right) + \\ & \frac{1}{a^k} \left(\mathfrak{J}_{x1}^k - \mathfrak{J}_{x2}^k - \mathfrak{J}_{x3}^k + \mathfrak{J}_{x4}^k \right) \eta + \frac{1}{b^k} \left(\mathfrak{J}_{y1}^k - \mathfrak{J}_{y2}^k - \mathfrak{J}_{y3}^k + \mathfrak{J}_{y4}^k \right) \xi = 0. \end{aligned} \quad (10.186)$$

Since the coordinates ξ and η are independent of each other, each term of the polynomial must be individually zero to ensure that the continuity condition is satisfied in every element. Thus, we obtain a set of equations governing the coefficients J_{xj}^k and J_{yj}^k

$$\begin{aligned} & \frac{1}{a^k} \left(-\mathfrak{J}_{x1}^k + \mathfrak{J}_{x2}^k - \mathfrak{J}_{x3}^k + \mathfrak{J}_{x4}^k \right) + \frac{1}{b^k} \left(-\mathfrak{J}_{y1}^k - \mathfrak{J}_{y2}^k + \mathfrak{J}_{y3}^k + \mathfrak{J}_{y4}^k \right) = 0 \\ & \left(\mathfrak{J}_{x1}^k - \mathfrak{J}_{x2}^k - \mathfrak{J}_{x3}^k + \mathfrak{J}_{x4}^k \right) = 0 \\ & \left(\mathfrak{J}_{y1}^k - \mathfrak{J}_{y2}^k - \mathfrak{J}_{y3}^k + \mathfrak{J}_{y4}^k \right) = 0. \end{aligned} \quad (10.187)$$

By incorporating the continuity condition ((10.187)) into one of the reconstruction equations ((10.177), (10.180), or (10.181)), we can obtain the images of the current density using only one component of the magnetic field [78, 79].

Since the finite-element method can deal with each individual element, any kind of boundary condition is easy to incorporate into the solution. For instance, a bounded current source usually will not allow current to flow out of the edge, which corresponds to the boundary condition

$$\vec{\mathbf{j}} \cdot \hat{\mathbf{n}} = 0. \quad (10.188)$$

Because the interpolation functions in the finite-element method are designed so that the nodal values are simply the current densities at the nodes, if the nodal values of the current component normal to the edge are zero, then this boundary condition is satisfied along that edge.

To demonstrate this approach, consider a 11.7 mm \times 12.6 mm current loop as shown in Figure 10.31(a). The current distribution does not have sharp edges to avoid problems with spatial aliasing that would occur with the spatial-filtering inverse. We assume that the shape of the conductor is known, and hence we can create the finite-element mesh shown in Figure 10.31(b). In an ideal case, when no noise is present in the data and the magnetic field is recorded very close to the current source, the filtering technique, which involves only a fast Fourier transform (FFT), a two-dimensional multiplication, and an inverse FFT, has the advantages of dealing with a large amount of data quickly and provides an excellent result. However, even a small amount of noise will reduce severely the quality of the image produced by the filtering technique, producing current noise over the entire image plane, while the finite-element method controls the effects of the noise in the magnetic field by restricting the current to within the correct boundary.

To demonstrate this, we calculate the z -component of the magnetic field as would be measured at $z = 1.5$ mm and at $z = 3$ mm, and then add spatially white noise so that the signal-to-noise ratios (SNRs) are 20-to-1 and 5-to-1, respectively. For the finite-element inverse, we sample the magnetic field over a 25 mm \times 25 mm area with 1 mm spacing, *i.e.*, 26×26 points. Since the spatial-filtering inverse can readily use more data points without requiring the inversion of a giant matrix, we can sample the field over the same region with a 60×60 mesh. Figures 10.32(a) and (b) show the results of the filtering technique and the finite-element method, respectively, for $z = 1.5$ mm and a SNR of 20. The mean-square deviation (MSD) for the result from the filtering technique (Figure 10.32(a)) increases from 0.002 to 0.133, which means that even a 5% noise level will degrade the quality by a factor of 60 over the reconstruction from the noise-free data. In contrast, the MSD for the finite-element method (Figure 10.32(b)) increases only from 0.026 to 0.040. While the finite-element approach with 26×26 noise-free field points at 1.5 mm provides images that are coarser than obtained by the 60×60 data used with the filtering approach, the image quality is degraded less quickly by noise for the finite-element approach, so that in the presence of only a small amount of noise, the finite-element approach provides superior results.

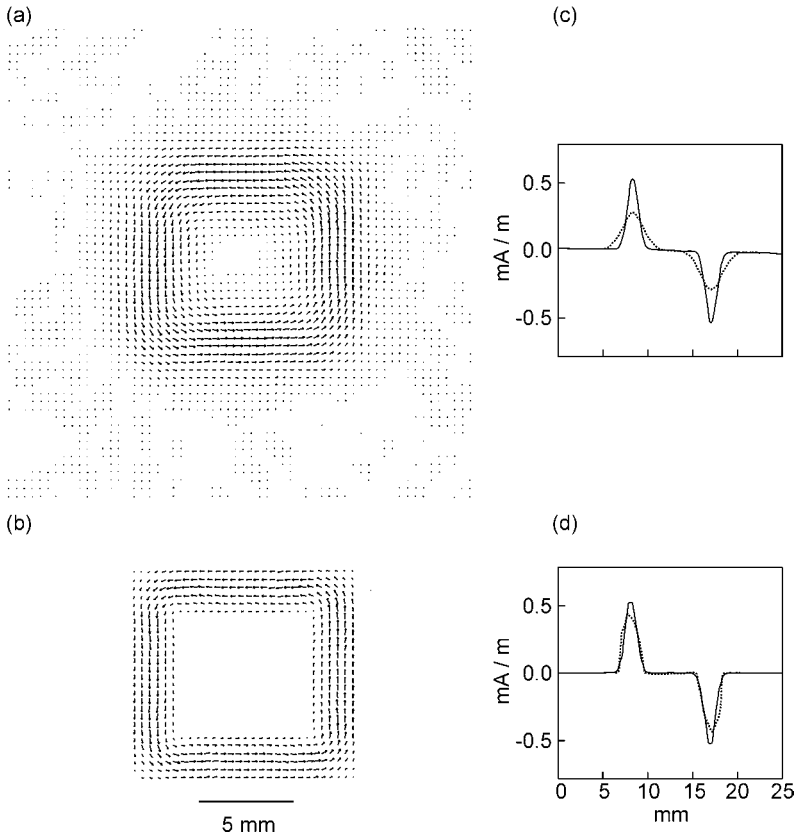


Fig. 10.32 The reconstructions by the filtering technique (a,c) and the finite-element method (b,d) at $z = 1.5$ mm with $\text{SNR} = 20$. (a,b) Reconstructed images of the current; (c,d) cross-section of J_x . The solid and dotted lines in (c) and (d) are the original current distribution and the reconstruction. (Adapted from Ref. [79], with permission.)

The advantage of the finite-element approach is even more apparent for B_z measured at 3 mm with a SNR of 5, shown in Figure 10.33. The filtering result in Figure 10.33(a) has an MSD of 0.42, whereas the finite-element method, shown in Figure 10.33(b), has an MSD of 0.12.

Discontinuous Two-Dimensional Current Sources

In measurements when current is injected into a conductor, as in Figure 10.18, there is a discontinuity in the current in the plane at the location of the two electrodes. In the filtering technique, we can address this with source/sink terms in the equation of continuity; in the finite-element approach, the continuity equation (10.187) can be modified for the elements containing the sources [79]. However, the accuracy of the reconstruction in the immediate vicinity of the electrode may be unsatisfactory. The usual approach would be to modify the mesh to have a very

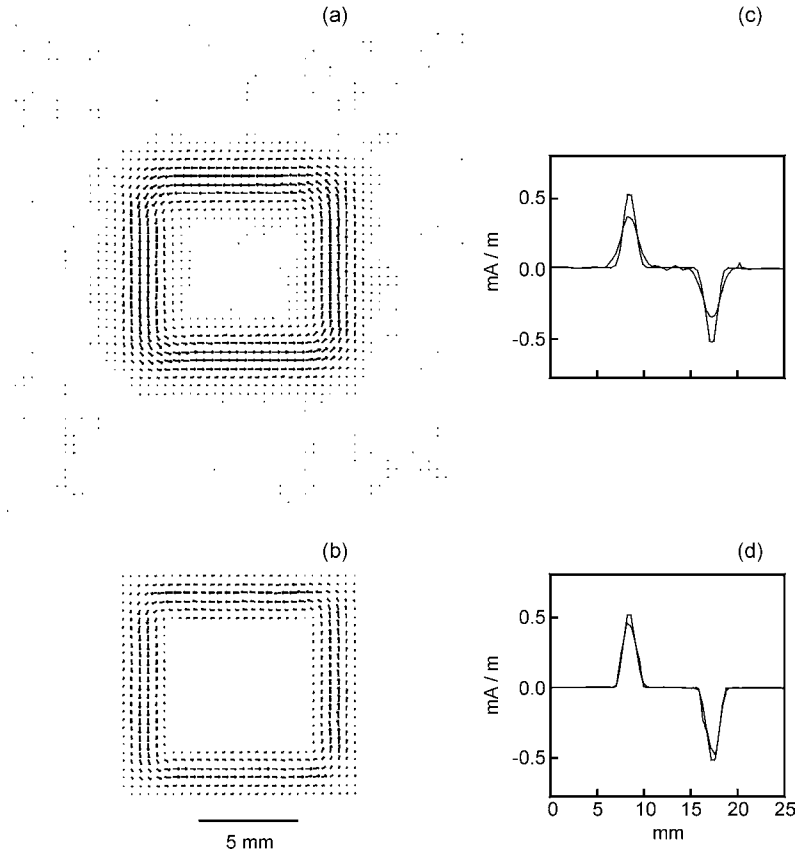


Fig. 10.33 The reconstructions by the filtering technique (a,c) and the finite-element method (b,d) at $z = 3.0$ mm with $\text{SNR} = 5$. (a,b) Reconstructed images of the current; (c,d) cross-section of J_x . The solid and dotted lines in (c) and (d) are the original current distribution and the reconstruction. (Adapted from Ref. [79], with permission.)

fine discretization in the immediate vicinity of the electrodes. However, with the finite-element inverse approach, such mesh refinement would drastically increase the size of the matrix that had to be inverted by singular-value decomposition or some other solver. An alternative approach is to superimpose two currents: a divergent current \vec{J}_d that correctly represents the current in the immediate vicinity of the two electrodes, and a continuous component \vec{J}_c , such that

$$\vec{J} = \vec{J}_d + \vec{J}_c. \quad (10.189)$$

For the divergent part, we assume that the current corresponds to that associated with the potential V produced by a pair of point electrodes at voltages $\pm U$ in an unbounded homogeneous conducting sheet, where

$$V = U \log \sqrt{(x - x_1)^2 + (y - y_1)^2} - U \log \sqrt{(x - x_2)^2 + (y - y_2)^2}, \quad (10.190)$$

so that

$$\begin{aligned} J_{dx} &= \frac{\partial V}{\partial x} \\ &= \frac{U(x - x_1)}{(x - x_1)^2 + (y - y_1)^2} - \frac{U(x - x_2)}{(x - x_2)^2 + (y - y_2)^2}, \end{aligned} \quad (10.191)$$

$$\begin{aligned} J_{dy} &= \frac{\partial V}{\partial y} \\ &= \frac{U(y - y_1)}{(x - x_1)^2 + (y - y_1)^2} - \frac{U(y - y_2)}{(x - x_2)^2 + (y - y_2)^2}. \end{aligned} \quad (10.192)$$

Then the deconvolution problem reduces to trying to find the divergence-free component \vec{J}_c such that the total current \vec{J} will produce the correct magnetic field while satisfying both the boundary condition

$$(\vec{J}_d + \vec{J}_c) \cdot \hat{n} = 0, \quad (10.193)$$

and also the continuity condition

$$\nabla \cdot \vec{J}_d = U\delta(\vec{r} - \vec{r}_1) - U\delta(\vec{r} - \vec{r}_2), \quad (10.194)$$

$$\nabla \cdot \vec{J}_c = 0. \quad (10.195)$$

Examples of this approach are presented in [79].

Eliminating Edge Fields

When current is passed through a conducting object of finite dimension, the discontinuity of the current at the edges of the object can produce large magnetic fields whose gradients will limit the ability to detect small flaws or field perturbations within the object either by direct imaging or by inverse solution. In terms of the inverse problem, the presence of the edges produces a large signal that could dominate the inverse process to the exclusion of smaller features. This was first recognized when trying to determine the smallest possible hole in a plate that could be detected by SQUID imaging of injected currents. There are a number of solutions to this problem involving either software preprocessing before an inverse calculation, or even with hardware at the time of data acquisition. Figure 10.34 shows how this can be accomplished by using a canceling plate that has a uniform current distribution passing beneath the sample, but in the opposite direction [113]. This approach may be useful for SQUID NDE measurements on

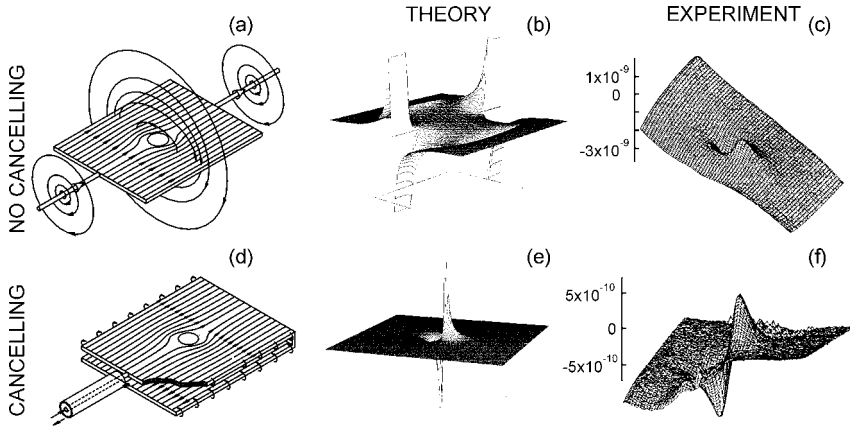


Fig. 10.34 The effects of conductor edges and the use of a canceling plate in the detection of small flaws in a conducting object: (a) the injection of current into a planar conductor with a hole; (b) the predicted magnetic field; (c) the magnetic signature of the hole;

(d) the use of a canceling plate and a coaxial cable to deliver the current to the sample; (e,f) the measured magnetic field (scale range 1 nT). (Adapted from Ref. [113], with permission.)

long samples, such as at the end of a continuous aluminum extruder or rolling mill. As software preprocessing, the calculated magnetic field from an appropriately shaped plate can be subtracted from the recorded magnetic image, with the caveat that the SQUID must have an adequate field resolution (e.g., low digitization error) and linearity so as to not introduce additional artifacts.

An alternative approach is to use spatial filters, which can take the form of physical gradiometers, or synthetic ones (consistent with the limitations imposed by resolution and linearity) that are matched to the magnetic signature of the flaw of interest [114]. Figure 10.35 shows a simulation of how the edge effects of the internal structure of the lower wing splice of an F-15 aircraft can be eliminated by digital filtering. More importantly, this study also demonstrates that physical or synthetic planar gradiometers can be designed to detect small flaws in large background signals. A spatial filter that is matched to the magnetic signature of the flaw of interest represents a physical detector or algorithm that is sensitive to a particular inverse solution but insensitive to others. This approach can be generalized to any situation where a desired signature may be buried within a larger background field. A gradiometer might be configured, either in hardware or software, to optimize detection of that signature. Scanning of this synthetic gradiometer corresponds to the convolution of the gradiometer transfer function with the magnetic field. The advantage of doing this as a preprocessing step in the inverse solution is that different filters can be compared since all of the original field distribution was recorded prior to analysis.

The finite-element technique also can be used to eliminate edge fields from recorded field distributions, thereby enhancing the signals from any interior

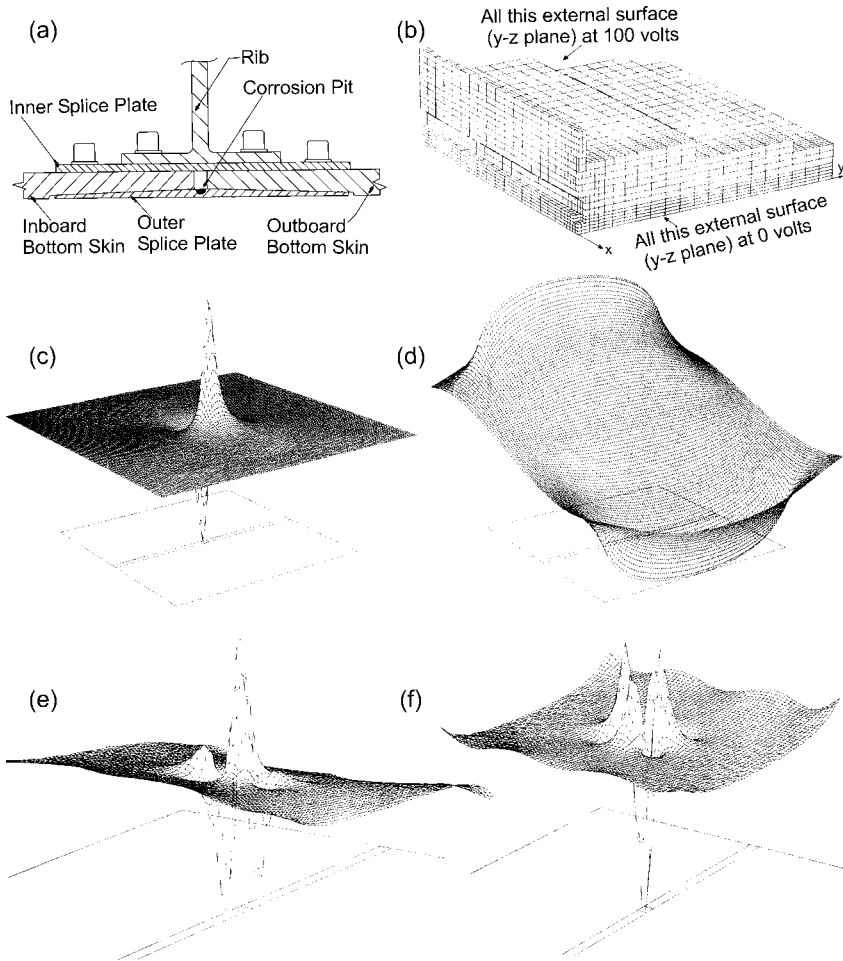


Fig. 10.35 Simulations of the magnetic signature of a small region of hidden corrosion in an F-15 lower wing splice. (a) Schematic cross-section of the splice. (b) The finite-element mesh describing one-quarter of a section of wing splice. A uniform current is applied parallel to the x -axis. (c) The magnetic signature of the flaw alone. (d) The magnetic field from the wing structure and the flaw. The

peak-to-peak signal arising from the edges of the various plates in the splice is 400 times larger than that of the flaw. (e, f) The simulated output of a SQUID gradiometer configured to reject large-scale spatial variations such as from the wing structure and selectively detect fields from localized flaws. (Adapted from Ref. [114], with permission.)

structure [79]. Equation (10.15) shows that we can write the law of Biot and Savart in terms of a surface integral of the discontinuity in the tangential component of the current density \vec{J} , and the volume integral of the curl of \vec{J} . In two dimensions, the surface integral reduces to a line integral over the boundary b of the sample, and the volume integral to an integral over the two-dimensional surface S , so that

$$B_z(\vec{r}) = \frac{\mu_0 d}{4\pi} \oint_b \frac{\vec{J}(\vec{r}') \cdot d\vec{l}'}{|\vec{r} - \vec{r}'|} + \frac{\mu_0 d}{4\pi} \int_s \frac{[\nabla' \times \vec{J}(\vec{r}')]_z}{|\vec{r} - \vec{r}'|} dx' dy'. \quad (10.196)$$

Following the approach in Tan *et al.* [79], we can use Ohm's law

$$\vec{J} = -\sigma \nabla V, \quad (10.197)$$

the curl of this expression,

$$\begin{aligned} \nabla \times \vec{J} &= -\nabla \times (\sigma \nabla V) \\ &= -\nabla \sigma \times \nabla V \\ &= \nabla \times (V \nabla \sigma), \end{aligned} \quad (10.198)$$

and standard vector identities to rewrite (10.196) as

$$B_z(\vec{r}) = \frac{\mu_0 d}{4\pi} \oint_b \frac{\vec{J}(\vec{r}') \cdot d\vec{l}'}{|\vec{r} - \vec{r}'|} + \frac{\mu_0 d}{4\pi} \int_s \frac{[V(\vec{r}') \nabla' \sigma(\vec{r}') \times \vec{r}']_z}{|\vec{r} - \vec{r}'|} dx' dy'. \quad (10.199)$$

If the medium is homogeneous and isotropic, $\nabla' \sigma = \vec{0}$, and the second integral is zero, which means that the magnetic field depends only on the current tangential to the edge, *i.e.*, the first integral. If the test object has a nonuniform or anisotropic conductivity, the second term will contribute. The finite-element technique provides us with a powerful tool for separating these two contributions: the magnetic field is used with the finite-element inverse to determine the current distribution in a homogeneous, isotropic sample of the correct shape. This current is then used with the first integral of (10.199) to compute the magnetic field produced by the edges. If this is identical to the measured field, the sample is homogeneous and isotropic. If the two fields differ, then there are internal inhomogeneities or anisotropies. This approach may provide a means for enhancing the sensitivity of SQUID imaging to detect internal flaws in metallic structures.

10.3.2.7 Phase-Sensitive Eddy-Current Analysis

So far, we have discussed only the injection of current into conducting samples. While the injected-current technique is useful for high-precision measurements on test samples, the need to make good electrical contact with the sample would make it difficult to use on painted structures such as airplanes. It is also possible to use sheet inducers, first demonstrated with the MagnetoOptic Imager (MOI) [115, 116] in which the oscillating magnetic field is applied tangential to the surface of the test object by a sheet conductor or set of wires parallel to the test surface. This induces a large-extent sheet current in the test specimen, and thus produces flaw perturbation fields quite similar to those obtained with direct-current

injection. While beyond the scope of this chapter, it is important to recognize that this approach can be applied to inverse determinations, wherein SQUID data from this technique produce images suitable for deconvolution, and phase-sensitive analysis techniques can provide an additional degree of feature discrimination based upon flaw depth [117–120]. In this situation, the phase of the eddy current induced in a planar sample is a function of depth. At the surface of the sample, the eddy currents lead the magnetic field by approximately 90° . At low frequencies, the eddy-current phase is reasonably constant within the sample. At frequencies such that the skin depth is one-tenth of the thickness of the plate, there are large changes in the phase shift between the surface and the center of the sample. By using a vector lock-in amplifier and software phase-rotation techniques, we can image the component of the magnetic signal from the eddy currents at any desired phase relative to the applied field [119, 120]. Because of a frequency-dependent reversal of the sign of the eddy currents with depth, this technique also offers the possibility of three-dimensional current tomography [119, 120].

10.3.2.8 Summary of Inverse Magnetic Imaging of Current Distributions

As can be seen from the preceding analyses, the deconvolution of magnetic field maps to obtain images of current distributions can be addressed with a wide variety of mathematical techniques. There are others, such as an iterative perturbative approach using cubic splines [121] and a volume-integral approach [122], that have not been discussed here, and undoubtedly more techniques will be developed. In the perturbative approach, for example, the monopole and dipole terms of the electric potential can be computed analytically [123]. Likely candidates for further development as an inverse technique are the boundary integral [124–126] and resolution field [127, 128] methods. The geophysics literature is rich in sophisticated techniques [129–132]. A major limitation of the entire deconvolution process is that it is still more of an art than a science: there is no simple recipe to determine which approach is preferable for a particular combination of measurement geometry, noise, and current distribution. Until such a recipe is developed, it may be necessary to determine empirically the optimal technique for a particular application.

10.3.3

Imaging Magnetization Distributions

10.3.3.1 The Dipole Field Equation

Virtually all materials are magnetic, *i.e.*, they perturb to some extent an applied magnetic field. The perturbation is large if the material is iron, and very small if it is water or plastic. The perturbations of this field can be imaged, as shown schematically in Figures 10.2(b) and (g) and in the data in Figures 10.36 and 10.37. Such data can be used to determine the nature of the object that produced the perturbation, generally in terms of the magnetization or magnetic susceptibility

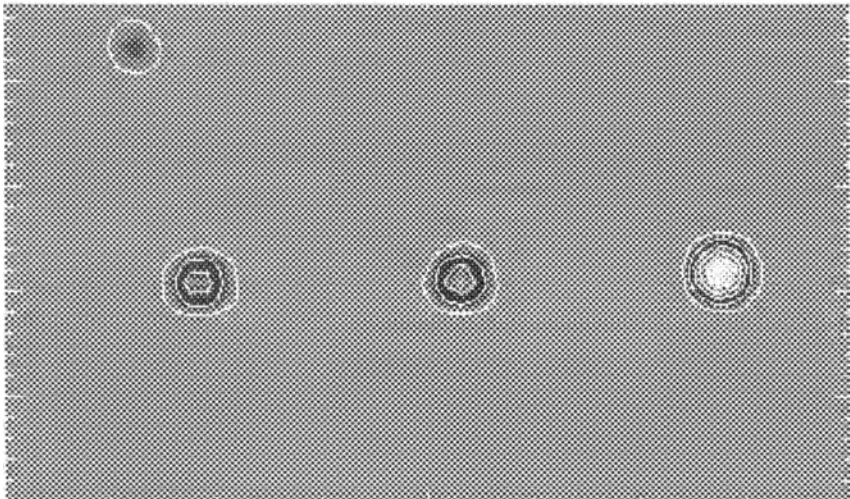
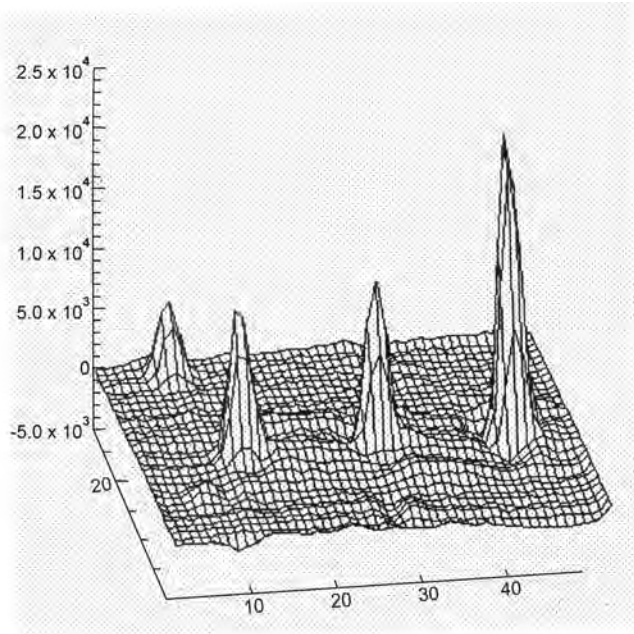


Fig. 10.36 Magnetic decoration of surface defects. A nickel NDE sample had electric discharge machined (EDM) slots with dimensions of $\sim 100\ \mu\text{m}$, that were filled with a superparamagnetic tracer. The magnetic field was recorded 2.0 mm from the sample with a 174- μT applied field. These susceptibility

images display the location and size of surface defects, including one (upper left) that was the result of a previously undetected scratch. MicroSQUID can find flaws as small as $2 \times 10^{-12}\text{m}^3$. (Adapted from Ref. [137], with permission.)

of the object. To see how this is accomplished, we need to start with a single magnetic dipole, whose field is given by (10.1), and whose inverse is given by (10.2). While this approach is appropriate for Figure 10.36, it may not work when we have multiple dipoles, or a distribution of dipoles in the form of a dipole density or magnetization as in Figure 10.37. In these latter cases, the inversion process is not so straightforward.

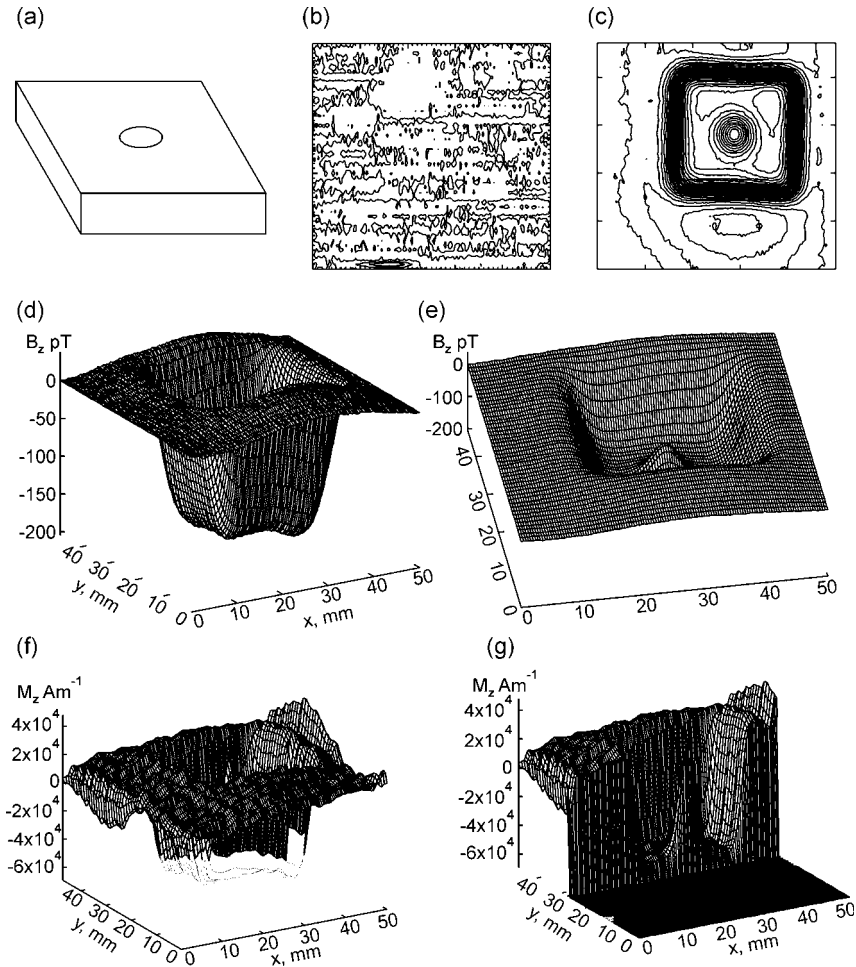


Fig. 10.37 Susceptibility images of Plexiglas. A 25.4-mm square sample of Plexiglas containing a 4.5-mm diameter hole was magnetized in a 110- μT applied field and scanned at a distance of 2.0 mm. (a) The sample; (b,c) contour maps of the recorded field B_z with (b) $B_{\text{app}} = 0 \mu\text{T}$ and (c) $B_{\text{app}} = 100 \mu\text{T}$;

(d,e) surface maps of the recorded field $B_{\text{app}} = 100 \mu\text{T}$ from two perspectives; (f,g) magnetization distributions computed from the measured field for (f) the entire sample and (g) a section of the sample. (Adapted from Ref. [138], with permission.)

10.3.3.2 Inverting the Dipole Field Equation for Diamagnetic and Paramagnetic Materials

The general inverse problem for magnetic media involves solving for the vector magnetization $\vec{M}(\vec{r}')$ in (10.3), or, after dividing by the applied field, the susceptibility $\chi(\vec{r}')$. This inverse problem has no unique solution. In the quasistatic limit, the curl of \vec{B} is zero in a current-free region, indicating that the field can be expressed as the gradient of the magnetic scalar potential V_m , where $\vec{B} = -\mu_0 \nabla V_m$. The magnetic potential outside of the surface S that bounds the sample of volume V is given by [133]

$$V_m(\vec{r}) = \frac{1}{4\pi} \int_S \frac{\vec{M}(\vec{r}') \cdot \hat{n}}{|\vec{r} - \vec{r}'|} d^2 r' + \frac{1}{4\pi} \int_V \frac{\nabla' \cdot \vec{M}(\vec{r}')}{|\vec{r} - \vec{r}'|} d^3 r'. \quad (10.200)$$

Hence, we see that measurements of quasistatic magnetic fields in free space outside a magnetized body provide information about the divergence of the magnetization distribution, rather than the magnetization itself, just as measurements of the magnetic field outside of a current distribution provide information only about the curl of the currents ((10.15)). Thus, any magnetization distribution that is divergence-free will be magnetically silent and cannot affect the external magnetic field. Beardsley [134] points out that in special cases, such as in a film with a magnetization that does not vary with thickness, the combined measurement of the external magnetic field and the angular deflection of an electron beam passing through the sample (differential phase contrast Lorentz microscopy) can provide the requisite information required to determine unambiguously the magnetization within the film. In this chapter, we restrict ourselves to SQUID measurements alone, and hence are faced, once again, with a potentially unsolvable inverse problem.

For magnetically soft materials, the magnetization is provided by external magnetic fields, and hence divergence-free magnetizations are avoided. This provides an important constraint to the problem. If we apply only a uniform H_z field, and if we know that for our sample $\vec{M}(\vec{r}') = \chi \vec{H}(\vec{r}')$, we need to solve for the scalar magnetization $M_z(\vec{r}')$ in the slightly simpler equation

$$\vec{B}(\vec{r}) = \frac{\mu_0}{4\pi} \int_V \left\{ \frac{3M_z(\vec{r}') (z - z')}{|\vec{r} - \vec{r}'|^5} (\vec{r} - \vec{r}') - \frac{M_z(\vec{r}') \hat{z}}{|\vec{r} - \vec{r}'|^3} \right\} d^3 r'. \quad (10.201)$$

In two dimensions, there is a unique inverse solution to this problem, to be presented in the next section. After that discussion, we shall show that in three dimensions, however, there is still a problem with nonuniqueness.

10.3.3.3 Two-Dimensional Magnetization Imaging

For two-dimensional samples, we can apply our inverse spatial filtering approach to determine the magnetization or susceptibility distributions from the magnetic field [78, 135, 136]. If the source is restricted to two dimensions, such as a thin sheet of diamagnetic or paramagnetic material, (10.201) reduces to a two-dimensional surface integral. We shall for now assume that we are applying only a z -component field $H_0\hat{z}$, and are measuring only the z -component of the sample-induced magnetic field \vec{B} at a height $(z - z')$ above the two-dimensional sample of infinite extent, so that we have

$$B_z(\vec{r}) = \frac{\mu_0}{4\pi} \int_{x'=-\infty}^{\infty} \int_{y'=-\infty}^{\infty} \left\{ \frac{3M_z(\vec{r}') (z - z')^2}{|\vec{r} - \vec{r}'|^5} - \frac{M_z(\vec{r}')}{|\vec{r} - \vec{r}'|^3} \right\} dx' dy'. \quad (10.202)$$

In practice, the integrals need not extend beyond the boundary of the source object, outside of which $\vec{M} \equiv \vec{0}$. In order to solve this equation for $\vec{M}_z(\vec{r}')$, we define a Green's function

$$G_z(\vec{r} - \vec{r}') = \frac{\mu_0}{4\pi} \left\{ \frac{3(z - z')^2}{|\vec{r} - \vec{r}'|^5} - \frac{1}{|\vec{r} - \vec{r}'|^3} \right\}, \quad (10.203)$$

so that (10.202) becomes

$$B_z(\vec{r}) = \int_{-\infty}^{\infty} \int_{-\infty}^{\infty} M_z(\vec{r}') G_z(\vec{r} - \vec{r}') dx' dy'. \quad (10.204)$$

We compute the two-dimensional spatial Fourier transform of the magnetic field

$$b_z(k_x, k_y, z) = FT\{B_z(x, y, z)\}, \quad (10.205)$$

so that we can use the convolution theorem to express (10.202) in the spatial frequency domain as

$$b_z(k_x, k_y, z) = g_z(k_x, k_y, z - z') m_z(k_x, k_y), \quad (10.206)$$

where $g_z(k_x, k_y, z - z')$ is the two-dimensional spatial Fourier transform of the Green's function, *i.e.*,

$$g_z(k_x, k_y, z - z') = \frac{\mu_0}{4\pi} \left\{ 2\pi k e^{-k(z-z')} \right\}, \quad (10.207)$$

with

$$k = (k_x^2 + k_y^2)^{\frac{1}{2}} \quad (10.208)$$

and $m_z(k_x, k_y)$ is the Fourier transform of the magnetization $M_z(x, y)$. The inverse problem then reduces to a division in the spatial frequency domain

$$m_z(k_x, k_y) = \frac{b_z(k_x, k_y, z)}{g_z(k_x, k_y, z - z')}. \quad (10.209)$$

As we have seen before, it may be necessary to use windowing techniques to prevent this equation from “blowing up” because of zeros in the Green’s function occurring at spatial frequencies for which there is a contribution to the magnetic field from either the sample or from noise. Typically, the window $w(k_x, k_y)$ is a low-pass filter which attenuates high-frequency noise in the vicinity of the zeros of g_z , so that (10.209) becomes

$$m_y(k_x, k_y) = \frac{b_z(k_x, k_y, z)}{g_z(k_x, k_y, z - z')} w(k_x, k_y). \quad (10.210)$$

As the final step, we use the inverse Fourier Transform (FT^{-1}) to obtain an image of the magnetization distribution

$$M_z(x, y) = FT^{-1}\{m_z(k_x, k_y)\}, \quad (10.211)$$

which can then be used to obtain the desired susceptibility image

$$\chi(x, y) = \frac{M_z(x, y)}{H_0(\vec{r})}. \quad (10.212)$$

This outlines the basic approach to two-dimensional magnetic susceptibility imaging; many of the techniques demonstrated for current-density imaging also will be applicable. It is important to note that once the Green’s function (and its inverse) and the window have been specified, it also is possible to proceed directly from $B_z(x, y)$ to $\chi(x, y)$ by evaluating the appropriate convolution integral in xy -space. Applications of this technique include localizing dilute paramagnetic tracers [137] and the imaging of plastic [138] (as shown in Figure 10.37), rock [8, 139, 140], and even water [141].

10.3.3.4 Magnetic Susceptibility Tomography

If the source is three-dimensional, a somewhat more general approach must be taken. We can start with (10.1), the dipole field equation for the magnetic field

$d\vec{B}(\vec{r})$ produced by a single magnetic dipole $d\vec{m}(\vec{r}')$. If the dipole moment arises from the magnetization of an incremental volume dv in an applied field $\vec{H}(\vec{r}')$, we have that

$$d\vec{m}(\vec{r}') = \chi(\vec{r}') \vec{H}(\vec{r}') dv'. \quad (10.213)$$

The dipole field equation then becomes

$$d\vec{B}(\vec{r}) = \frac{\mu_0 \chi(\vec{r}')}{4\pi} \left\{ \frac{3\vec{H}(\vec{r}') \cdot (\vec{r} - \vec{r}')}{|\vec{r} - \vec{r}'|^5} (\vec{r} - \vec{r}') - \frac{\vec{H}(\vec{r}')}{|\vec{r} - \vec{r}'|^3} \right\} dv'. \quad (10.214)$$

This equation can be written as

$$d\vec{B}(\vec{r}) = \vec{G}(\vec{r}, \vec{r}', \vec{H}) \chi(\vec{r}') dv', \quad (10.215)$$

where we introduce a vector Green's function

$$\vec{G}(\vec{r}, \vec{r}', \vec{H}) = \frac{\mu_0}{4\pi} \left\{ \frac{3\vec{H}(\vec{r}') \cdot (\vec{r} - \vec{r}')}{|\vec{r} - \vec{r}'|^5} (\vec{r} - \vec{r}') - \frac{\vec{H}(\vec{r}')}{|\vec{r} - \vec{r}'|^3} \right\}. \quad (10.216)$$

The components of \vec{G} are simply

$$\vec{G} = G_x \hat{x} + G_y \hat{y} + G_z \hat{z}, \quad (10.217)$$

where

$$G_x(\vec{r}, \vec{r}', \vec{H}) = \frac{\mu_0}{4\pi} \left\{ \frac{3\vec{H} \cdot (\vec{r} - \vec{r}')}{|\vec{r} - \vec{r}'|^5} (x - x') - \frac{H_x}{|\vec{r} - \vec{r}'|^3} \right\}, \quad (10.218)$$

$$G_y(\vec{r}, \vec{r}', \vec{H}) = \frac{\mu_0}{4\pi} \left\{ \frac{3\vec{H} \cdot (\vec{r} - \vec{r}')}{|\vec{r} - \vec{r}'|^5} (y - y') - \frac{H_y}{|\vec{r} - \vec{r}'|^3} \right\}, \quad (10.219)$$

$$G_z(\vec{r}, \vec{r}', \vec{H}) = \frac{\mu_0}{4\pi} \left\{ \frac{3\vec{H} \cdot (\vec{r} - \vec{r}')}{|\vec{r} - \vec{r}'|^5} (z - z') - \frac{H_z}{|\vec{r} - \vec{r}'|^3} \right\}. \quad (10.220)$$

The three components of the magnetic field in (10.215) now can be written as

$$dB_x(\vec{r}) = \chi(\vec{r}') G_x(\vec{r}, \vec{r}', \vec{H}), \quad (10.221)$$

$$dB_y(\vec{r}) = \chi(\vec{r}') G_y(\vec{r}, \vec{r}', \vec{H}), \quad (10.222)$$

$$dB_z(\vec{r}) = \chi(\vec{r}') G_z(\vec{r}, \vec{r}', \vec{H}). \quad (10.223)$$

Note that \vec{H} may in turn be a function of x' , y' , and z' . In contrast, the Green's function in (10.203) does not contain \vec{H} . However, \vec{H} is assumed to be known and only adds a geometrically variable scale factor into the Green's function. The increased complexity of (10.218) through (10.220) arises from our desire to include \vec{H} as a vector field with three independently specified components.

If we know both the location \vec{r}' of a source that is only a single dipole, and also the strength and direction of \vec{H} at that point, we can make a single measurement of the magnetic field at \vec{r} to determine $\chi(\vec{r}')$. It is adequate to measure only a single component of $\vec{B}(\vec{r})$ as long as that component is nonzero. The problem becomes somewhat more complex when there are either multiple dipoles or a continuous distribution of dipoles. In that case, we need to sum or integrate (10.215) over the entire source object

$$\vec{B}(\vec{r}) = \int_{x'} \int_{y'} \int_{z'} \vec{G}(\vec{r}, \vec{r}', \vec{H}) \chi(\vec{r}') dv' \quad (10.224)$$

To proceed numerically, we shall assume that we can discretize the source object into m elements of volume or voxels v_j , where $1 \leq j \leq m$. The field from this object is then

$$\vec{B}(\vec{r}) = \sum_{j=1}^m \vec{G}(\vec{r}, \vec{r}'_j, \vec{H}) \chi(\vec{r}'_j) v_j. \quad (10.225)$$

A single measurement of \vec{B} will be inadequate to determine the susceptibility values for the m elements. Thus, we must make our measurements at n measurement points \vec{r}_i , where $1 \leq i \leq n$ identifies each such measurement. The three field components measured at a single point would constitute, in this notation, three independent scalar measurements which happen to have the same value for \vec{r} . Equation (10.225) becomes

$$\vec{B}_i(\vec{r}_i) = \sum_{j=1}^m \vec{G}(\vec{r}_i, \vec{r}'_j, \vec{H}) \chi(\vec{r}'_j) v_j. \quad (10.226)$$

To simplify the analysis, we can convert to matrix notation. In this case, the vector Green's function \vec{G} becomes an $n \times m$ matrix $\tilde{\vec{G}}$ that contains as each of its rows the Green's functions that relate a single measurement to every source element, *i.e.*, (10.221) – (10.223). The n field measurements can be written as the n elements of an $n \times 1$ column matrix \vec{B} . The magnetic susceptibility of each of the m

source elements can be described by an $m \times 1$ column matrix $\tilde{\chi}$. The volume of each source element can be incorporated into either the $\tilde{\mathbf{G}}$ or $\tilde{\chi}$ matrices. The measurements are related to the sources by

$$\tilde{\mathbf{B}} = \tilde{\mathbf{G}}\tilde{\chi}. \quad (10.227)$$

If $n = m$ the system of equations will be exactly determined, but it may not be possible to obtain a solution because of measurement noise or nonorthogonality, *i.e.*, linear dependence of the n equations. The alternative is to choose $n > m$, so that the system becomes overdetermined, and a least-squares solution can be attempted. Ideally, only those measurements needed to increase the independence of the equations will be added. While there are several ways to proceed, we shall consider only the general approach of multiplying both sides of (10.227) by $\tilde{\mathbf{G}}^T$, the transpose of $\tilde{\mathbf{G}}$, also known as the normal equations

$$\tilde{\mathbf{G}}^T \tilde{\mathbf{B}} = \tilde{\mathbf{G}}^T \tilde{\mathbf{G}} \tilde{\chi}. \quad (10.228)$$

The product $\tilde{\mathbf{G}}^T \tilde{\mathbf{G}}$ is now an $m \times m$ matrix that in principle can be inverted. This allows us to solve for $\tilde{\chi}$

$$\left[\tilde{\mathbf{G}}^T \tilde{\mathbf{G}} \right]^{-1} \tilde{\mathbf{G}}^T \tilde{\mathbf{B}} = \tilde{\chi}. \quad (10.229)$$

The ability to compute the inverse of the $\tilde{\mathbf{G}}^T \tilde{\mathbf{G}}$ matrix is determined by the measurement noise, by how well the measurements span the source space, and by the well-conditioning of the G matrix. Typically, if this inversion process is attempted for measurements made in a single plane over a complex source, the near elements of the source will dominate, and the matrix will be ill-conditioned.

Magnetic susceptibility tomography [142–147] can be used to avoid the ill-conditioned nature of (10.229) by applying the magnetic field from a number of different directions and by measuring the magnetic field at multiple locations all around the object. Since $n \gg m$, the system of equations becomes highly overdetermined, and standard techniques, such as singular value decomposition, can be used to determine the susceptibility of each voxel. Since the direction of the magnetization of each voxel of the material is known for every measurement, and this direction is varied, the domination of the $\tilde{\mathbf{G}}^T \tilde{\mathbf{G}}$ matrix by a small set of measurements can be avoided. The stability of the inversion of (10.229) can be enhanced by using nonuniform magnetizing fields [142]. The first demonstration of this technique, shown in Figure 10.38, used a uniform magnetizing field and a 64-voxel cube [145]. The reconstruction was reasonably accurate in the absence of noise, but the matrix was sufficiently ill-conditioned that stable inverse solutions were difficult to obtain with modest amounts of noise. The matrix will be more readily inverted if nonuniform magnetizing fields are utilized, since there are only three independent uniform fields that can be applied to an object [142–144],

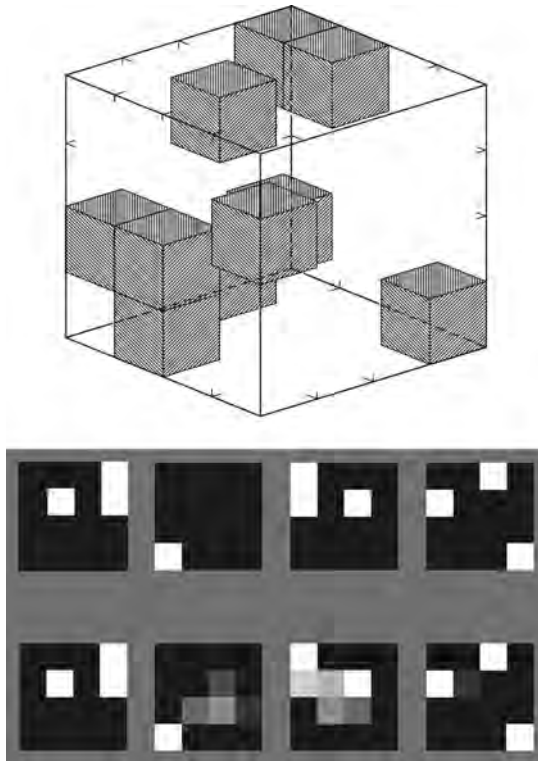


Fig. 10.38 Susceptibility tomography to reconstruct a simulated 64-element cube. Top: the ten shaded elements have a susceptibility of $+2.5 \times 10^{-5}$; all others have a susceptibility of $+2.0 \times 10^{-5}$. Bottom (upper): gray-scale representation of the actual susceptibility distribution; bottom (lower): the

distribution determined by a simulated susceptibility tomography measurement using a fixed magnetizing field and maps of the normal component of the perturbation field over the six faces of the cube. (Adapted from Ref. [145], with permission.)

and since a nonuniform magnetizing field eliminates the uncertainty of equivalent spherical sources with identical dipole moments.¹¹⁾

11) Suppose that we consider two uniformly magnetized spheres, centered at the origin, that have different radii but with magnetizations that are scaled such that the two spheres have the same magnetic dipole moment. Because the magnetic field outside of a uniformly magnetized sphere is perfectly dipolar, it is impossible to distinguish between these two sources by means of magnetic measurements made beyond the radius of the larger sphere. The existence of two different source distributions with identical fields in the region outside of all possi-

ble sources is the death knell for the inverse problem: without additional constraints, an inverse algorithm will be unable to control the degree of freedom within the source that corresponds to the radius of a uniformly magnetized sphere whose susceptibility scales inversely with the sphere volume. A multipole analysis of the external fields can give the dipole moment of the source to an arbitrary accuracy, but cannot determine both the radius of a uniformly magnetized sphere and its susceptibility if they are scaled for a constant dipole moment.

Two- and three-dimensional magnetic susceptibility imaging offers potential advantages for imaging magnetically labeled flaws or composites impregnated with dilute magnetic tracers [137, 148, 149], for magnetic imaging of materials such as plastic, titanium, or aluminum that are normally considered nonmagnetic, monitoring macrophage activity [150, 151], and, with susceptibility tomography, three-dimensional magnetic images of metabolism and iron storage in the liver and possibly regional oxygenation of the brain. In particular, while magnetic resonance imaging (MRI) is highly sensitive to spatial variations in magnetic susceptibility [152–155], the calibration of MRI susceptibility measurements for iron storage or other measurements of susceptibility effects in the body remains elusive, and hence SQUID susceptometry remains the gold standard [156–158]. However, additional improvements to both SQUID instruments and algorithms [142–144, 159] will be required before magnetic susceptibility tomography can compete with the more conventional, nonimaging methods for SQUID measurements of biosusceptibilities. Ongoing work in MRI inverse models and measurement protocols may eventually provide a noninvasive means for measuring biosusceptibility distributions in humans [160].

10.3.4

The Inverse Problem and Silent Sources

10.3.4.1 Introduction

In the preceding sections, we presented a wide variety of techniques for addressing the magnetic inverse problem. The lack of a unique solution to the magnetic or electric inverse problems is a general issue that applies to either field alone. However, in biomagnetism, the electric sources produce both electric and magnetic fields. This coupling of the fields in turn leads to new complexities that we will now explore. Sections 10.3.4.2 and 10.3.4.4 draw extensively from Ref. [13].

10.3.4.2 The Helmholtz Decomposition

In Section 10.2.4.2, we saw that the electric potential in an infinite homogeneous conductor is determined solely by the divergence of the primary current, while the magnetic field is determined by its curl. This leads to an interesting, and somewhat controversial, observation about the primary current distribution. If $\vec{J}^i(\vec{r})$ is an arbitrary vector field, it can be represented by a Helmholtz decomposition [161]

$$\vec{J}^i(\vec{r}) = \vec{J}_F^i(\vec{r}) + \vec{J}_V^i(\vec{r}), \quad \text{where } \nabla \times \vec{J}_F^i(\vec{r}) = \vec{0} \text{ and } \nabla \cdot \vec{J}_V^i(\vec{r}) = 0. \quad (10.230)$$

Thus \vec{J}_F^i has no curl and is called a “flow field,” while \vec{J}_V^i has no divergence and is called a “vortex field.” In an infinite homogeneous conductor, represented by only the first terms in (10.35) and (10.36) (*i.e.*, $\vec{K}^i = \vec{0}$), the electric potential is thereby determined solely by the pattern of \vec{J}_F^i and the magnetic field only by the

pattern of \vec{J}_V^i ; if \vec{J}_F^i and \vec{J}_V^i are independent, then V and \vec{B} will likewise be independent. This observation has been the basis for the controversy regarding possible independent information in the MCG. As we will see, the answer to this controversy may lie in the clarification of either the physiological constraints on \vec{J}^i , since any constraint that prevents \vec{J}^i from being the most general form of vector field will also cause \vec{J}_F^i and \vec{J}_V^i to be related, or in the effects of inhomogeneities at the cellular level.

The question of constraints on \vec{J}^i can be addressed using a simple variable-counting argument [22]. If the primary current distribution is a general vector field, it will have three degrees of freedom. The Helmholtz decomposition is simply a statement that such a vector field can be described by a scalar potential with one degree of freedom (consistent with \vec{J}_F^i having no curl), and a vector potential with two degrees of freedom (consistent with \vec{J}_V^i having no divergence). As first pointed out by Rush [162], there are physiological constraints on \vec{J}^i that leave it with less than three degrees of freedom. As a result, the electric and magnetic fields cannot be completely independent.

The question of independence becomes more complicated in a conductor with boundaries or internal inhomogeneities. Then V is still determined solely by \vec{J}_F^i , but \vec{B} now receives contributions from both \vec{J}_V^i and \vec{J}_F^i through the appearance of V in the second term of the integrand in (10.36). The magnetic field contribution from \vec{J}_V^i may still contain independent information consistent with our preceding discussion, but the contribution associated with the inhomogeneities is determined by \vec{J}_F^i . This would provide a mixing of the information in the MCG and ECG, which could be particularly important in situations where the second term of the integrand in (10.36) dominates the first. At first glance the second term is governed by V , which is described by \vec{J}_F^i . However, the integration of \vec{K}^i in both equations incorporates the boundary geometry differently and the effect of the geometry on the relative information content of these two integrals is not yet understood. Using the variable counting approach, the secondary source contribution should contain at least two degrees of freedom, since V contains one and the boundary that specifies the orientation of the secondary sources will contain another. How these two or more degrees of freedom couple to the ECG and the MCG is in need of clarification.

The ideal way to demonstrate the independence (or dependence) of the two integrals on the boundary geometry would be to demonstrate (or to prove the nonexistence of) examples in which a particular boundary or internal inhomogeneity affects either the electric field or the magnetic field from a particular source but not both, *i.e.*, an inhomogeneity that would be silent to only one of the two fields. A simple example is a horizontal current dipole in a conducting half space beneath a horizontal boundary: the normal component of the magnetic field in the air above the boundary is not affected by the inhomogeneity but the electric field above is. Many theoretical and experimental studies have compared the effects of the geometry of macroscopic inhomogeneities on the MCG and ECG with the hope of determining which measurement is least sensitive to the boundary and most sensitive to the primary sources. The situation is reversed at the cel-

lular level, since the inhomogeneity of the membrane dominates both the electric and magnetic fields and the active currents within the membrane do not directly affect either field to an appreciable degree.

The realization that the ECG and MCG *might be* independent, *i.e.*, the MCG might contain new information not present in the ECG, led to an intense debate. Rush claimed that there was no new information in the MCG [162], Plonsey responded [163] by noting that the uniform double layer provided a physiological constraint that reduced $\vec{j}^i(\vec{r})$ to having a single degree of freedom. Wikswo *et al.* demonstrated that the uniform double layer model led to differing sensitivities of the ECG and MCG to both the configuration of the double-layer rim and the effect of boundaries in (10.35) and (10.36) [22]. As summarized by Gulrajani [164], the initial arguments then reduced to one of differential sensitivities. The issue of physiological constraints remained unaddressed [165].

10.3.4.3 Electrically Silent Sources

In 1982, Wikswo and Barach realized, based upon pioneering work by Corbin, Scherr, and Roberts [166–168], that the anisotropy of cardiac tissue could create current sources that had a magnetically detectable but electrically silent component [14], as shown in Figure 10.39. These sources were then realized to be examples of a general class of sources, as illustrated in Figure 10.40, where the electric field reflects irrotational components of the source, and the magnetic field reflects both.

Plonsey and Barr then showed, in a ground-breaking pair of papers, that the cardiac bidomain should support circulating currents that could not be readily detected from measurements of the extracellular potential [169, 170]. An analytical examination of the role of tissue anisotropy demonstrated that the bidomain model had within it electrical anisotropies that might support currents that were electrically silent but magnetically detectable [15], and that much of the argument

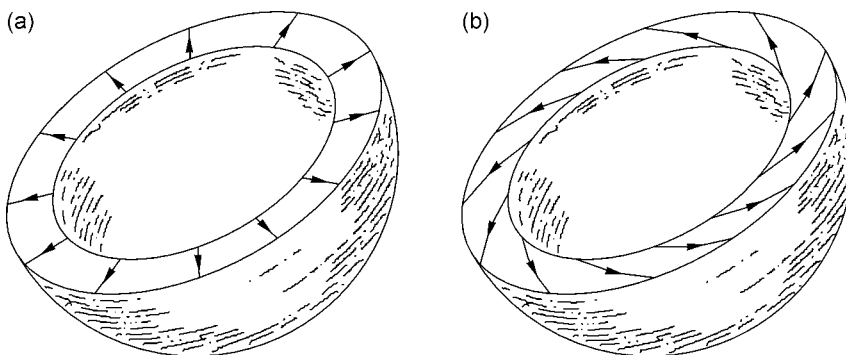


Fig. 10.39 Two models of the cardiac activation wave front: (a) a uniform double-layer model of cardiac activation; (b) another double-layer model of cardiac activation that would be electrically identical to that in (a) but magnetically different. (Adapted from Ref. [14], with permission.)

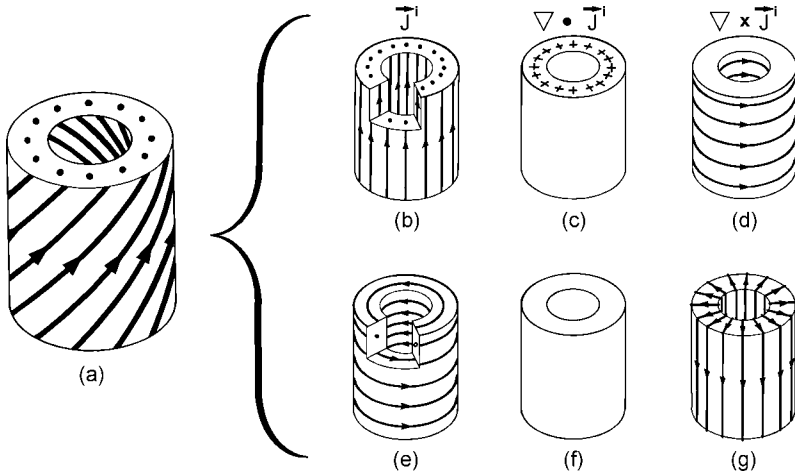


Fig. 10.40 (a) A general, hypothetical impressed current distribution in a tubular region of biologically active tissue; (b) the impressed currents J^i are uniformly distributed in the z direction and have the divergence and curl shown in (c) and (d). The J^i in (e) are tangential and have curl, as in (g), but no

divergence, as in (f). The cut-outs are to show that the impressed current is distributed throughout the wall of the tube, while the curls and divergences are nonzero only on surfaces. (Adapted from Ref. [14], with permission.)

reduced to one of off-diagonal terms in the two anisotropy tensors that were required to describe cardiac tissue. The question of whether or not these toy models would survive in realistic geometries was assessed by a modeling study of the magnetic field that would be recorded at the ventricular apex [171], as shown in Figure 10.41.

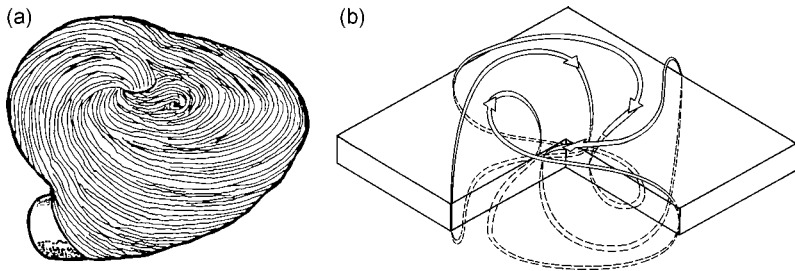


Fig. 10.41 The effects of spiral tissue architecture at the cardiac apex: (a) the fiber orientation at the apex (adapted from Ref. [245], with permission); (b) the apical magnetic field predicted for a bidomain model of a planar slab of tissue with spiral tissue architecture having a circularly symmetric cylindrical

wave front propagating outwards from the center. The field pattern is quite different from that produced by expanding wave fronts in tissue with parallel fibers, shown in Figs. 10.7 and 10.39. (Adapted from Ref. [171], with permission.)

From the perspective of the inverse problem, the issue then reduces to whether the appropriate model fitted to magnetic and electric data could distinguish between these two types of cardiac sources, *i.e.*, use the MCG to detect the effects of spiral anisotropy that could not be discerned from the ECG [70]. To date, there have yet to be incontrovertible demonstrations of new information in the human MCG, although magnetic fields recorded from the surface of an isolated rabbit heart during stimulation and propagation of action potentials clearly support the bidomain model and its representation of the magnetic field [65, 172–175].

10.3.4.4 Multipole Expansions

The relation of the electric and magnetic fields of current sources is also present in multipole expansions, as evidenced by the gray and black arrows representing dipole models in Figure 10.6. Both sets of current dipoles in the quadrupole expansion produce, in the appropriate limit, indistinguishable electric fields, but different magnetic fields. In the simple multipole expansions discussed in Ref. [18], there is in fact a series of electrically silent multipole terms. To better demonstrate this point, we analyze the current multipole expansions for the electric potential and magnetic field, such as the ones derived by Katila and Karp [176]. These authors emphasized that the leading term of each expansion has the current dipole as its source, and therefore to first order the two measures of cardiac activity yield identical information. Independently we have noted that the next term of the expansion has the current quadrupole coefficients a_{ij} appearing as the source, but different combinations of a_{ij} enter the expression for $V(\vec{r})$ than for $\vec{B}(\vec{r})$. In particular, the field depends on asymmetric terms of the quadrupole tensor that do not contribute to the potential. We shall briefly elaborate on this point of view.

The a_{ij} represent particular integrals of each Cartesian component of the current density [176]

$$a_{ij} = \int r'_i J'_j(\vec{r}') dv', \quad (10.231)$$

where both indexes i and j stand for any of the three axes x , y , and z , leading to nine possible combinations. The set of quadrupole terms can be arrayed in a matrix denoted by the symbol $\tilde{\mathbf{A}}$

$$\tilde{\mathbf{A}} = \begin{bmatrix} a_{xx} & a_{xy} & a_{xz} \\ a_{yx} & a_{yy} & a_{yz} \\ a_{zx} & a_{zy} & a_{zz} \end{bmatrix}. \quad (10.232)$$

Each of the terms can be represented by a pair of opposing dipoles placed side-by-side or in a line, with an appropriate distance of separation. The terms of the quadrupole tensor of (10.232) can thus be displayed pictorially as in Figure 10.42(a). This tensor at first glance appears to have nine independent terms.

However, the sum of a_{xx} , a_{yy} , and a_{zz} , known as the “trace” of the tensor, must be set equal to zero, because this sum must be electrically silent, *i.e.*, the electric potential outside this combined source would be zero everywhere, and the sum of a_{xx} , a_{yy} , and a_{zz} would otherwise be indeterminate. Because of this constraint, there are only eight independent terms in the tensor. While the act of setting the trace to zero will also modify the pictures in Figure 10.42(a) [177], we shall not do this so as to simplify the discussion.

We can write $\tilde{\mathbf{A}}$ as the sum of symmetric and antisymmetric tensors

$$\tilde{\mathbf{A}} = \tilde{\mathbf{A}}^s + \tilde{\mathbf{A}}^a, \quad (10.233)$$

where $\tilde{\mathbf{A}}^s$ and $\tilde{\mathbf{A}}^a$ are given by combining $\tilde{\mathbf{A}}$ with its mathematical transpose, indicated by $\tilde{\mathbf{A}}^T$

$$\begin{aligned} \tilde{\mathbf{A}}^s &= \frac{1}{2}(\tilde{\mathbf{A}} + \tilde{\mathbf{A}}^T) \\ \tilde{\mathbf{A}}^a &= \frac{1}{2}(\tilde{\mathbf{A}} - \tilde{\mathbf{A}}^T). \end{aligned} \quad (10.234)$$

The pictorial representation of $\tilde{\mathbf{A}}$ and $\tilde{\mathbf{A}}^T$ is shown in Figures 10.42(b) and (c), respectively. The symmetric tensor $\tilde{\mathbf{A}}^s$ contains combinations of a_{ij} that appear in the current multipole expansion for the electrical potential distribution from a primary current source. It contains five independent terms, when we take account of the constraint that the trace must be zero. The antisymmetric tensor $\tilde{\mathbf{A}}^a$ contains three independent terms, since the three terms in the lower left corner of Figure 10.42(c) are simply the negative of the respective three terms in the upper right corner across the diagonal. We also see that these three terms in the current quadrupole tensor represent current loops (magnetic dipoles) oriented normal to the three axes of the Cartesian coordinate system. Each is electrically “silent,” so it is apparent that these three terms can be determined only by magnetic measurements and not by electric ones. One advantage of analyzing a field pattern with the current multipole expansion, as opposed to the magnetic multipole expansion, is that it allows extraction of the maximal information from the magnetic field while also providing equivalent primary current generators that can be readily interpreted in terms of various physiological current source distributions.

More sophisticated vector expansions of the source can also be obtained, which contain electric-like and magnetic-like terms. The electric field depends only on the former, whereas the magnetic field depends on both [165].

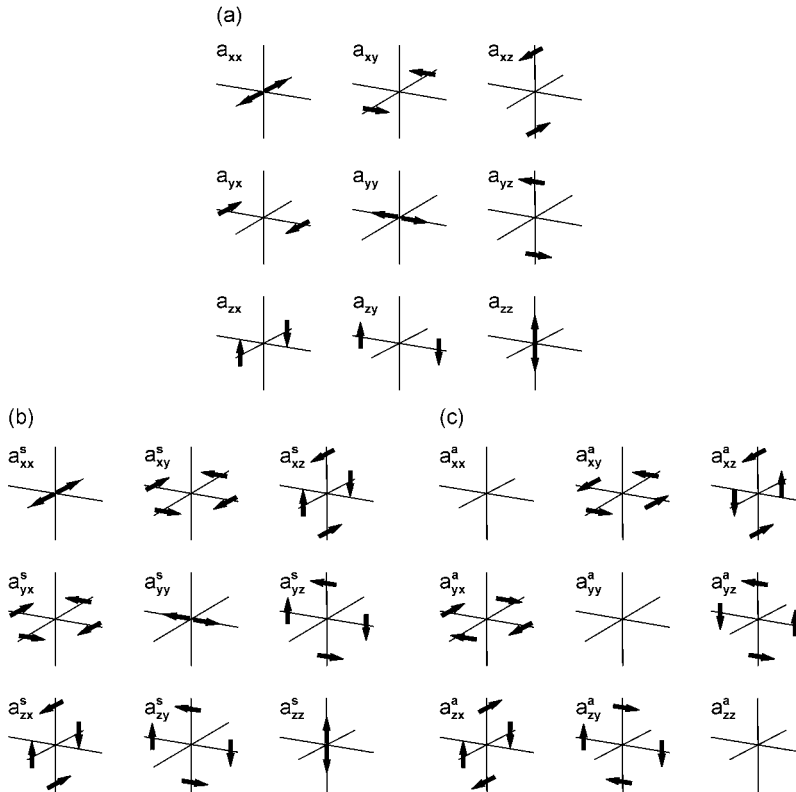


Fig. 10.42 Pictorial representation of the current quadrupole tensor: (a) the complete tensor; (b) symmetric part of the tensor; (c) antisymmetric part of the tensor. (Adapted from Ref. [13], with permission.)

10.3.4.5 Multiple Dipole Models

We presented Figure 10.8 in the context of the forward model of computing the cardiac magnetic field from a distributed dipole model of the cardiac activation wave front. From the point of view of the inverse model, this picture is dangerously deceptive. We demonstrate this by referring to the classic example by Holt *et al.* that demonstrated the limitations of multiple dipole models for inverse electrocardiography [38–40]. The effectiveness of various inverse algorithms that employ the multiple dipole model was investigated, among others, by Uutela *et al.* [178].

Least-Squares Fitting and the Generalized Inverse

We can now come full circle and reexamine the problems of fitting magnetic fields to a set of magnetic or electric dipoles. Earlier, we showed that the fields from a single dipole were given by (10.1) or (10.160). Following the convention we had in our discussion of magnetic susceptibility tomography, we can use matrix

notation to write the magnetic field as the product of a Green's function matrix and a source vector

$$\vec{B}(\vec{r}) = \sum_{j=1}^m \vec{G}(\vec{r}, \vec{r}_j) S(\vec{r}_j) v_j, \quad (10.235)$$

where $S(\vec{r}_j)$ is either an electric or magnetic dipole at point \vec{r}_j . This becomes

$$\vec{B} = \vec{G}\vec{S}. \quad (10.236)$$

As before, if $n = m$ the system of equations will be exactly determined, but it may not be possible to obtain a solution because of measurement noise, *i.e.*, linear dependence of the n rows of \vec{G} . The alternative is to choose $n > m$, so that the system becomes over-determined, and we can proceed with the least-squares generalized inverse solution

$$\vec{S} = [\vec{G}^T \vec{G}]^{-1} \vec{G}^T \vec{B}. \quad (10.237)$$

The ability to compute the inverse of the $\vec{G}^T \vec{G}$ matrix is determined by the measurement noise, by how well the measurements span the source space, and by the well-conditioning of the G matrix. It may be that $\vec{G}^T \vec{G}$ is sufficiently ill-conditioned or singular that its inverse cannot be computed, in which case one must resort to SVD or some other regularization technique to determine those contributions to $\vec{G}^T \vec{G}$ that can be determined by the measurement set. However, as we will now show, physiological constraints on the source distribution may produce computational problems far beyond what might be addressed with SVD. To show this, we will now examine the multiple-dipole model of the cardiac activation wave front as shown in Figure 10.8.

Multiple Dipoles and Cardiac Activation

As electrocardiography became more sophisticated and multiple recording leads became available, there was great interest in moving beyond the simple dipole model of the heart [179–181]. The obvious next step was to use two dipoles, one for each ventricle, and then multiple dipoles, such that the time dependence of a single dipole might reflect regional ischemia or infarction, and hence the inversion of Figure 10.8 comes to the fore. As discovered when first attempted by Holt *et al.* [38–40], there are instabilities in the solutions that correspond to the addition and subtraction of dipole representations of spherical capacitors. Perturbing one dipole can be balanced by a corresponding antiperturbation of all other dipoles. The obvious solution is to constrain the orientation of the dipole, through quadratic programming, so that their orientation cannot reverse. This corresponds to the addition of physiological constraints to a model, something that has been popular in MEG analyses of cortical sources. However, it must be remembered that at least in the uniform double-layer model of cardiac activation, any perturbation of the wave

front that does not affect the shape of the rim will not affect the external potentials, so physiological constraints such as *a priori* knowledge of wave front geometry will help, if at all, only as long as the actual geometry for the disease subject is close to what was assumed in creating the model. The situation is even more complicated when we consider the bidomain effects discussed above.

10.3.5

Three-Dimensional Inverse Algorithms

10.3.5.1 Introduction

In the cases presented up to this point, we generally considered only the simplest constraints with respect to whether an object is two- or three-dimensional, or whether we know where the current is injected and withdrawn, or what the boundary conditions are. For the MEG and to some extent the MCG, physiological information, obtained by MRI or other imaging modalities, can provide valuable information. One must be cautious, particularly when dealing with pathological conditions, that the data from a patient are not interpreted solely on the basis of a model designed for normal subjects. The question then reduces to one of deciding where best to place the uncertainties intrinsic to the magnetic inverse problem: stable solutions that specify diffuse effective sources, or highly localized models that may be overly simplistic. Undoubtedly, the best results will be obtained if the greatest amount of complementary information can be included in the analysis.

There are a number of three-dimensional inverse algorithms, such as beamformers, minimum norm techniques, the focal undetermined system solver, multiple signal classification, principal and independent component analysis, low-resolution electromagnetic tomography, magnetic field tomography, *etc.* (Some of those techniques have been reviewed in the context of magnetocardiography in Ref. [182].) The remainder of this section briefly reviews these important methods, which are further discussed in Chapter 11. It must be emphasized that none of these techniques can create new information beyond what is provided to the model. It should also be mentioned that the three-dimensional techniques discussed below can be applied in the context of both the current and magnetic dipole models, provided of course that appropriate modifications are made to accommodate the two formalisms.

10.3.5.2 Beamformers

Beamformers [183, 184] are spatial filters that were originally introduced in telecommunications [185] to provide an efficient method for the estimation of signals originating from a source located in a certain direction in the presence of noise and other signals. Their purpose is to spatially filter signals that have overlapping temporal frequencies but distinct sources. Historically, the term originates from the fact that early spatial filters were akin to pencil beams that preferentially allowed signals from a specific location to be received by a detector, while others

were attenuated [183]. The use of beamformers in biomagnetism was pioneered by van Veen, van Dronkelen et al. [183, 186], and Robinson and Vrba [187].

Through the use of multiple beamformers with different passbands, one can construct a neural power map that depicts neural power as a function of passband location [183]. Beamformer outputs are formed as weighted sums of sensor responses that specify spatial filtering features and increase sensitivity to signals from a preferred location. Strategies for determining the optimal set of weights lead to various distinct implementations of the beamformer method, including the linearly constrained minimum-variance (LCMV) [188] and nonlinearly constrained beamformers [187] used in synthetic aperture magnetometry (SAM). In the latter case, weights are computed for a unique orientation of the target source via a nonlinear optimization process that seeks to maximize the neural activity index, also known as the pseudo-Z statistic [189]. Various other adaptations of this method exist, including, for example, adaptive beamformers [190, 191].

10.3.5.3 Minimum Norm Techniques

Minimum norm techniques are optimal when minimal *a priori* information about the source is provided [192]. In this approach, the inverse problem is addressed using a combination of magnetometer lead fields to estimate the primary current distribution. As already explained in this chapter, one can write, in terms of the current dipole \vec{P} ,

$$B_i(\vec{r}') = \vec{L}_i(\vec{r}') \cdot \vec{P},$$

where B_i is the field component parallel to \vec{L}_i measured at location i of the magnetometer coil, and \vec{L}_i is the lead field associated with that location. Primary current distributions can be considered as elements of a so-called current space F that includes all square-integrable current distributions whose locations are limited to the conductor V . Since the field measurements B_i only convey information about a subspace F' of F , it follows that this subspace is spanned by the lead fields. One can define the inner product of two currents \vec{J}_1 and \vec{J}_2 in F as

$$\langle \vec{J}_1, \vec{J}_2 \rangle = \int_V \vec{J}_1(\vec{r}) \cdot \vec{J}_2(\vec{r}) d^3r \quad (10.238)$$

with norm

$$\|\vec{J}_k\|^2 = \int_V |\vec{J}_k(\vec{r})|^2 d^3r \quad (10.239)$$

The basic idea of the minimum norm technique is to identify an estimate J^* that is a linear combination of lead fields

$$\vec{J}^* = \sum_{j=1}^M w_j \vec{L}_j, \quad (10.240)$$

where w_j are real coefficients. Such an estimate must be confined to F' and must also reproduce the measured signals B_i . The process described above can be carried out by solving the set of linear equations

$$\vec{b} = \tilde{\mathbf{F}} \vec{w}, \quad (10.241)$$

where

$$\vec{b} = (B_1, \dots, B_m)^T \quad (10.242)$$

is the set of measured data,

$$\vec{w} = (w_1, \dots, w_m)^T \quad (10.243)$$

is the set of lead field coefficients to be found, and $\tilde{\mathbf{F}}$ is an $m \times m$ matrix with entries that are lead field inner products of the form

$$F_{ij} = \langle \vec{L}_i, \vec{L}_j \rangle \quad (10.244)$$

Solutions to this set of equations are not unique because any current \vec{J}_\perp satisfying the equality $\langle \vec{J}_\perp, \vec{L}_i \rangle = 0$ (i.e., perpendicular to the lead field \vec{L}_i) can be added to \vec{J}^* , yielding another solution to our set of equations. The physical meaning of this statement is that any current distribution that the magnetometer cannot detect can be added to the solution [192]. Mathematically, $\tilde{\mathbf{F}}$ is nonsingular if the lead fields are linearly independent. In practical situations, however, this is not the case: $\tilde{\mathbf{F}}$ can have very small eigenvalues, which leads to large errors in the calculation of the lead field coefficients w_j . In such cases, a regularization method can be applied, as discussed in a previous section of this chapter. Two minimum norm algorithms worth mentioning are the L1 and L2 norms, where L1 is characterized by a limited number of focused sources, while L2 (also known as minimum norm least squares or MNLS) is associated with a broad distribution of many sources [193].

The value and effectiveness of classic minimum norm techniques has been recognized in the EEG and MEG community particularly in cases where *a priori* source information is not available and/or very noisy data are analyzed. It has been shown that, although these methods are generally unable to accurately retrieve the depth of sources, they are quite effective at reconstructing two-dimensional projections of current distributions [192, 194–196].

10.3.5.4 FOCUSS

The FOCal Undetermined System Solver (FOCUSS) algorithm [197, 198] is a tomographic reconstruction method that aims to tame the major problem associated with typical minimum norm techniques: the lack of spatial resolution resulting in diffuse solutions, especially for deeper sources. In this method, a dipole is assigned to each voxel of the reconstruction volume, meaning that the nonlinear position parameters are completely specified. The Cartesian components of the dipole moments are thus the only unknowns to be estimated, and they are linearly related to the measurements. Provided that we make a sufficiently fine sampling of the volume relative to the spatial smoothness of the source distribution, the accuracy of the method is limited mainly by noise and other modeling errors. In some applications, such as MEG, it may be advantageous to use spherical coordinates and to recover only the two orthogonal vector components of the moment tangential to the radius of the sphere. In this way, we avoid the ill-posedness associated with radially oriented currents in the head, which cannot be observed with external field measurements, as discussed previously. For time-varying fields, reconstructions are calculated for each time slice.

The major strength of the FOCUSS algorithm lies in the reconstruction of localized sources. Unlike minimum norm estimates, which tend to produce many nonzero dipoles corresponding to a dispersion of the sources over a large volume, FOCUSS only selects a small number of elements that can generate the observed field.

We can express the system of linear equations in matrix form. Assuming a Cartesian coordinate system and numbering the dipole components sequentially, we have

$$\tilde{\mathbf{b}} = \tilde{\mathbf{G}}\tilde{\mathbf{p}}, \quad (10.245)$$

or

$$\begin{bmatrix} b_1 \\ \vdots \\ b_m \end{bmatrix} = [G_{1,x} \ G_{1,y} \ G_{1,z} \ G_{2,x} \ G_{2,y} \ \dots \ G_{n/3,z}] \begin{bmatrix} p_1 \\ \vdots \\ p_n \end{bmatrix} \quad (10.246)$$

where $\tilde{\mathbf{b}}$ is an $m \times 1$ vector containing m measurements of a magnetic field component, $\tilde{\mathbf{G}}$ is the $m \times n$ basis matrix or Green's function matrix, whose elements are determined by the model geometry, and $\tilde{\mathbf{p}}$ is an $n \times 1$ vector containing the n unknown components of $n/3$ dipoles. Since $\tilde{\mathbf{G}}$ depends solely on the geometry of the sources and sensors, it needs to be calculated only once for a particular configuration, allowing for realistic, complex, and detailed modeling.

In essence, the algorithm starts with a distributed estimate, which can be obtained, for example, by the minimum norm method. Then, FOCUSS recursively enhances some of the sources while attenuating the rest of the elements until they become zero. Only a small number of dipoles is therefore selected,

yielding a localized energy solution. Specifically, at each iteration of the algorithm, a solution is obtained by means of the weighted minimum norm

$$\tilde{\mathbf{p}} = \tilde{\mathbf{W}} \left(\tilde{\mathbf{G}} \tilde{\mathbf{W}} \right)^+ \tilde{\mathbf{b}} = \tilde{\mathbf{W}} \tilde{\mathbf{W}}^T \tilde{\mathbf{G}}^T \left(\tilde{\mathbf{G}} \tilde{\mathbf{W}} \tilde{\mathbf{W}}^T \tilde{\mathbf{G}}^T \right)^{-1} \tilde{\mathbf{b}}, \quad (10.247)$$

where $^+$ stands for the Moore–Penrose inverse, or pseudo-inverse, of a matrix and $\tilde{\mathbf{W}}$ is an $n \times n$ weighting matrix comprised of dimensionless scaling factors, whose purpose is to enhance some of the elements in $\tilde{\mathbf{p}}$. At each step, only $\tilde{\mathbf{W}}$ is changed, leading to a new (partial) solution.

Different definitions of $\tilde{\mathbf{W}}$ are possible, but a common choice is to make it a diagonal matrix whose elements are the elements of $\tilde{\mathbf{p}}$ obtained in the previous iteration. Another choice, which proves to be more robust, consists of defining $\tilde{\mathbf{W}}$ as the compound product of the weighting matrices obtained in the preceding steps. FOCUSS stops when the solution $\tilde{\mathbf{p}}$ no longer changes, and it has been shown that the algorithm always converges to a localized solution with no more than m nonzero elements [198].

Since FOCUSS is an initialization-dependent algorithm, care should be taken in calculating this particular step. An unbiased minimum norm solution, which compensates for the bias associated with the magnetic field falloff, may be used to provide an initialization within proximity of the true sources. In addition, in many applications, the matrix $\tilde{\mathbf{G}}$ is ill-conditioned, thereby requiring the use of some regularization technique to achieve a compromise between stability and a close fit to the data. Truncated SVD, where singular values below a certain threshold are discarded, may be used to address this problem.

10.3.5.5 MUSIC

The MUSIC algorithm was first proposed by Schmidt [199] to address the processing of signals from sensors with arbitrary locations and directional characteristics. It was then applied to biomagnetism by Mosher and co-workers [200, 201]; in our description of this method, we rely heavily on their work. Because our discussion is nevertheless introductory in nature, we refer the reader to the original literature [199, 200] for a detailed description of the method.

Let the $m \times n$ matrix $\tilde{\mathbf{F}}$ contain the spatiotemporal data for n time samples and m SQUID magnetometer channels. One can define an $m \times r$ “hybrid” gain matrix $\tilde{\mathbf{H}}$ that represents some mix of rotating or fixed dipoles in a noisy data model; the rank of $\tilde{\mathbf{H}}$ is equal to $R = 2p_R + p_F$, where p_R and p_F represent the number of rotating and fixed dipoles, respectively, for a total number of p dipoles. $\tilde{\mathbf{H}}$ contains the $3p$ unknown location parameters of these dipoles as well as the corresponding p_F unknown constraint moment parameters.

The matrix equation for this model assumes the form

$$\tilde{\mathbf{F}} = \tilde{\mathbf{H}} \tilde{\mathbf{S}} + \tilde{\mathbf{N}}, \quad (10.248)$$

where $\tilde{\mathbf{F}}$ contains the magnetometer data, $\tilde{\mathbf{S}}$ is a scalar time series matrix, and $\tilde{\mathbf{N}}$ represents the error between the measurements and our model; dimensionally, $\tilde{\mathbf{S}}$ is $r \times n$. In MUSIC, $\tilde{\mathbf{H}}$ is assumed to be of full column rank r for p dipoles. Let $\tilde{\mathbf{R}}_F$ denote a square symmetric matrix representing the spatial autocorrelation of the data, which can be computed using

$$\tilde{\mathbf{R}}_F = E\{\tilde{\mathbf{F}}\tilde{\mathbf{F}}^T\}, \quad (10.249)$$

where $E\{\cdot\}$ is the expectation operator. Then $\tilde{\mathbf{R}}_F$ can be written in terms of its eigendecomposition

$$\tilde{\mathbf{R}}_F = \tilde{\mathbf{\Phi}}\tilde{\mathbf{\Lambda}}\tilde{\mathbf{\Phi}}^T = \begin{bmatrix} \tilde{\mathbf{\Phi}}_s & \tilde{\mathbf{\Phi}}_n \end{bmatrix} \begin{bmatrix} \tilde{\mathbf{\Lambda}}_s & \\ & \tilde{\mathbf{\Lambda}}_n \end{bmatrix} \begin{bmatrix} \tilde{\mathbf{\Phi}}_s & \tilde{\mathbf{\Phi}}_n \end{bmatrix}^T, \quad (10.250)$$

where $\tilde{\mathbf{\Lambda}}_s$ is a diagonal matrix containing the largest R eigenvalues, while $\tilde{\mathbf{\Phi}}_s$ contains the corresponding eigenvectors. One assumption of the MUSIC algorithm is that the additive noise in the data is white and that it has a temporal and spatial mean of zero; this condition can be used to show that $\tilde{\mathbf{\Lambda}}_n = \sigma^2 \mathbf{I}$, where σ is the noise variance [200]. This variance is also equal to an eigenvalue λ with multiplicity $m-r$, which can be used to show that $\tilde{\mathbf{\Phi}}_n$ contains the remaining $m-r$ eigenvalues. The MUSIC algorithm computes the eigendecomposition

$$\hat{\tilde{\mathbf{R}}}_F = \frac{1}{N} \tilde{\mathbf{F}}\tilde{\mathbf{F}}^T = \hat{\tilde{\mathbf{\Phi}}}\hat{\tilde{\mathbf{\Lambda}}}\hat{\tilde{\mathbf{\Phi}}}^T, \quad (10.251)$$

where $\hat{\tilde{\mathbf{R}}}_F$ is the data estimate of $\tilde{\mathbf{R}}_F$ (the caret throughout this section refers to data estimate matrices of statistical quantities). The algorithm then orders the eigenvalues $\lambda_1, \dots, \lambda_m$ thus computed in descending order of their magnitude and finds a separation point D between the signal and noise subspace eigenvalues (where $1 \leq D < m$) based on the criterion that a distinct drop in eigenvalue magnitude occurs between λ_D and λ_{D+1} (see also Ref. [202] on alternative criteria for selecting the separation point). Next, the $m \times 2$ gain matrix $\tilde{\mathbf{G}}_i$ is computed over a fine grid of three-dimensional locations. For each entry in this matrix, the principal left eigenvectors $\tilde{\mathbf{U}}_{G_i}$ of $\tilde{\mathbf{G}}_i$ are computed using an SVD of the form

$$\tilde{\mathbf{G}}_i = \tilde{\mathbf{U}}_{G_i} \tilde{\mathbf{\Sigma}}_{G_i} \tilde{\mathbf{V}}_{G_i}^T. \quad (10.252)$$

This in turn allows one to compute

$$J_h(i) = \lambda_{\min} \left\{ \tilde{\mathbf{U}}_{G_i}^T \hat{\tilde{\mathbf{\Phi}}}_n^T \hat{\tilde{\mathbf{\Phi}}}_n \tilde{\mathbf{U}}_{G_i} \right\}, \quad (10.253)$$

i.e., the minimum eigenvalue of the expression in brackets. If, at each minimum of J_h , the subspace of $\tilde{\mathbf{G}}_i$ is orthogonal to the noise subspace, then the dipole is rotating. An alternative way of determining this is by computing the cost function

$$J_r(i) = \frac{\left\| \tilde{\boldsymbol{\Phi}}_n^T \tilde{\mathbf{U}}_{G_i} \tilde{\boldsymbol{\Sigma}}_{G_i} \right\|_F^2}{\left\| \tilde{\boldsymbol{\Sigma}}_{G_i} \right\|_F^2}, \quad (10.254)$$

where the subscript F refers to the Frobenius norm;¹²⁾ in this case, a rotating dipole satisfies $J_h(i) \approx J_r(i) \approx 0$. If the location of the dipole is fixed ($J_h(i) \approx 0$, $J_r(i) \neq 0$), its orientation can be estimated by computing the eigenvector of λ_{\min} . The process described above is then repeated until p_R rotating dipoles and p_F fixed dipoles are found such that $R = 2p_R + p_F$. Refinement of the solution can be achieved by further application of the same algorithm on a finer local grid.

10.3.5.6 Principal and Independent Component Analysis

Another method related to MUSIC that has been used perhaps less successfully [203, 204] is the principal component analysis (PCA) algorithm. In this approach, the data matrix $\tilde{\mathbf{F}}$ is first decomposed using the SVD

$$\tilde{\mathbf{F}} = \tilde{\mathbf{U}} \tilde{\boldsymbol{\Sigma}} \tilde{\mathbf{V}}^T. \quad (10.255)$$

The columns of $\tilde{\mathbf{U}}$ contain information referring to the spatial distribution of principal components while those of $\tilde{\mathbf{V}}$ are the corresponding time functions. If one forms the matrix $\tilde{\boldsymbol{\Sigma}}'$ containing only the R principal singular terms, the i th dipole location and moment can be found from a least squares minimization of the quantity

$$\min_{\tilde{\mathbf{L}}_i, \tilde{\mathbf{Q}}_i} \left\| \tilde{\mathbf{G}}_i(\tilde{\mathbf{L}}_i) \tilde{\mathbf{Q}}_i - \tilde{\mathbf{U}} \tilde{\boldsymbol{\Sigma}}' \tilde{\mathbf{C}}_i \right\|_2^2, \quad (10.256)$$

where $\tilde{\mathbf{G}}_i(\tilde{\mathbf{L}}_i)$ is the usual gain matrix for a dipole at location $\tilde{\mathbf{L}}_i$ with components specified by $\tilde{\mathbf{Q}}_i$. Several methods exist for choosing the so-called rotation factors $\{C_{lm}\}$ [205, 206]; the error in the equation above can be written as [200]

$$J_{\text{PCA}}(i) = \left\| \tilde{\mathbf{U}} \tilde{\boldsymbol{\Sigma}}' \tilde{\mathbf{C}}_i - \tilde{\mathbf{G}}_i \tilde{\mathbf{Q}}_i \right\|_2^2 = \left\| \tilde{\mathbf{P}}_{G_i}^\perp \tilde{\mathbf{U}} \tilde{\boldsymbol{\Sigma}}' \tilde{\mathbf{C}}_i \right\|_2^2, \quad (10.257)$$

where $\tilde{\mathbf{P}}_{G_i}^\perp$ is the orthogonal projection for a unique dipole.

12) The Frobenius norm of an $m \times n$ matrix $\tilde{\mathbf{A}}$ is

$$\text{defined as } \left\| \tilde{\mathbf{A}} \right\|_F = \sqrt{\sum_{i=1}^m \sum_{j=1}^n |a_{ij}|^2}.$$

Independent component analysis (ICA) is an extension of PCA that was developed in relation to the blind source separation (BSS) problem, where ICA is very common [207, 208]. Several ICA algorithms exist, such as SOBI [209], Infomax [210], and fICA [211]; the fundamental assumption common to all of these, however, is that distinct sources generate uncorrelated (*i.e.*, unrelated) and statistically independent signals. The process of finding an appropriate set of such signals is carried out in ICA by minimizing a measure of joint entropy of the signals under consideration. Another assumption of this technique which has been criticized as a weakness is that the number of sources cannot exceed the number of sensors [212]. However, to have more sources than sensors (as in a fixed MEG measurement, for example) would violate our principle of a model not creating new information.

Two phases are involved in ICA: learning and processing. In the first of these, a weighting matrix $\tilde{\mathbf{W}}$ is found, which minimizes the mutual information between channels. This process effectively makes output signals that are statistically independent, such that the multivariate probability density function of the input signals f becomes equal to

$$f = \prod_i f_i, \quad (10.258)$$

i.e., to the product of probability density functions of every independent variable [213]. In the second phase of ICA, the matrix $\tilde{\mathbf{W}}$ is applied to the signal subspace data and the parameters of the dipoles are found using a search method (*e.g.*, the simplex algorithm). A very common application of ICA is in EEG, where the method is used, for example, to recover brain signals associated with the detection of visual targets [212, 214] or to extract ocular artifacts from EEG data [215, 216]. Detailed theoretical discussions of both BSS and ICA are provided in Refs. [208, 217, 218].

10.3.5.7 Signal Space Projection

In the signal space projection (SSP) approach, the magnetic field signals m_i , $i = 1, \dots, m$, are assumed to form a time-dependent signal vector $\tilde{\mathbf{m}}(t)$ in an m -dimensional signal space. The measured signal vector $\tilde{\mathbf{m}}(t)$ can be written as

$$\tilde{\mathbf{m}}(t) = \sum_{i=1}^M a_i(t) \tilde{\mathbf{s}}_i + \tilde{\mathbf{n}}(t), \quad (10.259)$$

where $\tilde{\mathbf{s}}_i$ are the elements of an orthonormal basis spanning the m -dimensional magnetic signal space F , $a_i(t)$ contains the time-dependence information of $\tilde{\mathbf{s}}_i$, and $\tilde{\mathbf{n}}(t)$ is the noise. Because $\tilde{\mathbf{s}}_i$ are basis objects spanning F that specify the orientations of the field vectors, the former are held fixed. In other words, as Hämäläinen and Ilmoniemi put it, “each source corresponds to a constant output pattern whose amplitude changes with time” [192]. One advantage of this approach over

other methods such as PCA is that, if the $a_i(t)$ coefficients are estimated directly from $\tilde{\mathbf{m}}(t)$, no conductivity or source model is required [219].

The SSP method was introduced by Ilmoniemi et al. [220] and was applied for the first time by Miettinen [221]. To carry out SSP, two projection operators, $\tilde{\mathbf{P}}_{\perp}$ and $\tilde{\mathbf{P}}_{\parallel}$, are required to divide the signal $\tilde{\mathbf{m}}(t)$ into two parts \tilde{s}_{\perp} and \tilde{s}_{\parallel} , respectively. The first part contains information belonging to the subspace spanned by component vectors $1, \dots, k$ and the matrix $\tilde{\mathbf{K}} = (\tilde{s}_1 \tilde{s}_2 \dots \tilde{s}_k)$ is associated with it. The second part \tilde{s}_{\parallel} cannot be reproduced by any of the sources in $\tilde{\mathbf{K}}$. Thus

$$\tilde{s}_{\parallel} = \tilde{\mathbf{P}}_{\parallel} \tilde{\mathbf{m}} \quad \text{and} \quad \tilde{s}_{\perp} = \tilde{\mathbf{P}}_{\perp} \tilde{\mathbf{m}}. \quad (10.260)$$

The matrix representations of the operators $\tilde{\mathbf{P}}_{\perp}$ and $\tilde{\mathbf{P}}_{\parallel}$ can be computed using the SVD of $\tilde{\mathbf{K}}$

$$\tilde{\mathbf{K}} = \tilde{\mathbf{U}} \tilde{\mathbf{A}} \tilde{\mathbf{V}}^T. \quad (10.261)$$

The first k columns of the matrix $\tilde{\mathbf{U}}$ form an orthonormal basis for the column space of $\tilde{\mathbf{K}}$, yielding the results

$$\tilde{\mathbf{P}}_{\parallel} = \tilde{\mathbf{U}}_k \tilde{\mathbf{U}}_k^T \quad (10.262)$$

and

$$\tilde{\mathbf{P}}_{\perp} = \tilde{\mathbf{I}} - \tilde{\mathbf{P}}_{\parallel}. \quad (10.263)$$

The data estimates $\hat{\mathbf{a}}(t)$ of the theoretical amplitudes $a_i(t)$ are then computed from

$$\hat{\mathbf{a}}(t) = \tilde{\mathbf{V}} \tilde{\mathbf{A}}^{-1} \tilde{\mathbf{U}}^T \tilde{\mathbf{m}}(t). \quad (10.264)$$

The operators $\tilde{\mathbf{P}}_{\perp}$ and $\tilde{\mathbf{P}}_{\parallel}$ effectively form a spatial filter since they allow one to isolate signals that were generated only by the sources of interest. If the sources included in $\tilde{\mathbf{K}}$ are only artifact-related, the information contained in the artifact-free signal can be separated into \tilde{s}_{\perp} . For this reason, the SSP method is particularly valuable as an artifact removal tool [222, 223] and has been used as such in a variety of applications [192, 224–226] including, among others, neuronal source characterization [227] and gastrointestinal inverses [47].

10.3.5.8 Other Three-Dimensional Methods

LORETA (low resolution electromagnetic tomography) was introduced by Pascual-Marqui et al. [228], who proposed that the inverse solution describing the current density throughout the full volume of the conductor can be selected based on the criterion of smoothness associated with the spatial distribution of sources. Mathematically, this method minimizes the squared norm of the Laplacian of the

weighted three-dimensional current density vector field [229]. One of the demonstrated advantages of this algorithm is that it provides small localization errors for deep sources; the method has been applied successfully to study auditory event-related potentials [230] and epileptiform activity [229]. A more recent algorithm, dubbed standardized LORETA (sLORETA) [191, 231, 232], does not use the Laplacian as a measure of spatial smoothness in computing the inverse solution. It relies instead on the calculation of statistical maps indicating the probable locations of sources. The performance of this method under the presence of noise is evaluated in Ref. [232].

Many other inverse techniques exist, such as the maximum entropy of the mean (MEM) method of Clarke and Janday [233, 234], probabilistic reconstruction of multiple sources (PROMS) [235], and magnetic field tomography (MFT) [236], all of which make use of probabilistic methods to estimate the detectable impressed current \vec{j}^i . In MFT [110], the value of the impressed current is computed independently for each time slice; the method is also best adapted to the detection of distributed sources. In the Bayesian approach [237, 238] the prior knowledge regarding the nature of the sources is represented as a prior probability, which is combined with a probabilistic description of the data to compute a posterior distribution by making use of Bayes' theorem; the optimal distribution of sources maximizes this probabilistic quantity.

As a final remark, it is interesting to note that most common linear inverse algorithms are highly related at a theoretical level and differ mostly in how the source covariance matrix of the data is constructed. As demonstrated by Mosher et al. [239], the method of estimating data and noise covariances used in a particular technique is important because many minimum norm algorithms are intimately dependent on these parameters. Conceptually, this is essential because the estimation of covariances is strongly related to the distinction between data and noise, which plays a vital role in the source recovery process.

10.4 Conclusions

Very few of the peculiarities or techniques described above to solve the magnetic inverse problem are unique to SQUID magnetometers, but in fact arise from the nature of the fields themselves. SQUIDS are among the most sensitive magnetometers, and all of this sensitivity is generally required to measure biomagnetic fields. With few exceptions, the biomagnetic inverse problem is a three-dimensional one, and has no unique solution. As a result, a wide range of techniques is utilized to convert biomagnetic images into approximations or constrained descriptions of bioelectric sources. The NDE and geomagnetic applications of SQUIDS are more forgiving, in that often the samples are two-dimensional, for which there are unique inverse solutions, or applied fields can be controlled in a manner that provides additional information required to solve the inverse problem. It is important to realize, however, that many of the techniques outlined in

this chapter, even in their present rudimentary state of development, can be used to analyze field images obtained from optical, fluxgate, Hall probe, and magnetoresistive magnetometers. Given the promise of these and other advanced imaging techniques, it is enticing to consider the future use of SQUID cameras based upon digital SQUID techniques to provide a thousand integrated digital magnetometers on a single chip [240, 241], or imaging optical magnetometers [242]. Meanwhile, there is much work that can be done to explore even more fully the mathematics and experimental techniques of magnetic imaging with SQUIDs and other magnetometers.

Acknowledgments

Much of the research described within this chapter was funded by grants from the Air Force Office of Scientific Research, the Electric Power Research Institute, and the National Institutes of Health. We are indebted to Afshin Abedi, John Barach, Alan Bradshaw, James Cadzow, Anthony Ewing, Luis Fong, Jenny Holzer, William Jenks, Xangkang Li, Yu Pei Ma, Bradley Roth, Nestor Sepulveda, Daniel Staton, Shaofen Tan, and Ian Thomas for their major contributions to the Vanderbilt magnetic imaging effort, and their papers from which we have drawn heavily in preparing this chapter. We thank Hans Koch and Wolfgang Haberkorn for providing the historical background on the nonuniqueness of the inverse problem solution. We also thank William Jenks, Margaret Khayat, Eduardo Parente Ribeiro, Daniel Staton, and Leonora Wikswow for their comments on predecessors of this manuscript, and Licheng Li for her care in preparing many of the illustrations. We especially thank Harold Weinstock for his encouragement and support of this research. We are deeply indebted to Don Berry, Cheryl Cosby, and Allison Price for their unflagging assistance and attention to detail in preparing the manuscript for this chapter, including but not limited to maintaining the reference database, typing the many equations, revising or creating each of the drawings, and very careful editing.

References

- 1 Helmholtz, H. (1853) Ueber einige Gesetze der Vertheilung elektrischer Ströme in körperlichen Leitern mit Anwendung auf die thierisch-electrischen Versuche, *Ann. Phys. Chem.* **89**, 211–233, 353–377.
- 2 Braginski, A.I. (2005) Personal communication.
- 3 Bradshaw, L.A. and Wikswow, J.P., Jr. (1999) Vector or scalar magnetometer arrays?, in *Proceedings of the First Joint BMES/EMBS Conference*, Vol. 2, Atlanta, GA, p. 888.
- 4 Nalbach, M. and Dossel, O. (2002) Comparison of sensor arrangements of MCG and ECG with respect to information content, *Physica C* **372**, 254–258.
- 5 Baudenbacher, F., Peters, N. T. and Wikswow, J. P., Jr. (2002) High resolution low-temperature superconductivity superconducting quantum interference device microscope for imaging mag-

- netic fields of samples at room temperatures, *Rev. Sci. Instrum.* **73**, 1247–1254.
- 6 Fong, L. E., Holzer, J. R., McBride, K. K., Lima, E. A., Baudenbacher, F. and Radparvar, M. (2005) High-resolution room-temperature sample scanning superconducting quantum interference device microscope configurable for geological and biomagnetic applications, *Rev. Sci. Instrum.* **76**, 053703.
 - 7 Cohen, D., Edelsack, E. A. and Zimmerman, J. E. (1970) Magnetocardiograms taken inside a shielded room with a superconducting point-contact magnetometer, *Appl. Phys. Lett.* **16**, 278–280.
 - 8 Weiss, B. P., Kirschvink, J. L., Baudenbacher, F. J., Vali, H., Peters, N. T., Macdonald, F. A. and Wikswo, J. P. (2000) A low temperature transfer of ALH84001 from Mars to Earth, *Science* **290**, 791–795.
 - 9 Wikswo, J. P., Jr. (1996) The magnetic inverse problem for NDE, in *SQUID Sensors: Fundamentals, Fabrication and Applications*, Weinstock, H. (ed.), Kluwer, The Netherlands, pp. 629–695.
 - 10 Ma, Y. P., Thomas, I. M., Lauder, A. and Wikswo, J. P., Jr. (1993) A high resolution imaging susceptometer, *IEEE Trans. Appl. Supercond.* **3**, 1941–1944.
 - 11 Wikswo, J. P., Jr. (1978) The calculation of the magnetic field from a current distribution: application to finite element techniques, *IEEE Trans. Magn.* **Mag14**, 1076–1077.
 - 12 Geselowitz, D. B. (1970) On the magnetic field generated outside an inhomogeneous volume conductor by internal current sources, *IEEE Trans. Magn.* **Mag6**, 346–347.
 - 13 Wikswo, J. P., Jr. (1983) Theoretical aspects of the EEG-MEG relationship, in *Biomagnetism: An Interdisciplinary Approach*, Williamson, S. J., Romani, G.-L., Kaufman, L. and Modena, I. (eds.), Plenum, New York, pp. 311–326.
 - 14 Wikswo, J. P., Jr. and Barach, J. P. (1982) Possible sources of new information in the magnetocardiogram, *J. Theor. Biol.* **95**, 721–729.
 - 15 Roth, B. J. and Wikswo, J. P., Jr. (1986) Electrically silent magnetic fields, *Biophys. J.* **50**, 739–745.
 - 16 Demunck, J. C., Vandijk, B. W. and Spekreijse, H. (1988) Mathematical dipoles are adequate to describe realistic generators of human-brain activity, *IEEE Trans. Biomed. Eng.* **35**, 960–966.
 - 17 Williamson, S. J. and Kaufman, L. (1981) Biomagnetism topical review, *J. Magn. Magn. Mater.* **22**, 129–201.
 - 18 Wikswo, J. P., Jr. and Swinney, K. R. (1985) Scalar multipole expansions and their dipole equivalents, *J. Appl. Phys.* **57**, 4301–4308.
 - 19 Brody, D. A. (1968) The inverse determination of simple generator configurations from equivalent dipole and multipole information, *IEEE Trans. Biomed. Eng.* **BME15**, 106–110.
 - 20 Horacek, B. M. (1973) Digital model for studies in magnetocardiography, *IEEE Trans. Magn.* **Mag9**, 440–444.
 - 21 Grynspan, F. (1971) Relationship between the surface electromagnetic fields and the electrical activity of the heart, Ph.D. Dissertation, University of Pennsylvania.
 - 22 Wikswo, J. P., Jr., Malmivuo, J. A. V., Barry, W. H., Leifer, M. C. and Fairbank, W. M. (1979) The theory and application of magnetocardiography, in *Advances in Cardiovascular Physics*, Vol. 2. Ghista, D. N., Vollenhoven, V. E. and Yang, W. (eds.), Karger, Basel/New York, pp. 1–67.
 - 23 Jackson, J. D. (1975) *Classical Electrodynamics*, Wiley, New York.
 - 24 Cohen, D. and Hosaka, H. (1976) Magnetic field produced by a current dipole, *J. Electrocardiol.* **9**, 409–417.
 - 25 Wikswo, J. P., Jr. and Swinney, K. R. (1984) A comparison of scalar multipole expansions, *J. Appl. Phys.* **56**, 3039–3049.
 - 26 Castellanos, A., Panizo, M. and Rivas, J. (1978) Magnetostatic multipoles in cartesian coordinates, *Am. J. Phys.* **46**, 1116–1117.
 - 27 Gonzalez, H., Juarez, S. R., Kiellandowski, P. and Loewe, M. (1998) Multipole expansion in magnetostatics, *Am. J. Phys.* **66**, 228–231.
 - 28 Geselowitz, D. B. (1965) Two theorems concerning the quadrupole applicable to electrocardiography, *IEEE Trans. Biomed. Eng.* **BM12**, 164–168.

- 29 Gray, C. G. (1978) Simplified derivation of magnetostatic multipole expansion using scalar potential, *Am. J. Phys.* **46**, 582–583.
- 30 Gray, C. G. (1979) Magnetic multipole expansions using the scalar potential, *Am. J. Phys.* **47**, 457–459.
- 31 Gray, C. G. (1980) Definition of the magnetic quadrupole-moment, *Am. J. Phys.* **48**, 984–985.
- 32 Nolte, G. and Curio, G. (1997) On the calculation of magnetic fields based on multipole modeling of focal biological current sources, *Biophys. J.* **73**, 1253–1262.
- 33 Mosher, J. C., Leahy, R. M., Shattuck, D. W. and Baillet, S. (1999) MEG source imaging using multipolar expansions, in *Information Processing in Medical Imaging: 16th International Conference, IPMI '99*, Visegrad, Hungary, Kuba, A., Samal, M. and Todd-Pokropek, A. (eds.), Springer, Berlin/New York, pp. 15–28.
- 34 Jerbi, K., Mosher, J. C., Baillet, S. and Leahy, R. M. (2002) On MEG forward modelling using multipolar expansions, *Phys. Med. Biol.* **47**, 523–555.
- 35 Jerbi, K., Baillet, S., Mosher, J. C., Nolte, G., Garnero, L. and Leahy, R. M. (2004) Localization of realistic cortical activity in MEG using current multipoles, *NeuroImage* **22**, 779–793.
- 36 Ermer, J. J., Mosher, J. C., Baillet, S. and Leahy, R. M. (2001) Rapidly recomputable EEG forward models for realistic head shapes, *Phys. Med. Biol.* **46**, 1265–1281.
- 37 Brody, D. A. and Bradshaw, J. C. (1962) The equivalent generator components of uniform double layers, *Bull. Math. Biophys.* **24**, 183–195.
- 38 Lynn, M. S., Barnard, A. C. L. and Holt, J. H. (1967) A proposed method for the inverse problem in electrocardiology, *Biophys. J.* **7**, 925–945.
- 39 Holt, J. H., Barnard, A. C. L. and Lynn, M. S. (1969) A study of the human heart as a multiple dipole electrical source; II. Diagnosis and quantitation of left ventricular hypertrophy, *Circulation* **40**, 697–718.
- 40 Holt, J. H. and Barnard, A. C. L. (1973) Body surface potentials in ventricular hypertrophy – analysis using a multipole dipole model of the heart, in *Computer application on ECG and VCG analysis, Proceedings of the 2nd IFIP TC-4 Working Conference on Computer Application on ECG and VCG Analysis*, North Holland, Amsterdam, pp. 333–349.
- 41 Wiksw, J. P., Jr., Gevins, A. and Williamson, S. J. (1993) The future of the EEG and MEG, *Electroencephalogr. Clin. Neurophysiol.* **87**, 1–9.
- 42 Hillebrand, A. and Barnes, G. R. (2002) A quantitative assessment of the sensitivity of whole-head MEG to activity in the adult human cortex, *NeuroImage* **16**, 638–650.
- 43 Okada, Y., Lauritzen, M. and Nicholson, C. (1987) MEG source models and physiology, *Phys. Med. Biol.* **32**, 43–51.
- 44 Okada, Y. C., Lahteenmaki, A. and Xu, C. B. (1999) Experimental analysis of distortion of magnetoencephalography signals by the skull, *Clin. Neurophysiol.* **110**, 230–238.
- 45 Wiksw, J. P., Jr. and Roth, B. J. (1988) Magnetic determination of the spatial extent of a single cortical current source: a theoretical analysis, *Electroencephalogr. Clin. Neurophysiol.* **69**, 266–276.
- 46 Bradshaw, L. A. and Wiksw, J. P. (2001) Spatial filter approach for evaluation of the surface Laplacian of the electroencephalogram and magnetoencephalogram, *Ann. Biomed. Eng.* **29**, 202–213.
- 47 Bradshaw, L. A., Wijesinghe, R. S. and Wiksw, J. P. (2001) Spatial filter approach for comparison of the forward and inverse problems of electroencephalography and magnetoencephalography, *Ann. Biomed. Eng.* **29**, 214–226.
- 48 Tan, S., Roth, B. J. and Wiksw, J. P., Jr. (1990) The magnetic field of cortical current sources: the application of a spatial filtering model to the forward and inverse problems, *Electroencephalogr. Clin. Neurophysiol.* **76**, 73–85.
- 49 Nolte, G. and Curio, G. (2000) Current multipole expansion to estimate lateral extent of neuronal activity: a theoretical analysis, *IEEE Trans. Biomed. Eng.* **47**, 1347–1355.
- 50 Allescher, H. D., Abraham-Fuchs, K., Dunkel, R. E. and Classen, M. (1998)

- Biomagnetic 3-dimensional spatial and temporal characterization of electrical activity of human stomach, *Dig. Dis. Sci.* **43**, 683–693.
- 51 Irimia, A. and Bradshaw, L. A. (2003) Theoretical ellipsoidal model of gastric electrical control activity propagation, *Phys. Rev. E* **68**, 051905.
- 52 Irimia, A., Beauchamp, J. J. and Bradshaw, L. A. (2004) Theoretical and computational multiple regression study of gastric electrical activity using dipole tracing from magnetic field measurements, *J. Biol. Phys.* **30**, 239–259.
- 53 Irimia, A. and Bradshaw, L. A. (2004) Theoretical and computational methods for the noninvasive detection of gastric electrical source coupling, *Phys. Rev. E* **69**, 051920.
- 54 Dallas, W. J. (1985) Fourier space solution to the magnetostatic imaging problem, *Appl. Opt.* **24**, 4543–4546.
- 55 Kullmann, W. H. and Dallas, W. J. (1987) Fourier imaging of electrical currents in the human brain from their magnetic fields, *IEEE Trans. Biomed. Eng.* **BME34**, 837–842.
- 56 Roth, B. J., Sepulveda, N. G. and Wikswo, J. P., Jr. (1989) Using a magnetometer to image a two-dimensional current distribution, *J. Appl. Phys.* **65**, 361–372.
- 57 Alvarez, R. E. (1990) Biomagnetic Fourier imaging, *IEEE Trans. Med. Imaging* **9**, 299–304.
- 58 Smith, W. E., Dallas, W. J., Kullmann, W. H. and Schlitt, H. A. (1990) Linear estimation theory applied to the reconstruction of a 3-D vector current distribution, *Appl. Opt.* **29**, 658–667.
- 59 Alvarez, R. E. (1991) Filter functions for computing multipole moments from the magnetic-field normal to a plane, *IEEE Trans. Med. Imaging* **10**, 375–381.
- 60 Staton, D. J., Rousakov, S. V. and Wikswo, J. P., Jr. (1996) Conductivity imaging in plates using current injection tomography, *Rev. Prog. Quant. Nondestr. Eval.* **15**, 845–851.
- 61 Wakai, R. T. and Lutter, W. J. (2002) Matched-filter template generation via spatial filtering: application to fetal biomagnetic recordings, *IEEE Trans. Biomed. Eng.* **49**, 1214–1217.
- 62 Bradshaw, L. A., Richards, W. O. and Wikswo, J. P., Jr. (2001) Volume conductor effects on the spatial resolution of magnetic fields and electric potentials from gastrointestinal electrical activity, *Med. Biol. Eng. Comp.* **39**, 35–43.
- 63 Chatrathorn, S., Fleet, E.F. and Wellstood, F.C. (1999) High-Tc scanning SQUID microscopy: imaging integrated circuits beyond the standard near-field limit, *Bull. APS* **44**, 1554.
- 64 Chatrathorn, S., Fleet, E. F., Wellstood, F. C., Knauss, L. A. and Eiles, T. M. (2000) Scanning SQUID microscopy of integrated circuits, *Appl. Phys. Lett.* **76**, 2304–2306.
- 65 Staton, D. J., Friedman, R. N. and Wikswo, J. P., Jr. (1993) High-resolution SQUID imaging of octupolar currents in anisotropic cardiac tissue, *IEEE Trans. Appl. Supercond.* **3**, 1934–1936.
- 66 Staton, D.J. (1994) Magnetic imaging of applied and propagating action current in cardiac tissue slices: determination of anisotropic electrical conductivities in a two dimensional bidomain, Ph.D. Dissertation, Vanderbilt University.
- 67 Wikswo, J. P., Jr. (1994) The complexities of cardiac cables: virtual electrode effects, *Biophys. J.* **66**, 551–553.
- 68 Wikswo, J.P., Jr. (1978) Optimization of SQUID differential magnetometers, *AIP Conf. Proc.* **44**, 145–149.
- 69 Wikswo, J. P., Jr. (1988) High-resolution measurements of biomagnetic fields, in *Advances in Cryogenic Engineering*, Fast, R. W. (ed.), Plenum, pp. 107–116.
- 70 Wikswo, J. P., Jr. (1996) High-resolution magnetic imaging: cellular action currents and other applications, in *SQUID Sensors: Fundamentals, Fabrication and Applications*, Weinstock, H. (ed.), Kluwer, The Netherlands, pp. 307–360.
- 71 Roth, B. J. and Wikswo, J. P., Jr. (1990) Apodized pickup coils for improved spatial resolution of SQUID magnetometers, *Rev. Sci. Instrum.* **61**, 2439–2448.
- 72 Poularikas, A. D. (1996) *The Transforms and Applications Handbook*, CRC Press, Boca Raton, FL.
- 73 Abedi, A., Fellenstein, J., Lucas, A. J. and Wikswo, J. P., Jr. (1999) A superconducting quantum interference device

- magnetometer system for quantitative analysis and imaging of hidden corrosion activity in aircraft aluminum structures, *Rev. Sci. Instrum.* **70**, 4640–4651.
- 74 Bradshaw, L.A. (1995) Measurement and modeling of gastrointestinal bioelectric and biomagnetic fields, Ph.D. Dissertation, Vanderbilt University.
- 75 Blakely, R. J. (1995) *Potential Theory in Gravity and Magnetic Applications*, Cambridge University Press, New York.
- 76 Fedi, M. and Florio, G. (2002) A stable downward continuation by using the ISVD method, *Geophys. J. Int.* **151**, 146–156.
- 77 Pawlowski, R. S. (1995) Preferential continuation for potential-field anomaly enhancement, *Geophysics* **60**, 390–398.
- 78 Tan, S. (1992) Linear system imaging and its applications to magnetic measurements by SQUID magnetometers, Ph.D. Dissertation, Vanderbilt University.
- 79 Tan, S., Sepulveda, N. G. and Wikswo, J. P., Jr. (1995) A new finite-element approach to reconstruct a bounded and discontinuous two-dimensional current image from a magnetic field map, *J. Comput. Phys.* **122**, 150–164.
- 80 Hosaka, H. and Cohen, D. (1976) Visual determination of generators of the magnetocardiogram, *J. Electrocardiol.* **9**, 426–432.
- 81 Thomas, I. M., Freake, S. M., Swithenby, S. J. and Wikswo, J. P., Jr. (1993) A distributed quasi-static ionic current source in the 3–4 day old chicken embryo, *Phys. Med. Biol.* **38**, 1311–1328.
- 82 Barbosa, C. H., Bruno, A. C., Scavarda, L. F., Lima, E. A., Ribeiro, P. C. and Keller, C. (1995) Image-processing techniques for NDE SQUID systems, *IEEE Trans. Appl. Supercond.* **5**, 2478–2481.
- 83 Oh, S., Ramon, C., Marks, R. J., II, Nelson, A. C. and Meyer, M. G. (1993) Resolution enhancement of biomagnetic images using the method of alternating projections, *IEEE Trans. Biomed. Eng.* **40**, 323–328.
- 84 Li, X., Cadzow, J.A. and Wikswo, J.P. (1996) Reconstruction of electric current density distribution from magnetometer measurements (unpublished).
- 85 Lima, E. A., Bruno, A. C. and Szczupak, J. (1999) Two-dimensional spatial frequency response of SQUID planar gradiometers, *Supercond. Sci. Technol.* **12**, 949–952.
- 86 Lima, E. A. and Bruno, A. C. (2001) Improving the detection of flaws in steel pipes using SQUID planar gradiometers, *IEEE Trans. Appl. Supercond.* **11**, 1299–1302.
- 87 Lima, E. A., Bruno, A. C. and Szczupak, J. (2002) Two-dimensional deconvolution technique to recover the original magnetic field from the flux measured by SQUID planar gradiometers, *Supercond. Sci. Technol.* **15**, 1259–1267.
- 88 Lima, E. A. and Bruno, A. C. (2002) Experimental verification of a spatial deconvolution procedure for planar gradiometer configurations, *Physica C* **368**, 100–104.
- 89 Lima, E. A. and Bruno, A. C. (2003) Spatial frequency response of conventional and non-conventional SQUID gradiometers, *IEEE Trans. Appl. Supercond.* **13**, 735–738.
- 90 Bruno, A. C., Ribeiro, P. C., von der Weid, J. P. and Symko, O. G. (1986) Discrete spatial filtering with SQUID gradiometers in biomagnetism, *J. Appl. Phys.* **59**, 2584–2589.
- 91 Bruno, A.C., Guida, A.V. and Ribeiro, P.C. (1987) Planar gradiometer input signal recovery using a Fourier technique, in *Biomagnetism '87, 6th Int. Conf.*, Tokyo, pp. 454–457.
- 92 Ribeiro, P. C., Bruno, A. C., Paulsen, C. C. and Symko, O. G. (1987) Spatial Fourier transform method for evaluating SQUID gradiometers, *Rev. Sci. Instrum.* **58**, 1510–1513.
- 93 Bruno, A. C. and Ribeiro, P. C. (1989) Spatial deconvolution algorithm for superconducting planar gradiometer arrays, *IEEE Trans. Magn.* **25**, 1219–1222.
- 94 Alvarez, R. E. (1991) Filter functions for computing multipole moments from the magnetic-field normal to a plane, *IEEE Trans. Med. Imaging* **10**, 375–381.
- 95 Jooss, C., Warthmann, R., Forkl, A. and Kronmüller, H. (1998) High-resolution magneto-optical imaging of critical cur-

- rents in $\text{YBa}_2\text{Cu}_3\text{O}_{7-\delta}$ thin films, *Physica C* **299**, 215–230.
- 96 Laviano, F., Botta, D., Chiodoni, A., Gerbaldo, R., Ghigo, G., Gozzelino, L., Zannella, S. and Mezzetti, E. (2003) An improved method for quantitative magneto-optical analysis of superconductors, *Supercond. Sci. Technol.* **16**, 71–79.
- 97 Chatrathorn, S., Fleet, E. F. and Wellstood, F. C. (2002) Relationship between spatial resolution and noise in scanning superconducting quantum interference device microscopy, *J. Appl. Phys.* **92**, 4731–4740.
- 98 Press, W. H., Flannery, B. P. and Teukolsky, S. A. (1992) Singular value decomposition, in *Numerical Recipes in FORTRAN: The Art of Scientific Computing*. Press, W. H. (ed.), Cambridge University Press, Cambridge, UK/New York, pp. 51–63.
- 99 Golub, G. H. and Van Loan, C. F. (1996) *Matrix Computations*, Johns Hopkins University Press, Baltimore, MD.
- 100 Benzing, W., Scherer, T. and Jutzi, W. (1993) Inversion calculation of two dimensional current distributions from their magnetic field, *IEEE Trans. Appl. Supercond.* **3**, 1902–1905.
- 101 Ramon, C., Meyer, M. G., Nelson, A. C., Spelman, F. A. and Lamping, J. (1993) Simulation studies of biomagnetic computed tomography, *IEEE Trans. Biomed. Eng.* **40**, 317–322.
- 102 Feldmann, D. M. (2004) Resolution of two-dimensional currents in superconductors from a two-dimensional magnetic field measurement by the method of regularization, *Phys. Rev. B* **69**, 144515.
- 103 Brandt, E. H. (1995) Square and rectangular thin superconductors in a transverse magnetic-field, *Phys. Rev. Lett.* **74**, 3025–3028.
- 104 Wijngaarden, R. J., Heeck, K., Spoelder, H. J. W., Surdeanu, R. and Griessen, R. (1998) Fast determination of 2D current patterns in flat conductors from measurement of their magnetic field, *Physica C* **295**, 177–185.
- 105 Soika, E. and Moller, H. J. (2004) Magnetic field measurements and numerical simulation of the current distribution in the emitter region of solar cells, *J. Magn. Magn. Mater.* **272–276**, 667–668.
- 106 Tripp, J. H. (1983) Physical concepts and mathematical models, in *Biomagnetism: An Interdisciplinary Approach*, Williamson, S. J. (ed.), Plenum, New York, pp. 101–138.
- 107 Jenkins, J., Wu, D. and Arzbaecher, R. (1976) Use of the atrial electrogram in computer detection and classification of cardiac arrhythmias, in *Proceedings of the 29th ACEMB Conference*, Boston, MA, p. 128.
- 108 Hurley, D. C., Ma, Y. P., Tan, S. and Wikswo, J. P., Jr. (1993) Imaging of small defects in nonmagnetic tubing using a SQUID magnetometer, *Res. Nondestr. Eval.* **5**, 1–29.
- 109 Hurley, D. C., Ma, Y. P., Tan, S. and Wikswo, J. P., Jr. (1993) A comparison of SQUID imaging techniques for small defects in nonmagnetic tubes, *Rev. Prog. Quant. Nondestr. Eval.* **12**, 633–640.
- 110 Ioannides, A. A., Bolton, J. P. R. and Clarke, C. J. S. (1990) Continuous probabilistic solutions to the biomagnetic inverse problem, *Inverse Problems* **6**, 523–542.
- 111 Haacke, E. M., Liang, Z. P. and Izen, S. H. (1989) Constrained reconstruction – a superresolution, optimal signal-to-noise alternative to the Fourier-transform in magnetic-resonance imaging, *Med. Phys.* **16**, 388–397.
- 112 Seger, M., Fischer, G., Modre, R., Messnarz, B., Hanser, F. and Tilg, B. (2005) Lead field computation for the electrocardiographic inverse problem – finite elements versus boundary elements, *Comp. Meth. Programs Biomed.* **77**, 241–252.
- 113 Wikswo, J. P., Jr., Sepulveda, N. G., Ma, Y. P., Henry, W. P., Crum, D. B. and Statton, D. J. (1993) An improved method for magnetic identification and localization of cracks in conductors, *J. Nondestr. Eval.* **12**, 109–119.
- 114 Sepulveda, N.G. and Wikswo, J.P. (1994) Differential operators and their applications to magnetic measurements using SQUID magnetometers (unpublished).
- 115 Thome, D. K., Fitzpatrick, G. L. and Skaugset, R. L. (1996) Aircraft corrosion

- and crack inspection using advanced magneto-optic imaging technology, *Proc. SPIE* **2945**, 365–373.
- 116 Fitzpatrick, G. L., Thome, D. K., Skaugset, R. L., Shih, E. Y. C. and Shih, W. C. L. (1993) Magneto-optic eddy-current imaging of aging aircraft – a new NDI technique, *Mater. Eval.* **51**, 1402–1407.
- 117 Ma, Y. P. and Wikswo, J. P., Jr. (1994) SQUID eddy current techniques for detection of second layer flaws, *Rev. Prog. Quant. Nondestr. Eval.* **13**, 303–309.
- 118 Ma, Y. P. and Wikswo, J. P., Jr. (1995) Techniques for depth-selective, low-frequency eddy current analysis for SQUID-based nondestructive testing, *J. Nondestr. Eval.* **14**, 149–167.
- 119 Ma, Y. P. and Wikswo, J. P., Jr. (1996) Depth-selective SQUID eddy current techniques for second layer flaw detection, *Rev. Prog. Quant. Nondestr. Eval.* **15**, 401–408.
- 120 Ma, Y. P. and Wikswo, J. P., Jr. (1998) SQUID magnetometers for depth-selective, oriented eddy current imaging, *Rev. Prog. Quant. Nondestr. Eval.* **17A**, 1067–1074.
- 121 Ioannides, A. A. and Grimes, D. I. F. (1987) Line current source reconstructions from magnetic-flux measurements, *Phys. Med. Biol.* **32**, 146.
- 122 McKirdy, D. M., Cochran, A. and Donaldson, G. B. (1996) Forward and inverse processing in electromagnetic NDE using SQUIDS, *Rev. Prog. Quant. Nondestr. Eval.* **15A**, 347–354.
- 123 Nolte, G. and Curio, G. (1999) Perturbative analytical solutions of the electric forward problem for realistic volume conductors, *J. Appl. Phys.* **86**, 2800–2811.
- 124 Cruse, T. A., Ewing, A. P. and Wikswo, J. P., Jr. (1999) Green's function formulation of Laplace's equation for electromagnetic crack detection, *Computat. Mech.* **23**, 420–429.
- 125 Ewing, A. P., Cruse, T. A. and Wikswo, J. P., Jr. (1998) A SQUID NDE measurement model using BEM, *Rev. Prog. Quant. Nondestr. Eval.* **17A**, 1083–1090.
- 126 Ewing, A. P., Barbosa, C. H., Cruse, T. A., Bruno, A. C. and Wikswo, J. P., Jr. (1998) Boundary integral equations for modeling arbitrary flaw geometries in electric current injection NDE, *Rev. Prog. Quant. Nondestr. Eval.* **17A**, 1011–1015.
- 127 Lutkenhoner, B. and Menendez, R. G. D. P. (1997) The resolution-field concept, *Electroencephalogr. Clin. Neurophysiol.* **102**, 326–334.
- 128 Lutkenhoner, B. (2003) Magnetoencephalography and its Achilles' heel, *J. Physiol. Paris* **97**, 641–658.
- 129 Lines, L. R. and Treitel, S. (1984) Tutorial, a review of least-squares inversion and its application to geophysical problems, *Geophys. Prospect.* **32**, 159–186.
- 130 Oldenburg, D. (1990) Inversion of electromagnetic data: an overview of new techniques, *Surv. Geophys.* **11**, 231–270.
- 131 Marcuello-Pascual, A., Kaikkonen, P. and Pous, J. (1992) 2-D inversion of MT data with a variable model geometry, *Geophys. J. Int.* **110**, 297–304.
- 132 Parker, R. L. (1977) Understanding inverse theory, *Annu. Rev. Earth Planetary Sci.* **5**, 35–64.
- 133 Reitz, J. R. and Milford, F. J. (1967) *Foundations of Electromagnetic Theory*, Addison-Wesley, Reading, MA.
- 134 Beardsley, I. A. (1989) Reconstruction of the magnetization in a thin film by a combination of Lorentz microscopy and field measurements, *IEEE Trans. Magn.* **25**, 671–677.
- 135 Tan, S., Ma, Y. P., Thomas, I. M. and Wikswo, J. P., Jr. (1996) Reconstruction of two-dimensional magnetization and susceptibility distributions from the magnetic field of soft magnetic materials, *IEEE Trans. Magn.* **32**, 230–234.
- 136 Tan, S., Ma, Y. P., Thomas, I. M. and Wikswo, J. P., Jr. (1993) High resolution SQUID imaging of current and magnetization distributions, *IEEE Trans. Appl. Supercond.* **3**, 1945–1948.
- 137 Thomas, I. M., Ma, Y. P. and Wikswo, J. P., Jr. (1993) SQUID NDE: detection of surface flaws by magnetic decoration, *IEEE Trans. Appl. Supercond.* **3**, 1949–1952.
- 138 Thomas, I. M., Ma, Y. P., Tan, S. and Wikswo, J. P., Jr. (1993) Spatial resolution and sensitivity of magnetic susceptibility imaging, *IEEE Trans. Appl. Supercond.* **3**, 1937–1940.

- 139 Thomas, I. M., Moyer, T. C. and Wiksw, J. P., Jr. (1992) High resolution magnetic susceptibility imaging of geological thin sections: pilot study of a pyroclastic sample from the Bishop Tuff, California, U.S.A., *Geophys. Res. Lett.* **19**, 2139–2142.
- 140 Weiss, B. P., Baudenbacher, F. J., Wiksw, J. P. and Kirschvink, J. L. (2001) Magnetic microscopy promises a leap in sensitivity and resolution, *EoS Trans. AGU* **82**, 513–518.
- 141 Wiksw, J. P., Jr., Ma, Y. P., Sepulveda, N. G., Tan, S., Thomas, I. M. and Lauder, A. (1993) Magnetic susceptibility imaging for nondestructive evaluation, *IEEE Trans. Appl. Supercond.* **3**, 1995–2002.
- 142 Ribeiro, E. P., Wiksw, J. P., Jr., Ribeiro, P. C. and Szczupak, J. (1996) Magnetic susceptibility tomography with nonuniform field, in *Biomag 96: Proceedings of the 10th Int. Conf. on Biomagnetism*, Aine, C. J., Okada, Y. C., Stroink, G. and Swithenby, S. J. (eds.), Springer, New York, pp. 671–674.
- 143 Ribeiro, E.P., Wiksw, J.P., Jr., Ribeiro, P.C. and Szczupak, J. (1997) Magnetic susceptibility tomography with filtered singular values, *Med. Biol. Eng. Comp.* **35** (Suppl. I), 14.
- 144 Ribeiro, E.P. (1996) Magnetic susceptibility tomography with superconducting magnetometer SQUID, Ph.D. Dissertation, PUC-Rio, Rio de Janeiro.
- 145 Sepulveda, N. G., Thomas, I. M. and Wiksw, J. P., Jr. (1994) Magnetic susceptibility tomography for three-dimensional imaging of diamagnetic and paramagnetic objects, *IEEE Trans. Magn.* **30**, 5062–5069.
- 146 Thomas, I.M., Sepulveda, N.G. and Wiksw, J.P., Jr. (1993) Magnetic susceptibility tomography: a new modality for three-dimensional biomedical imaging, in *Proceedings of the 15th Annual International Conference of the IEEE Engineering in Medicine and Biology Society, Engineering Solutions to Current Health Care Problems*, Vol. 15, Part I, San Diego, CA, pp. 94–95.
- 147 Wiksw, J. P., Jr., Sepulveda, N. G. and Thomas, I. M. (1995) Three-dimensional biomagnetic imaging with magnetic susceptibility tomography, in *Biomagnetism: Fundamental Research and Clinical Applications: Proceedings of the 9th International Conference on Biomagnetism*, Baumgartner, C., Deecke, L., Stroink, G. and Williamson, S. J. (eds.), IOS Press, Burk, VA, pp. 780–784.
- 148 Jenks, W. G., Sadeghi, S. S. H. and Wiksw, J. P., Jr. (1997) SQUIDs for nondestructive evaluation, *J. Phys. D: Appl. Phys.* **30**, 293–323.
- 149 Jenks, W.G., Ma, Y.P., Parente Ribeiro, E. and Wiksw, J.P. (1997) SQUID NDE of composite materials with magnetic tracers (unpublished).
- 150 Thomas, I. M. and Friedman, R. N. (1993) Magnetic susceptibility imaging of macrophage activity in rat liver using intravenous superparamagnetic tracers, in *Proceedings of the Annual International Conference of the IEEE Engineering in Medicine and Biology Society*, Szeto, A. Y. J. and Rangayyan, R. M. (eds.), IEEE, San Diego, CA, pp. 503–504.
- 151 Thomas, I. M. and Friedman, R. N. (1995) Study of macrophage activity in rat liver using intravenous superparamagnetic tracers, in *Biomagnetism: Fundamental Research and Clinical Applications*, Baumgartner, C. (ed.), Elsevier Science, pp. 809–813.
- 152 Weisskoff, R. M. and Kiihne, S. (1992) MRI susceptometry – image-based measurement of absolute susceptibility of MR contrast agents and human blood, *Magn. Reson. Med.* **24**, 375–383.
- 153 Yamada, N., Imakita, S., Sakuma, T., Nishimura, Y., Yamada, Y., Naito, H., Nishimura, T. and Takamiya, M. (1990) Evaluation of the susceptibility effect on the phase images of a simple gradient echo, *Radiology* **175**, 561–565.
- 154 Weis, J., Nilsson, S., Ericsson, A., Wikstrom, M., Sperber, G. O. and Hemmingsson, A. (1994) Measurement of magnetic-susceptibility and MR contrast agent concentration, *Magn. Reson. Imaging* **12**, 859–864.
- 155 Chu, S. C. K., Xu, Y., Balschi, J. A. and Springer, C. S. (1990) Bulk magnetic-susceptibility shifts in NMR-studies of compartmentalized samples – use of paramagnetic reagents, *Magn. Reson. Med.* **13**, 239–262.

- 156 Farrell, D. E. (1993) Assessment of iron in human tissue: the magnetic biopsy, in *Biomagnetism: An Interdisciplinary Approach*, Williamson, S. J. (ed.), Plenum Press, New York, pp. 483–499.
- 157 Brittenham, G. M., Sheth, S., Allen, C. J. and Farrell, D. E. (2001) Noninvasive methods for quantitative assessment of transfusional iron overload in sickle cell disease, *Semin. Hematol.* **38**, 37–56.
- 158 Paulson, D. N., Engelhardt, R., Fischer, R. and Heinrich, H. C. (1989) The Hamburg biosusceptometer for liver iron quantification, in *Advances in Biomagnetism*, Williamson, S. J., Hoke, M., Stroink, G. and Kotani, M. (eds.), Plenum Press, New York, pp. 497–500.
- 159 Ribeiro, E.P., Wikswo, J.P., Jr., Ribeiro, P.C., Monteiro, E.C., Bruno, A.C. and Szczupak, J. (1996) Tomografia de susceptibilidade magnetica com campo gradiente, in *III National Forum on Science and Technology in Health*, Campos Do Jordao, SP, Brazil.
- 160 Wang, Z. Y. J., Li, S. C. and Haselgrove, J. C. (1999) Magnetic resonance imaging measurement of volume magnetic susceptibility using a boundary condition, *J. Magn. Reson.* **140**, 477–481.
- 161 Plonsey, R. (1972) Capability and limitations of electrocardiography and magnetocardiography, *IEEE Trans. Biomed. Eng.* **BM19**, 239–244.
- 162 Rush, S. (1975) Independence of magnetic and electric body surface recordings, *IEEE Trans. Biomed. Eng.* **BME22**, 157–167.
- 163 Plonsey, R. and Barr, R. C. (1982) The four-electrode resistivity technique as applied to cardiac muscle, *IEEE Trans. Biomed. Eng.* **BME29**, 541–546.
- 164 Gulrajani, R. M. (1998) *Bioelectricity and Biomagnetism*, Wiley, New York.
- 165 Koch, H. and Haberkorn, W. (2001) Magnetic field mapping of cardiac electrophysiological function, *Philos. Trans. R. Soc. London A* **359**, 1287–1298.
- 166 Corbin, L. V., II and Scher, A. M. (1977) The canine heart as an electrocardiographic generator. Dependence on cardiac cell orientation, *Circ. Res.* **41**, 58–67.
- 167 Roberts, D. E., Hersh, L. T. and Scher, A. M. (1979) Influence of cardiac fiber orientation on wavefront voltage, conduction velocity, and tissue resistivity in the dog, *Circ. Res.* **44**, 701–712.
- 168 Roberts, D. E. and Scher, A. M. (1982) Effect of tissue anisotropy on extracellular potential fields in canine myocardium in situ, *Circ. Res.* **50**, 342–351.
- 169 Plonsey, R. and Barr, R. C. (1984) Current flow patterns in two-dimensional anisotropic bisyncytia with normal and extreme conductivities, *Biophys. J.* **45**, 557–571.
- 170 Barr, R. C. and Plonsey, R. (1984) Propagation of excitation in idealized anisotropic two-dimensional tissue, *Biophys. J.* **45**, 1191–1202.
- 171 Roth, B. J., Guo, W.-Q. and Wikswo, J. P., Jr. (1988) The effects of spiral anisotropy on the electric potential and the magnetic field at the apex of the heart, *Math. Biosci.* **88**, 191–221.
- 172 Staton, D. J. and Wikswo, J. P., Jr. (1995) High-resolution imaging of magnetic fields from injected and action currents in slices of anisotropic cardiac tissue, in *Biomagnetism: Fundamental Research and Clinical Applications: Proceedings of the 9th International Conference on Biomagnetism*, Baumgartner, C., Deecke, L., Stroink, G. and Williamson, S. J. (eds.), IOS Press, Amsterdam, pp. 684–687.
- 173 Staton, D. J. and Wikswo, J. P., Jr. (1995) Magnetic imaging of currents in two-dimensional cardiac tissue: experimental and theoretical studies of electrical activity in mammalian cardiac slices, in *Biomagnetism: Fundamental Research and Clinical Applications: Proceedings of the 9th International Conference on Biomagnetism*, Baumgartner, C., Deecke, L., Stroink, G. and Williamson, S. J. (eds.), IOS Press, Amsterdam, pp. 647–651.
- 174 Baudenbacher, F., Peters, N. T., Baudenbacher, P. and Wikswo, J. P. (2002) High resolution imaging of biomagnetic fields generated by action currents in cardiac tissue using a LTS-SQUID microscope, *Physica C* **368**, 24–31.
- 175 Fong, L. E., Holzer, J. R., McBride, K., Lima, E. A., Baudenbacher, F. and Radparvar, M. (2004) High-resolution imaging of cardiac biomagnetic fields using a low-transition-temperature supercon-

- ducting quantum interference device microscope, *Appl. Phys. Lett.* **84**, 3190–3192.
- 176 Katila, T. and Karp, P. (1983) Magneto-cardiography: morphology and multipole presentations, in *Biomagnetism: An Interdisciplinary Approach*, Williamson, S. J. (ed.), Plenum Press, New York, pp. 237–263.
- 177 Wikswo, J.P., Jr., Griffin, J.C., Leifer, M.C. and Harrison, D.C. (1978) Vector magnetocardiography: the effect of the heart lung boundary, *Clin. Res.* **26**, 486a.
- 178 Uutela, K., Hamalainen, M. and Salmelin, R. (1998) Global optimization in the localization of neuromagnetic sources, *IEEE Trans. Biomed. Eng.* **45**, 716–723.
- 179 Wilson, F. N., Johnston, F. D., Rosenbaum, F. F. and Barker, P. S. (1946) On Einthoven's triangle, the theory of unipolar electrocardiographic leads, and the interpretation of the precordial electrocardiogram, *Am. Heart J.* **32**, 277–310.
- 180 Wilson, F. N. and Bayley, R. H. (1950) The electric field of an eccentric dipole in a homogeneous spherical conducting medium, *Circulation* **1**, 84–92.
- 181 Gonnelli, R. S. and Agnello, M. (1987) Inverse problem solution in cardiomagnetism using a current multipole expansion of the primary sources, *Phys. Med. Biol.* **32**, 133–142.
- 182 Dossel, O. (2000) Inverse problem of electro- and magnetocardiography: review and recent progress, URL: http://www.ijbem.org/volume2/number2/doesel/paper_ijbem.htm.
- 183 VanVeen, B. D. and Buckley, K. M. (1988) Beamforming: a versatile approach to spatial filtering, *IEEE ASSP Magazine* **5**, 4–24.
- 184 Liu, T. C. and VanVeen, B. D. (1992) Multiple window based minimum variance spectrum estimation for multidimensional random-fields, *IEEE Trans. Signal Process.* **40**, 578–589.
- 185 Lacoss, R. T. (1968) Adaptive combining of wideband array data for optimal reception, *IEEE Trans. Geosci. Electron.* **GE 6**, 78–86.
- 186 van Drongelen, W., Yuchtman, M., VanVeen, B. D. and vanHuffelen, A. C. (1996) A spatial filtering technique to detect and localize multiple sources in the brain, *Brain Topogr.* **9**, 39–49.
- 187 Robinson, S.E. and Vrba, J. (1999) Functional neuroimaging by synthetic aperture magnetometry (SAM), in *Biomag98: 11th International Conference on Biomagnetism*, Sendai, Japan, Tohoku University Press, pp. 302–305.
- 188 VanVeen, B. D., van Drongelen, W., Yuchtman, M. and Suzuki, A. (1997) Localization of brain electrical activity via linearly constrained minimum variance spatial filtering, *IEEE Trans. Biomed. Eng.* **44**, 867–880.
- 189 Hillebrand, A. and Barnes, G. R. (2003) The use of anatomical constraints with MEG beamformers, *NeuroImage* **20**, 2302–2313.
- 190 Sekihara, K., Nagarajan, S. S., Poeppel, D. and Marantz, A. (2004) Performance of an MEG adaptive-beamformer source reconstruction technique in the presence of additive low-rank interference, *IEEE Trans. Biomed. Eng.* **51**, 90–99.
- 191 Schimpf, P. H., Liu, H. S., Ramon, C. and Hauelsen, J. (2005) Efficient electromagnetic source imaging with adaptive standardized LORETA/FOCUSS, *IEEE Trans. Biomed. Eng.* **52**, 901–908.
- 192 Hamalainen, M. S. and Ilmoniemi, R. J. (1994) Interpreting magnetic-fields of the brain – minimum norm estimates, *Med. Biol. Eng. Comp.* **32**, 35–42.
- 193 Haan, H., Streb, J., Bien, S. and Rosler, F. (2000) Individual cortical current density reconstructions of the semantic N400 effect: using a generalized minimum norm model with different constraints (L1 and L2 norm), *Hum. Brain Mapp.* **11**, 178–192.
- 194 Hauk, O. (2004) Keep it simple: a case for using classical minimum norm estimation in the analysis of EEG and MEG data, *NeuroImage* **21**, 1612–1621.
- 195 Hamalainen, M., Hari, R., Ilmoniemi, R. J., Knuutila, J. and Lounasmaa, O. V. (1993) Magnetoencephalography – theory, instrumentation, and applications to noninvasive studies of the working human brain, *Rev. Mod. Phys.* **65**, 413–497.
- 196 Uutela, K., Hamalainen, M. and Somersalo, E. (1999) Visualization of magnetoencephalographic data using mini-

- mum current estimates, *NeuroImage* **10**, 173–180.
- 197 Gorodnitsky, I. F., George, J. S. and Rao, B. D. (1995) Neuromagnetic source imaging with FOCUSS – a recursive weighted minimum norm algorithm, *Electroencephalogr. Clin. Neurophysiol.* **95**, 231–251.
- 198 Gorodnitsky, I. F. and Rao, B. D. (1997) Sparse signal reconstruction from limited data using FOCUSS: a re-weighted minimum norm algorithm, *IEEE Trans. Signal Process.* **45**, 600–616.
- 199 Schmidt, R. O. (1986) Multiple emitter location and signal parameter-estimation, *IEEE Trans. Antenn. Propag. AP-34*, 276–280.
- 200 Mosher, J. C., Lewis, P. S. and Leahy, R. M. (1992) Multiple dipole modeling and localization from spatio-temporal MEG data, *IEEE Trans. Biomed. Eng.* **39**, 541–557.
- 201 Mosher, J. C. and Leahy, R. M. (1998) Recursive MUSIC: a framework for EEG and MEG source localization, *IEEE Trans. Biomed. Eng.* **45**, 1342–1354.
- 202 Chen, W. G., Wong, K. M. and Reilly, J. P. (1991) Detection of the number of signals – a predicted eigen-threshold approach, *IEEE Trans. Signal Process.* **39**, 1088–1098.
- 203 Maier, J., Dagnelie, G., Spekreijse, H. and Vandijk, B. W. (1987) Principal components-analysis for source localization of veps in man, *Vision Res.* **27**, 165–177.
- 204 Achim, A., Richer, F. and Saint-Hilaire, J. M. (1988) Methods for separating temporally overlapping sources of neuroelectric data, *Brain Topogr.* **1**, 22–28.
- 205 Mocks, J. and Verleger, R. (1986) Principal component analysis of event-related potentials – a note on misallocation of variance, *Electroencephalogr. Clin. Neurophysiol.* **65**, 393–398.
- 206 Wood, C. C. and Mccarthy, G. (1984) Principal component analysis of event-related potentials – simulation studies demonstrate misallocation of variance across components, *Electroencephalogr. Clin. Neurophysiol.* **59**, 249–260.
- 207 Jutten, C. and Herault, J. (1991) Blind separation of sources: 1. An adaptive algorithm based on neuromimetic architecture, *Signal Process.* **24**, 1–10.
- 208 Comon, P. (1994) Independent component analysis, a new concept?, *Signal Process.* **36**, 287–314.
- 209 Tang, A. C., Pearlmutter, B. A., Malaszenko, N. A., Phung, D. B. and Reeb, B. C. (2002) Independent components of magnetoencephalography: localization, *Neural Comput.* **14**, 1827–1858.
- 210 Bell, A. J. and Sejnowski, T. J. (1995) An information maximization approach to blind separation and blind deconvolution, *Neural Comput.* **7**, 1129–1159.
- 211 Hyvarinen, A. (1999) Survey on independent component analysis, *Neural Comput. Surv.* **2**, 94–128.
- 212 Stone, J. V. (2002) Independent component analysis: an introduction, *Trends Cognitive Sci.* **6**, 59–64.
- 213 Zhukov, L., Weinstein, D. and Johnson, C. (2000) Independent component analysis for EEG source localization – an algorithm that reduces the complexity of localizing multiple neural sources, *IEEE Eng. Med. Biol. Magazine* **19**, 87–96.
- 214 Makeig, S., Jung, T. P., Bell, A. J., Ghahremani, D. and Sejnowski, T. J. (1997) Blind separation of auditory event-related brain responses into independent components, *Proc. Nat. Acad. Sci. USA* **94**, 10979–10984.
- 215 Vigario, R. N. (1997) Extraction of ocular artefacts from EEG using independent component analysis, *Electroencephalogr. Clin. Neurophysiol.* **103**, 395–404.
- 216 Vigario, R., Sarela, J., Jousmaki, V., Hamalainen, M. and Oja, E. (2000) Independent component approach to the analysis of EEG and MEG recordings, *IEEE Trans. Biomed. Eng.* **47**, 589–593.
- 217 Amari, S. and Cardoso, J. F. (1997) Blind source separation – semiparametric statistical approach, *IEEE Trans. Signal Process.* **45**, 2692–2700.
- 218 Ikeda, S. and Toyama, K. (2000) Independent component analysis for noisy data – MEG data analysis, *Neural Networks* **13**, 1063–1074.
- 219 Uusitalo, M. A. and Ilmoniemi, R. J. (1997) Signal-space projection method for separating MEG or EEG into compo-

- nents, *Med. Biol. Eng. Comp.* **35**, 135–140.
- 220 Ilmoniemi, R. (1997) Method and apparatus for separating the different components of evoked response and spontaneous activity brain signals as well as of signals measured from the heart, US Patent 5655534, PCT/F193/00504.
- 221 Miettinen, M. (1992) Magnetic measurements of visually evoked responses, M.Sc. Thesis, Helsinki University of Technology.
- 222 Nolte, G. and Curio, G. (1999) The effect of artifact rejection by signal-space projection on source localization accuracy in MEG measurements, *IEEE Trans. Biomed. Eng.* **46**, 400–408.
- 223 Nolte, G. and Hamalainen, M. S. (2001) Partial signal space projection for artefact removal in MEG measurements: a theoretical analysis, *Phys. Med. Biol.* **46**, 2873–2887.
- 224 Huotilainen, M., Ilmoniemi, R. J., Tiitinen, H., Lavikainen, J., Alho, K., Kajola, M., Simola, M. and Naatanen, R. (1993) Eye-blink removal for multichannel MEG measurements, in *Recent Advances in Biomagnetism: 9th International Conference on Biomagnetism*, Deecke, L., Baumgartner, C., Stroink, G. and Williamson, S. J. (eds.), Vienna, Austria, pp. 209–210.
- 225 Vrba, J., Robinson, S. E., McCubbin, J., Lowery, C. L., Eswaran, H., Wilson, J. D., Murphy, P. and Preissl, H. (2004) Fetal MEG redistribution by projection operators, *IEEE Trans. Biomed. Eng.* **51**, 1207–1218.
- 226 Hamalainen, M. S. (1995) Functional localization based on measurements with a whole-head magnetometer system, *Brain Topogr.* **7**, 283–289.
- 227 Tesche, C. D., Uusitalo, M. A., Ilmoniemi, R. J., Huotilainen, M., Kajola, M. and Salonen, O. (1995) Signal-space projections of MEG data characterize both distributed and well-localized neuronal sources, *Electroencephalogr. Clin. Neurophysiol.* **95**, 189–200.
- 228 Pascual-Marqui, R. D., Michel, C. M. and Lehmann, D. (1994) Low-resolution electromagnetic tomography – a new method for localizing electrical activity in the brain, *Int. J. Psychophysiol.* **18**, 49–65.
- 229 Lantz, G., Michel, C. M., Pascual-Marqui, R. D., Spinelli, L., Seeck, M., Seri, S., Landis, T. and Rosen, I. (1997) Extracranial localization of intracranial interictal epileptiform activity using LOR-ETA (low resolution electromagnetic tomography), *Electroencephalogr. Clin. Neurophysiol.* **102**, 414–422.
- 230 Anderer, P., Pascual-Marqui, R. D., Semlitsch, H. V. and Saletu, B. (1998) Differential effects of normal aging on sources of standard N1, target N1 and target P300 auditory event-related brain potentials revealed by low resolution electromagnetic tomography (LORETA), *Electroencephalogr. Clin. Neurophysiol./ Evoked Potent.* **108**, 160–174.
- 231 Pascual-Marqui, R. D. (2002) Standardized low-resolution brain electromagnetic tomography (sLORETA): technical details, *Methods Findings Exp. Clin. Pharmacol.* **24**, 5–12.
- 232 Wagner, M., Fuchs, M. and Kastner, J. (2004) Evaluation of sLORETA in the presence of noise and multiple sources, *Brain Topogr.* **16**, 277–280.
- 233 Clarke, C. J. S. and Janday, B. S. (1989) The solution of the biomagnetic inverse problem by maximum statistical entropy, *Inverse Problems* **5**, 483–500.
- 234 Amblard, U., Lapalme, E. and Lina, J. M. (2004) Biomagnetic source detection by maximum entropy and graphical models, *IEEE Trans. Biomed. Eng.* **51**, 427–442.
- 235 Greenblatt, R. E. (1993) Probabilistic reconstruction of multiple sources in the bioelectromagnetic inverse problem, *Inverse Problems* **9**, 271–284.
- 236 Gross, J., Ioannides, A. A., Dammers, J., Maess, B., Friederici, A. D. and Muller-Gartner, H. W. (1998) Magnetic field tomography analysis of continuous speech, *Brain Topogr.* **10**, 273–281.
- 237 Phillips, J. W., Leahy, R. M., Mosher, J. C. and Timsari, B. (1997) Imaging neural activity using MEG and EEG, *IEEE Eng. Med. Biol.* **16**, 34–42.
- 238 Baillet, S. and Garnero, L. (1997) A Bayesian approach to introducing anatomic-functional priors in the EEG/MEG

- inverse problem, *IEEE Trans. Biomed. Eng.* **44**, 374–385.
- 239 Mosher, J.C., Baillet, S. and Leahy, R.M. (2003) Equivalence of linear approaches in bioelectromagnetic inverse solutions, in *IEEE Workshop on Statistical Signal Processing*, St. Louis, MO, pp. 294–297.
- 240 Wikswo, J. P., Jr. (1995) SQUID magnetometers for biomagnetism and non-destructive testing: important questions and initial answers, *IEEE Trans. Appl. Supercond.* **5**, 74–120.
- 241 Wikswo, J. P., Jr. (2000) Applications of SQUID magnetometers to biomagnetism and nondestructive evaluation, in *Applications of Superconductivity*, Weinstock, H. (ed.), Kluwer Netherlands, pp. 139–228.
- 242 Kominis, I. K., Kornack, T. W., Allred, J. C. and Romalis, M. V. (2003) A sub-femtotesla multichannel atomic magnetometer, *Nature* **422**, 596–599.
- 243 Wikswo, J. P., Jr. (1990) Biomagnetic sources and their models, in *Advances in Biomagnetism*, Williamson, S. J. (ed.), Plenum Press, New York, pp. 1–18.
- 244 Wikswo, J. P., Jr., van Egeraat, J. M., Ma, Y. P., Sepulveda, N. G., Staton, D. J., Tan, S. and Wijesinghe, R. S. (1990) Instrumentation and techniques for high-resolution magnetic imaging, *Proc. SPIE* **1351**, 438–470.
- 245 Mall, F. P. (1911) On the muscular architecture of the ventricles of the human heart, *Am. J. Anat.* **11**, 211–266.

